

**Masters Thesis: Fast and Adaptable 3D Multi-Echo K-Space Sampling
for High-Resolution T2* and Susceptibility Mapping of the Human
Brain**

Jana Strizak

Biomedical and Biological Engineering, McGill University, Montreal

July 2024

A thesis submitted to McGill University in partial fulfillment of the requirements
of the degree of Master of Engineering

© Jana Strizak, 2024

Table of Contents

Abstract.....	11
Résumé.....	12
Acknowledgments.....	13
Contribution of Authors.....	13
1 Introduction.....	14
2 Background and review of the literature	16
2.1 Nuclear Magnetic Resonance and T_2^* contrast	16
2.2 T_2^* contrast in the human brain	18
2.3 Spatial encoding and k-space.....	20
2.4 Ultra-high field MRI.....	23
2.5 Fast Cartesian Trajectories.....	24
2.6 Fast Non-Cartesian Trajectories.....	26
2.6 Image Quality and Artifacts	36
2.7 T_2^* Mapping with Non-Cartesian Trajectories.....	39
2.8 Image Reconstruction of Non-Cartesian Trajectories	42
3 Methods.....	45
3.1 3D Multi-echo Seiffert Spiral (MESS) Trajectory Design.....	45
3.1.1 3D Seiffert Spiral	45
3.1.2 Radius Modulation	46
3.1.3 Optimal Sampling Distribution.....	49
3.1.4 Total Trajectory Arc-Length	51
3.1.5 Gradient Hardware Compliance	51
3.1.6 Trajectory Rotations along Fibonacci Lattice.....	54

3.1.7	Axis Rotations.....	55
3.1.8	Nyquist Check	58
3.2	Image reconstruction.....	60
3.3	Imaging Experiments	60
3.3.1	<i>Single-Echo Seiffert Spiral</i>	61
3.3.2	Spiral-Out vs Spiral-In-Out Trajectory Design.....	62
3.3.3	MESS Optimized for Quantitative T2* Mapping.....	62
3.3.4	Effects of Variable Sampling Density	63
4	Results.....	64
4.1	Single Echo Seiffert Spiral	64
4.2	Spiral-Out vs Spiral-In-Out Trajectory Design.....	70
4.3	MESS Optimized for T2* Mapping.....	74
4.4	Effects of non-uniform radial sampling density.....	77
5	Discussion	81
5.1	Comparison to Previous Work	84
5.2	Limitations and Future Work	85
6	Conclusion	88
7	References.....	89

List of Figures

Figure 1: T2* relaxation after a 90 degree radiofrequency excitation pulse. The red arrow represents the magnetization, which originally has a maximum amplitude as the spins are in phase. The amplitude of the transverse magnetization then decays over time as spins dephase. The characteristic T2* decay time is shown by the red star [14].	18
Figure 2: Gradient echo pulse sequence diagram (a) with (b) the acquisition of a single line of k-space or (c) the acquisition of an entire plane of k-space per TR, known as echo planar imaging [31].	22
Figure 3: T2* maps of the in vivo human brain acquired at 3T (below) and 7T (above) [19].	24
Figure 4: Multi-shot EPI sampling using interleaved schemes. In this example, a plane of k-space is acquired in 2 shots at different TRs, each acquiring every second line of k-space.	25
Figure 5: T2* maps of the human brain derived from the image's magnitude using a (A) 3D EPI and (B) 3D GRE adapted from [19].	25
Figure 6: The top row shows 3D NC trajectories that can be made 3D by stacking along z. K-space trajectories in the form of (a) stack-of-EPI, (b) the PROPELLER, (c) stack-of-spirals, (d) stack-of-radial [35], (e) Rosette, and (f) the stack-of-Sparking trajectories [36]. The bottom row shows truly 3D NC trajectories in the form of (g) 3D radial spokes (a.k.a., kooshball), (h) 3D Cones, (i) an inner shot of Shells, (j) an outer Shells, and (k) the 3D Sparkling trajectories. The 3D Sparkling trajectory shots emanate from the center of k-space and travel out [37].	26
Figure 7: Arrangement of 3D spokes along a k-space sphere based on the a) golden means and b) spiral phyllotaxis rotation methods [38]. The same total number of spokes (160) provides a different sampling distribution in k-space, with the phyllotaxis method being more uniformly distributed along the Fibonacci lattice.	28
Figure 8: Two designs of the Yarnball trajectory, both with the same 3D matrix size of R. The top row shows a trajectory with a greater number of shots (128) and a shorter single trajectory arch length. The bottom row contains less shots (32) but a longer trajectory [1].	30
Figure 9: The dual-echo wind-out-in Yarnball trajectory gradient waveforms (a) and k-space locations (b)[70].	30

Figure 10: 0.72 mm isotropic T1-weighted images of a phantom (A) and a healthy volunteer (B) acquired in only 98 seconds using a 3D Yarnball trajectory of 10ms on a 3T Siemens Prisma scanner with no parallel imaging [1]. 31

Figure 11: Single shot of the 3D Seiffert spiral trajectory for two different radial density compensation functions. Both Trajectories have a 3.0ms read-out duration, with a maximum gradient magnitude of 30mT/m and a slew-rate of 180 T/m/s [11]...... 32

Figure 12: Close up of the axial Nyquist and 8-fold undersampled Seiffert and 3D Cones images of the knee[11]...... 35

Figure 13: Cartesian and non-Cartesian imaging artifacts. A) Presence of a moderate wrap-around artifact due to undersampling of Cartesian k-space data[77]. B) Ghosting artifacts in EPI [84]. C) Streaking artifacts caused by radial sampling compared, d) Cartesian sampling which contains signal spreading in the phase encode direction [38]. E) 2 times undersampled aliasing artifact of spiral trajectory [79]...... 37

Figure 14: PSF of a) Yarnball (top row) and 3D cones (bottom row). The FOV is indicated by the red circles. The right column is the relative intensity of pixels outside the green area [1]. b) Simulated PSF for 4X undersampled Seiffert (left column), and 3D cones (right column) along the z and x directions [11]. 38

Figure 15: Simulated images comparing the Yarnball and cones trajectory to depict the appearance of artifacts [1]. 39

Figure 16: In vivo ultrashort echo time quantitative susceptibility mapping (UTE-QSM) with Cones trajectory of three representative healthy volunteers. (A) 39-year-old male, (B) 29-year-old female, and (C) 32-year-old female. The estimated susceptibility maps show a clear contrast between different tissues including the white matter, gray matter, vessels (yellow arrows), caudate (blue arrow), and putamen (green arrow)[66]...... 40

Figure 17: 2D Multi-Echo Rosette trajectory showing a) pedals collected during one TR contributing to different echoes, b) the trajectory rotated along the 2D plane to fill k-space, and c) the fully acquired k-space during multiple shots of the rosette trajectory for each echo time [54]. 40

Figure 18: Single subject T2* weighted images along with the T2* map from its respective multi-echo sequence during free-breathing and failed breath-hold conditions. White arrows show locations of motion artifacts more prevalent in Cartesian sampling than rosette [54]. 41

Figure 19: R2* (1/T2*) maps of the brain acquired using a stack-of-spirals depicting possibility for 1mm and 0.5mm acquisition at 3T [47]. 42

Figure 20: A single echo Seiffert spiral at 4 different α values of 0.1, 0.5, 1, and 2 corresponding to different radial sampling densities. The plot in a) shows the radial progression of the spiral through-out the readout time of 6ms for various α values. The trajectory's shape at the corresponding α values is shown for a b) spiral-out and c) spiral-in-out trajectory..... 46

Figure 21: Density of points heatmap along various planes for a single-echo spiral-out trajectory at various α parameters of 2, 1, 0.5, and 0.1. 47

Figure 22: Density of points heatmap along various planes for the first echo of a MESS spiral-in-out trajectory at various α parameters of 2, 1, 0.5, and 0.1. 48

Figure 23: A MESS trajectory showing the wind-in-out pattern, along with b) the echoes separated to demonstrate their sampling time along the T2* decay curve. 49

Figure 24: The effect of m parameter modulation on sample distributions in k-space for a single echo Seiffert spiral. The relationship between discrepancy and m are shown in a, while the trajectory with the highest and lowest discrepancies are shown in b. 50

Figure 25: The effect of m parameter modulation on sample distributions in k-space for a MESS. The relationship between the average discrepancy between all echoes and m are shown in a, while the trajectory with the highest and lowest discrepancies for each echo are shown in b to f..... 50

Figure 26: The k-space positions, gradient waveforms, and slew rates of the x, y, and z components of the a) single echo spiral-out trajectory, b) single echo spiral-in-out trajectory, and c) 5 echo MESS trajectory. The spiral-in-out and MESS trajectory include the pre-phasing gradient step that encodes the initial k-space position at the periphery of k-space. The rephrasing step is not included in the acquired MRI data. 53

Figure 27: Mechanical Gradients of a a) single echo spiral-out, b) single echo spiral-in-out, and c) multi echo Seiffert spiral. The red bars represent the forbidden frequencies ranges, and mechanical gradient peaks in this area should be avoided..... 53

Figure 28: Two shots of the a) single-echo and b) 5 echo MESS trajectory rotation points along the Fibonacci lattice. The rotation point for the single-echo case is the endpoint of the shot, while for the MESS case it is the endpoint of the samples corresponding to the first echo. Only rotation points for 100 shots are displayed for simplicity to demonstrate the Fibonacci lattice on the k-space sphere. 55

Figure 29: Sampling density plots representing number of points along each 2D column, normalized by the length of that column for a single echo trajectory with $\alpha = 1$. The top row is without axis rotations, and the bottom row is with random axis rotation, showing more uniformly spaced points. The spiral-in-out case also shows more densely sampled points at the periphery of the k-space sphere..... 56

Figure 30: Sampling density plots representing number of points along each 2D column, normalized by the radius at that column for a single echo trajectory for the MESS case. This displays the consistent density profile along all echo samplings profiles..... 57

Figure 31: Density of points along different k-space radial shells with thickness for the single echo spiral-out Seiffert spiral, displaying the uniform 3D distribution of points along each radial surface, and more dense sampling at smaller radii..... 58

Figure 32: PSF for R = 1 (top), R = 2 (middle), R = 6 (bottom) acceleration factors of the same single echo Seiffert spiral trajectory with 240 FOV, 0.8mm resolution, and an α of 1. 65

Figure 33: cross-section of PSF in x, y, and z directions for fully, half, and 6 times undersampled single echo Seiffert spiral with a nominal resolution of 0.8mm, along with the FWHM resolution displayed on the graphs. All image reconstruction was performed using the default NUFFT transform. 66

Figure 34: Digital phantom image for a single echo Sieffert spiral trajectory with R = 1 (left), R = 2 (middle), R = 6 (right) undersampling factors, and a constant 0.8mm resolution, 6ms readout, and an $\alpha = 1$ 67

Figure 35: Comparison of a 0.8mm, 240mm FOV MRI image acquired along a single echo Cartesian (left), and Seiffert spiral (right) trajectory. The Cartesian image is also used as a phantom to simulate the Seiffert spiral sampling and reconstruction of the same trajectory parameters under ideal conditions (middle)..... 68

Figure 36: Human brain T2* weighted single echo Seiffert spiral images acquired at 240 FOV, 0.8mm resolution, 6ms readout, $\alpha = 1$, fully (left) and half sampled (middle). Reconstruction was performed using 32 coils with root sum of squares averaged. The reconstruction was also performed using PICS on the half-sampled image (right)..... 69

Figure 37: PSF for a single echo 1.5mm resolution 6ms readout with and without T2* blurring for a) the spiral-out and b) spiral-in-out trajectory design case. Comparisons show more artifacts due to T2* blurring for the spiral-in-out trajectory case. 72

Figure 38: Digital phantom images of a single echo spiral-out (left) and spiral-in-out (right) trajectory designs with parameters described in Table 2, including a 240 FOV, 1.5mm resolution, 1ms readout, and an α of 0.5. Red arrows show locations of significant ringing artifacts. 73

Figure 39: Single echo Seiffert spiral acquisition of a phantom with scan parameters described in Table 2, including 240 FOV, 1.5mm resolution, 1ms readout, α of 0.5, $R = 1$, in a spiral-out shape (left) and spiral-in-out shape (right)..... 74

Figure 40: 6 times undersampled multi-echo digital phantom simulated sampling with the MESS trajectory as described in Table 3. 75

Figure 41: 5 echo 6 times undersampled MESS acquisition of a phantom at 0.8mm resolution, 240 FOV, 20ms readout (4ms per echo), and α of 2. All 5 echoes are shown along with 3 different views of the phantom. 76

Figure 42: 3 echo MESS acquisition at 204 FOV, 2mm resolution, 6ms readout (2ms per echo), α of 1, $R = 1$. All 3 echoes are shown along with 3 different views of the echoes. 77

Figure 43: A 3 echo MESS trajectory at various α radius modulation values showing its impact on the first echo's PSF. 79

Figure 44: Simulated digital phantom images at of the first echo of a 3 echo MESS trajectory with 6ms readout (2ms per echo), 2mm resolution, 240 FOV, R = 1, and three different α values of 0.5 (left), 1 (middle), and 2 (right)..... 80

Figure 45: First echo of a 3 echo MESS acquisition at 204 FOV, 2mm resolution, 6ms readout (2ms per echo), R = 1 at different α values of 0.5 (left), 1 (middle) and 2 (right). Differences between image quality due to a different α parameter are compared. 81

List of Tables

Table 1: Acquisition parameters for the single echo T2*-weighted human brain imaging protocols. 61

Table 2: Scan parameters for comparisons between spiral-out and spiral-in-out trajectory shapes. 62

Table 3: Scan parameters for MESS trajectory for quantitative imaging 62

Table 4: Image acquisition parameters for a 3-echo MESS protocols for three different α values: 0.1, 0.5, 1, and 2..... 63

Table 5: Table summarizing the PSF's FWHM of the spiral-out and spiral-in-out trajectory designs of nominal resolution 1.5mm and a short readout of 1ms. 70

Table 6: Table summarizing the PSF's FWHM of the spiral-out and spiral-in-out trajectory designs of target resolution 1.5mm and a longer readout time of 6ms, comparing with and without T2* blurring for grey matter with a T2* value of 33.2ms. 71

Table 7: FWHM with no T2* blurring for a 0.8mm resolution, 6 times undersampled, 20ms readout (5ms each echo), 5 echoes MESS trajectory as described the parameters in Table 3. 75

Table 8: Table summarizing the FWHM in x, y, and z for various α s of 0.5, 1, and 2 with a 3 echo MESS trajectory at 240 FOV, 2mm resolution, R = 1. 78

Table 9: Table summarizing scan parameters for various α values for a 3 echo MESS acquisition at 204 FOV, 2mm resolution, 6ms readout (2ms per echo), R = 1, and the Cartesian equivalent. 81

List of Abbreviations

MRI.....	Magnetic Resonance Imaging
T.....	Tesla
MESS	Multi-Echo Seiffert Spiral
GRE	Gradient Echo
QSM.....	Quantitative Susceptibility Mapping
FID	Free Induction Decay
TE.....	Echo Time
SNR.....	Signal-To-Noise Ratio
EPI	Echo-Planar Imaging
NC.....	Non-Cartesian
PROPELLER	Periodically Rotated Overlapping Parallel Lines with Enhanced Reconstruction
PSF	Point-Spread Function
DCF.....	Discrete Fourier Transform
FFT.....	Fast Fourier Transform
NUFFT.....	Non-Uniform Fast Fourier Transform
DCF.....	Density Compensation Function
FWHM	Full-Width-Half-Max
s.....	Seconds
min.....	Minutes
BART.....	Berkeley Advanced Reconstruction Toolbox
PDHG.....	Partial Dual Hybrid Gradient

Abstract

Brain iron deposition is associated with neurodegenerative disorders such as Alzheimer's and Parkinson's disease and can be imaged in vivo non-invasively using magnetic resonance imaging (MRI). T2* maps and magnetic susceptibility maps can be calculated from multi-echo T2*-weighted gradient echo images. These quantitative biomarkers have been used to investigate the role of iron accumulation in the brain in healthy aging and neurodegenerative disorders. However, limitations such as long exam durations and sensitivity to motion have hindered their use in clinical research. To overcome this, I designed a sequence that incorporates a novel 3D non-Cartesian trajectory in the shape of a multi-echo Seiffert spiral (MESS). This acquisition allows for strategic image under-sampling for shorter scan times and is compatible with retrospective motion correction techniques. I implemented the sequence on an ultra-high field strength (7 Tesla) scanner, which provides higher signal for high-resolution imaging (<1mm). The image quality and imaging efficiency of this novel technique is compared against the current gold standard acquisition, a Cartesian line-by-line trajectory, in simulations, a phantom (test object), and human subjects. This project will enable the use of fast T2* and susceptibility mapping at 7T as a quantitative biomarkers of tissue iron content in normal ageing and neurodegenerative disorders.

Résumé

L'accumulation de fer dans le cerveau est associée à des troubles neurodégénératifs tels que les maladies d'Alzheimer et de Parkinson, et peut être visualisée in vivo de manière non invasive à l'aide de l'imagerie par résonance magnétique. Les cartes T2* et les cartes de susceptibilité magnétique peuvent être calculées à partir d'images d'écho de gradient multi-échos pondérées T2*. Ces biomarqueurs quantitatifs ont été utilisés pour étudier le rôle de l'accumulation de fer dans le cerveau dans le vieillissement en santé et les troubles neurodégénératifs. Cependant, des limitations, telles que la longue durée des examens et la sensibilité au mouvement, ont entravé leur utilisation en recherche clinique. Pour surmonter ce problème, j'ai conçu une séquence qui intègre une nouvelle trajectoire non-cartésienne 3D sous la forme d'une spirale Seiffert multi-écho (MESS). Cette acquisition permet un sous-échantillonnage stratégique des images pour des temps d'acquisition plus courts et est compatible avec les techniques rétrospectives de correction de mouvement. J'ai implémenté la séquence sur un scanner à ultra-haute intensité de champ (7 Tesla) qui fournit un signal plus élevé pour une imagerie haute résolution (<1 mm). La qualité de l'image et l'efficacité de cette nouvelle technique sont comparées à l'acquisition de référence actuelle, une trajectoire cartésienne ligne par ligne, chez un fantôme et des sujets humains. Ce projet permettra d'utiliser la cartographie rapide de T2* et de la susceptibilité magnétique à 7T comme biomarqueurs quantitatifs de la teneur en fer du cerveau chez les personnes vieillissant en santé et celles atteintes d'un trouble neurodégénératif.

Acknowledgments

I acknowledge the assistance of Robert Stobbe, a research scientist at the University of Alberta, for aiding in the design of the multi-echo trajectory through the supplementation of his Yarnball design's Matlab and Siemen's Idea pipeline [1].

I also acknowledge the assistance of Sajjad Feizollah, a PhD candidate at McGill University, and Marcus Coach, a Siemens Collaboration Scientist at the Montreal Neurological Institute, for assistance with the MRI data acquisition and reconstruction of the novel acquisition scheme introduced in this thesis. Sajjad Feizollah's assistance, along with Robert Stobbe, was imperative in the setup of the image reconstruction pipeline of non-Cartesian data.

Finally, I acknowledge the assistance and guidance provided by my supervisor Christine Tardif, an Assistant Professor in the Department of Neurology and Neurosurgery and Department of Biomedical Engineering at McGill University, throughout the entirety of this master's project.

Contribution of Authors

I am the author for each chapter of the thesis and have performed all of the work described in chapters 8 and 9, with the assistance of Sajjad Feizollah, a PhD candidate in Prof Tardif's lab, for the MRI data collection. This includes:

- the trajectory design and creation,
- the theoretical image simulations, point spread functions, and other trajectory analysis,
- the design of studies and experimental protocols,
- the collect of experimental MRI data, with the assistance of Sajjad Feizollah,
- the analysis of all experimental MRI data,
- the writing of the thesis.

The research conducted towards this thesis was presented at the 2023 Quebec Bio-Imaging Network Scientific Day and the 2023 McGill Biological and Biomedical Engineering Symposium.

1 Introduction

Neurodegenerative disorders such as Alzheimer's and Parkinson's disease are associated with iron deposition in the brain due to increased oxidative stress and aggregation of proteins such as amyloid- β and α -synuclein [2-4]. The iron causes local variations in magnetic susceptibility, allowing it to be imaged using T2*-weighted gradient echo (GRE) magnetic resonance imaging (MRI) [5-7]. Quantitative imaging biomarkers, such as T2* relaxation time maps and quantitative susceptibility maps (QSM), can be calculated from multi-echo GRE data to investigate cortical and subcortical iron deposition in neurodegenerative disorders [6-10]. Imaging at the ultra-high field strength of 7 Tesla (T) allows for increased image resolution as well as enhanced T2*-weighted brain tissue contrast due to the shortened T2* times. However, the adoption of these promising quantitative MRI biomarkers into clinical research is limited by long scan times and sensitivity to subject movement, which are exacerbated at high-resolution and leads to poor image quality and artifacts.

Acquiring multi-echo T2*-weighted images at 7T using a flexible and adaptable non-Cartesian 3D trajectory will allow for high-resolution T2* maps and QSM of the brain in shorter scan times and with minimal artifacts. The aim of my masters' thesis project is to design a multi-echo GRE trajectory that efficiently samples k-space to reduce scan time, strategically undersamples k-space in all three directions, and provides compatibility with motion correction.

I have implemented a 3D non-Cartesian k-space trajectory that efficiently traverses k-space through a spiral pattern similar to winding a yarn-ball. The trajectory is created by expanding the Seiffert spiral's geometric winding on a spherical surface to 3D by modulation the radius, as well as partitioning the continuous spiral into multiple contiguous segments corresponding to multiple echoes [11]. This trajectory allows for the modulation of k-space sampling density as a function of the radius and distributes the undersampling in all 3 dimensions, leading to scan time reductions compared to Cartesian sampling. It is also better conditioned for compressed sensing and parallel image reconstruction of undersampled data due to the dispersed aliasing artifacts. Finally, the repetitive sampling of the center of k-space reduces motion artifacts

through signal averaging and enables the application of retrospective motion-correction strategies.

The single- and multi-echo Seiffert spiral (MESS) trajectory designs are compared to the conventional line-by-line Cartesian trajectory. Point-spread function analysis as well as digital phantom image sampling and reconstruction are performed to evaluate the impact of the trajectory on image resolution and sampling artifacts, respectively. Phantom scans were performed on the 7T scanner at the Montreal Neurological Institute to assess image quality when impacted by T2* blurring, magnetic field inhomogeneities, and trajectory deviations due to imperfections in the spatial encoding gradient waveforms. A single echo T2*-weighted GRE human brain acquisition is performed using the 3D Seiffert spiral and conventional Cartesian trajectory to evaluate *in vivo* image quality as well.

Quantitative T₂* and susceptibility mapping are promising biomarkers for the early diagnosis of neurodegenerative disorders and monitoring of treatment efficacy. This fast 3D MESS imaging trajectory at 7T is a promising approach for the generation of high-resolution T2* maps and QSM images of the brain in short scan times appropriate for clinical applications.

2 Background and review of the literature

2.1 Nuclear Magnetic Resonance and T_2^* contrast

MRI operates based on the nuclear magnetic resonance phenomenon inherent to particles possessing the quantum property of spin angular momentum (I) [12]. This is present in atomic nuclei with an odd number of protons and/or neutrons, and its value is quantized into an integer or half-integer value. MRI predominantly images hydrogen nuclei in water with a spin of $\frac{1}{2}$ due to their abundance in biological soft tissues. However, other nuclei with spin such as carbon, oxygen, sodium, and fluorine, can also be imaged. The magnetic moment m of a nucleus describes how it interacts with an external magnetic field. As shown in (Equation 1) below, the magnetic moment is linearly related to the spin by the gyromagnetic ratio (γ) unique to each atomic species:

$$m = \gamma I$$

(Equation 1)

In the presence of an external magnetic field B_0 , the various m and I states are differentiated into $2I + 1$ different energy states. A H^1 nucleus can therefore be in 2 different states, called spin-up and spin-down. When the nucleus is submitted to an external magnetic field (B_0), typically ranging from 0.5 to 7 Tesla (T) in the clinic, and applied along the z-direction, the spins align parallel or anti-parallel with the field corresponding to the low and high-energy states respectively. The spins start precessing at the Larmor frequency about the z-axis proportional to the magnitude of B_0 , related by the gyromagnetic ratio (γ).

$$\omega_L = \gamma B_0$$

(Equation 2)

The probability of being in the spin-up or spin-down state is a function of the temperature (T) and is described by the Boltzmann distribution. The vector sum of the magnetic moments of the entire system, referred to as the macroscopic magnetization M , is of interest in MRI. The maximum value the net magnetization (M_0) can be at a specific temperature is related to the density of spins in the material (ρ) and is proportional to B_0 , meaning a stronger field will produce a larger MR signal.

$$M_0 = \frac{\gamma^2 h^2 \rho B_0}{4kT}$$

(Equation 3)

where h is Planck's constant, k is the Boltzmann constant, and T is the temperature. An electromagnetic wave in the form of a radio-frequency pulse is used to disturb the equilibrium state of the net magnetization by exciting the magnetic moments of the particles to higher energy states. This pulse is applied at the Larmor frequency to ensure energy absorption by the target nuclei and perpendicular to the B_0 magnetic field. The result is that the magnetization is tipped away from the z-axis into the transverse plane. The net magnetization will relax back to its equilibrium state once the radio-frequency pulse is turned off, where the transverse component M_{xy} decays exponentially with time constant T_2 and the longitudinal component M_z recovers exponentially with time constant T_1 . The decay of the electromagnetic signal in the transverse plane immediately after the excitation pulse is called the free induction decay (FID) (Figure 1).

T_2 decay is the time it takes for the net transverse magnetization to dissipate due to interactions between neighboring spins leading to a loss of phase coherence. This is influenced by tissue composition, temperature, and molecular motion. However, other mechanisms exist that contribute to the signal decay in the transverse plane. Local magnetic field inhomogeneities or susceptibility differences in tissues can cause small magnetic field variations within a voxel (ΔB), causing slightly different precession frequencies and phase shifts between individual spins. This dephasing causes a loss of coherence and thus enhanced M_{xy} signal decay at a characteristic time of T_2^* described in (Equation 5). These irregularities may arise from local iron deposition within the brain, variations in magnetic susceptibility at air-tissue interfaces, or from imperfections in the main magnetic field B_0 itself. The T_2^* relaxation time is related to T_2 and local variations in the magnetic field (ΔB) as:

$$\frac{1}{T_2^*} = \frac{1}{T_2} + \frac{1}{\gamma \Delta B}$$

(Equation 4)

The T2*-weighted signal is the exponential decay of the transverse magnetization after excitation ($M_{xy}(t_0)$) over a duration of time (t) from the start of the excitation (t_0) described by:

$$M_{xy}(t) = M_{xy}(t_0)e^{-\frac{t-t_0}{T_2^*}}$$

(Equation 5)

To measure voxel-wise T2* decay times, multiple T2*-weighted MRI measurements at different time points after excitation need to be acquired and subsequently fit to the signal equation above. The multi-echo data is fitted to a mono-exponential decay at each image voxel location to generate a T2* map [13]. T2* mapping serves as a valuable quantitative biomarker in MRI, offering insights into the composition of each voxel within an imaged volume.

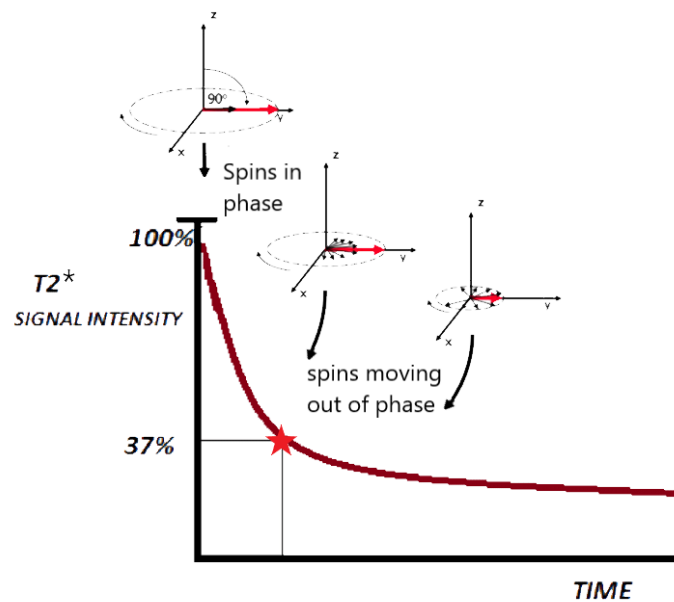


Figure 1: T2* relaxation after a 90 degree radiofrequency excitation pulse. The red arrow represents the magnetization, which originally has a maximum amplitude as the spins are in phase. The amplitude of the transverse magnetization then decays over time as spins dephase. The characteristic T2* decay time is shown by the red star [14].

2.2 T2* contrast in the human brain

In brain tissue, shorter T2* decay times are associated with the presence of iron deposits and variations in myelin content [15]. Since T2* is sensitive to local sources of magnetic susceptibility, it has been used to map ferromagnetic iron-rich deep brain structures [2-4, 6],

heavily myelinated intra-cortical laminae [4], and the venous vasculature tree [8, 16-18]. T2* decay is also sensitive to the level of blood oxygenation since deoxyhemoglobin is paramagnetic [7]. Quantitative and functional imaging of cerebral venous oxygen level has been used to assess cognitive impairment and the progression of neurodegenerative diseases [16-18]. These applications demonstrate T2* mapping as a powerful tool for characterizing brain tissue composition and potentially aiding in monitoring the progression of neurodegeneration and the impact of therapeutic interventions.

In healthy brains, T2* values typically vary across different brain regions depending on the local constituents of the region. Gray matter usually exhibits shorter T2* values compared to white matter due to variations in myelin content, iron concentration, and neuronal density. Iron content is normally largest in the putamen and least in the medulla in adult brains [19]. Normal aging is commonly associated with an increase in brain iron content in regions such as the basal ganglia (caudate nucleus, putamen, and globus pallidus)[20]. This is due to multiple factors, including altered iron homeostasis, increased oxidative stress, and changes in cellular metabolism. This phenomenon is often observed in neuroimaging studies and is believed to play a role in age-related cognitive decline and motor functions with implications in susceptibility to neurodegenerative conditions [21]. Some variations between structures exist, such as deep gray matter structures showing negative association between T2* values and aging due to iron accumulation, while white matter shows a positive association due to demyelination [22].

Neurodegenerative disorders such as Alzheimer's, Huntington, and Parkinson's disease are also associated with iron deposition in the brain due to increased oxidative stress and aggregation of proteins such as amyloid- β and α -synuclein [2-4]. Iron accumulation can be quantified with T2* mapping. This association has been validated with histology in postmortem imaging [15, 23, 24]. Iron deposits have been imaged using T2*-weighted GRE and has been linked with the progression of neurodegenerative disorders in vivo [5-7]. In-vivo imaging of Parkinson's disease showed a decrease in T2* values in the substantia nigra and other basal ganglia structures indicating increased iron deposits compared to healthy controls [25]. In-vivo imaging of Alzheimer's patients showed T2* relaxation rates in the bilateral hippocampus, caudate

nucleus, putamen and right globus pallidus to be significantly higher than the control group [26]. The putamen T2* values are most significantly correlated with the Alzheimer’s disease mini-mental state examinations [26]. These deviations in iron distribution and intensity on T2* maps serve as potential biomarkers, enabling the differentiation and characterization of neurodegenerative disorders from the natural aging-related changes, thereby aiding in early diagnosis, and potentially offering insights into disease progression and treatment strategies.

2.3 Spatial encoding and k-space

Traveling through K-Space

After excitation, the resulting precessing transverse magnetization M_{xy} will induce an electromotive force on the receiver coil. The signal recorded will be the aggregate signal from all spins in the excited volume:

$$s(t) = \int_r M(r)e^{-i\gamma Bt} dr$$

(Equation 6)

Where r is the position along the volume. To create an image, the signal from different spatial positions must be resolved. Spatial localization of the MRI signal is encoded by superimposing a spatial magnetic field gradient G on the stronger and uniform main magnetic field. A linearly varying magnetic field gradient is applied along the x, y, and/or z directions, which changes the local magnetic field at each point in space, leading to a precession frequency different from its neighbors.

$$B(r) = B_o + rG(r)$$

(Equation 7)

After the gradient magnetic field is turned off, and the individual spins return to the precession frequency dictated by the main magnetic field, there exists a phase difference that varies as a function of position. The relationship between the magnetic field gradient and k-space position is determined by the temporal integral of the gradient magnetic field:

$$k(t) = \frac{\gamma}{2\pi} \int_0^t G(\tau) d\tau$$

(Equation 8)

In conventional 3D Cartesian imaging, the y- and z-axis is *phase encoded* before the readout starts with a gradient in the y and z direction corresponding to desired y and z coordinate in k-space, described by (Equation 8). As the data acquisition commences, the gradient in the x direction turns on at the same time, allowing for movement in the x direction in k-space.

Encoding in the x direction, called the *frequency encoding* direction, is done at the same time as the readout (Figure 2,b). Together, various line-by-line frequency and phase encoding steps acquire the entire 3D Cartesian grid.

The signal $s(t)$ generated in the presence of the gradient field is proportional to the Fourier transform of the spatial magnetization distribution $M(r)$.

$$s(t) = \int_r M(r) e^{-i\gamma(B+Gr)t} dr = e^{-i\gamma Bt} \int_r M(r) e^{-i\gamma Gtr} dr = e^{-i\gamma Bt} \int_r M(r) e^{-2\pi ikr} dr$$

where $k = \frac{\gamma}{2\pi} Gt$ for a linearly varying gradient field.

(Equation 9)

Since k-space is the spatial frequency domain of the image, the extent of k-space is the reciprocal of the image resolution, and the separation between k-space points is the reciprocal of the image field-of-view (FOV). The sequence of k-space points acquired along a path in k-space after a single excitation is called the k-space trajectory.

The center of k-space contains the low spatial frequency information that contributes the majority of the signal in the image. The time at which the center of k-space is acquired, called the echo time (TE), determines the T2*-weighted image contrast. It also establishes the signal-to-noise ratio (SNR), which is essential for image quality.

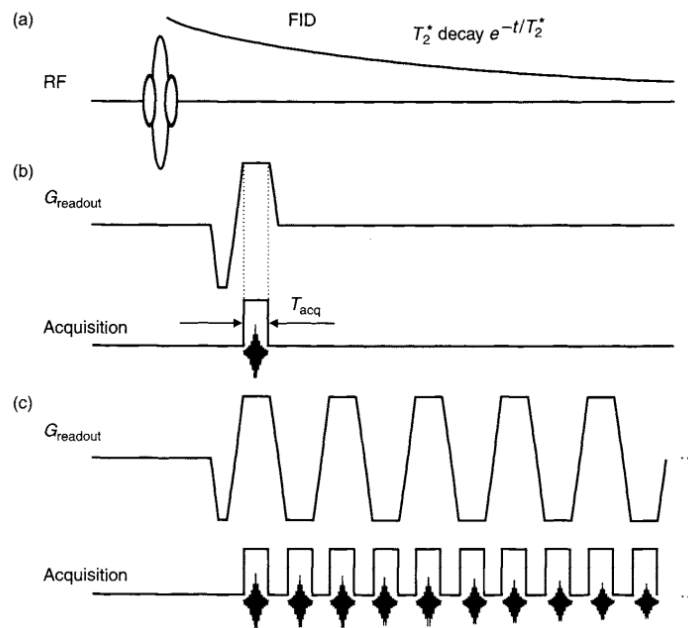


Figure 2: Gradient echo pulse sequence diagram (a) with (b) the acquisition of a single line of k-space or (c) the acquisition of an entire plane of k-space per TR, known as echo planar imaging [31].

Cartesian Gradient Echo (GRE) Acquisition

The basic Cartesian T_2^* -weighted gradient echo (GRE) sequence acquires a single phase encode line of k-space per TR (Figure 2,c) [31]. This is completed in a readout time of $\sim 2\text{ms}$, which is very short compared to the T_2^* decay time of brain tissue of approximately 60ms and 30ms at 3T and 7T, respectively. It is also very short with respect to the sequence TR. While inefficient, this short readout duration benefit from fewer artifacts. Longer readouts allow errors to accumulate due to the dephasing of spins caused by spatiotemporal B_0 variations, concurrent gradient fields, and eddy currents. T_2^* decay during acquisition is also an inherent problem with longer readout durations as later data points will have a lower signal, resulting in a T_2^* filter of k-space and blurring of the image.

The total number of TRs required to acquire k-space is called the number of shots (N_{shot}). A high number of shots is associated with longer scan times, which increase susceptibility to motion artifacts, reduce patient comfort, and are thus impractical for clinical use.

Multi-echo GRE Acquisition

Multi-echo data is collected using a gradient echo sequence by acquiring one line of k-space multiple times ($\sim 4-7$ echo times) within a single TR. An image is reconstructed for each echo time and a $T2^*$ value is fit at each voxel to create a $T2^*$ map. The multi-echo readout trajectory is either monopolar, where the data is readout in the same direction for each echo requiring an inter-echo delay to return to the starting k-space location, or bipolar, where the readout gradient polarity is reversed for each subsequent echo. This method is the gold standard for $T2^*$ mapping.

The acquisition of multi-echo data for $T2^*$ mapping requires longer TRs, to accommodate the longest TE, and thus long acquisition times, contributing to sensitivity to motion [21]. The longest component of the image acquisition is the time required to play out the gradient waveforms, which is limited by the maximum gradient amplitude and slew rate of the system. To shorten scan time, we can improve the efficiency of k-space sampling, acquire more of k-space per shot, and under-sample k-space data. In contrast to Cartesian imaging, non-Cartesian imaging samples k-space along 2D or 3D arbitrary trajectories that can be designed to shorten scan time using the strategies above, and increase robustness to subject motion.

2.4 Ultra-high field MRI

The main magnetic field B_0 of the MRI scanner is an important factor determining image quality and contrast. Most neuroimaging is performed at 1.5T or 3T field strengths, however 7T scanners are becoming more common in research and clinical settings due to their enhanced sensitivity and image resolution.

Higher magnetic field strengths are associated with higher signal strength emitted from the imaged tissue, leading to improved SNR. Achieving sufficient SNR is a challenge for high-resolution imaging due to the smaller voxel volumes, thus imaging at higher field strengths could be used to mitigate this. [27]. In fact, the same SNR can be achieved at 7T with a 2.4 times smaller voxel volume than at 3T [28].

Another advantage of a higher magnetic field strength is the shorter $T2^*$ decay, which enhances tissue contrast at shorter echo times. Tissue susceptibility causing local $T2^*$ signal dephasing

due to iron deposits or myelin is proportional to the external magnetic field. For this reason, T_2^* decay is faster at 7T with gray matter going from a 66ms to a 33.2ms relaxation time, while white matter decreases from 53.2ms to 26.8ms, the Caudate from 41.3ms to 19.9ms, and the Putamen from 31.5ms to 16.1ms [29]. The faster decay times enhance grey and white matter tissue contrasts at shorter echo times, leading to better contrast-to-noise ratios, and better delineation of fine brain structures at 7T using T_2^* -weighted GRE (Figure 3). This also enhances the detection [30, 31], and demyelination[32].

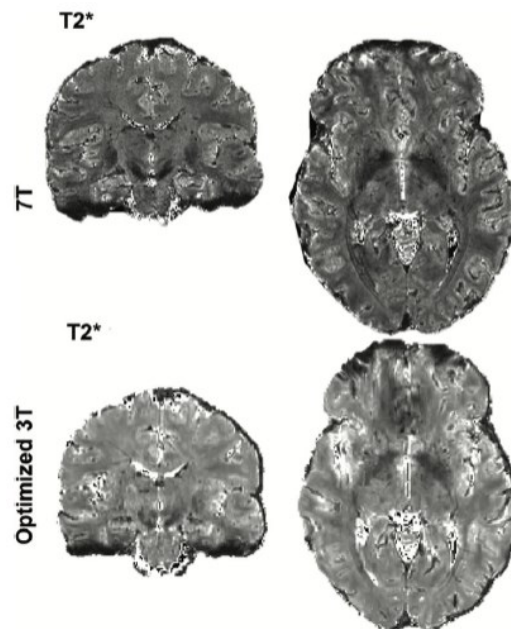


Figure 3: T_2^* maps of the in vivo human brain acquired at 3T (below) and 7T (above) [19].

2.5 Fast Cartesian Trajectories

Fast imaging techniques have been developed for diverse MRI applications such as pediatric, clinical, and dynamic imaging. The goal is most often to improve patient comfort and motion robustness. The need for fast acquisitions has led to the creation of fast Cartesian trajectories in the form of echo-planar imaging (EPI), and non-Cartesian trajectories.

Echo Planar Imaging: EPI involves the acquisition of a complete 2D k-space plane using a Cartesian grid. This trajectory makes use of bipolar readout gradients and acquires multiple k-space lines per echo in a back-and-forth zig-zag fashion. It is typical for a single RF excitation EPI

to acquire 60-100 lines of k-space, depending on the T_2^* decay time of the tissue. Alternatively, higher resolution images can be acquired using a segmented EPI trajectory [33].

The EPI trajectory can be subdivided into multiple segments or shots if the readout duration is too long with respect to the T_2^* decay time of the tissue. This can be done by acquiring k-space phase encode lines in a sequential or interleaved fashion, as shown in Figure 4. The interleaved method is most common to avoid large differences in signal delay between neighboring k-space points along the phase encode direction, which could lead to enhanced image artifacts.

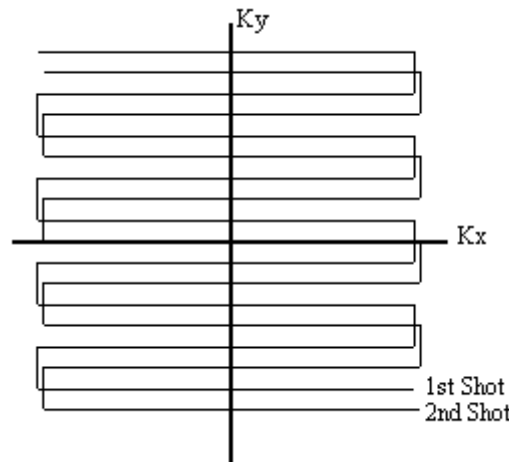


Figure 4: Multi-shot EPI sampling using interleaved schemes. In this example, a plane of k-space is acquired in 2 shots at different TRs, each acquiring every second line of k-space.

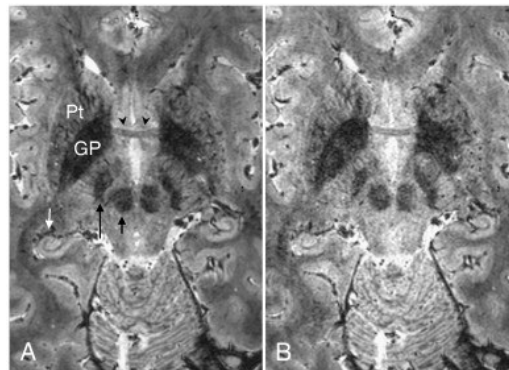


Figure 5: T_2^* maps of the human brain derived from the image's magnitude using a (A) 3D EPI and (B) 3D GRE adapted from [19].

3D EPI: To acquire a 3D volume, we can either create a stack of 2D EPI trajectories along z , or by creating a 3D EPI trajectory. The latter typically requires segmenting the trajectory into multiple interleaved shots. This 3D trajectory has been used to acquire high-resolution (0.5mm isotropic)

T2*-weighted images of the brain at 7T within 6 minutes, corresponding to a 4.5X acceleration compared to 3D GRE. The 3D EPI image also had twice the SNR of the GRE image. The T2* induced image blurring was not significant if the readout duration was shorter than the T2* decay time of the imaged tissue. The 3D EPI images in Figure 5 show improved tissue border visualization between white matter and the putamen, hippocampus, and substantia nigra [34].

2.6 Fast Non-Cartesian Trajectories

Non-Cartesian (NC) sampling trajectories travel through k-space and sample points which don't align with a uniformly sampled Cartesian grid. The sampling patterns can be designed to improve imaging efficiency, robustness to motion, and SNR.

3D NC trajectories can consist of 2D trajectories stacked in the third dimension, making them Cartesian in the stacked direction, or a true 3D trajectory which travels in all three k-space directions at each shot. A few of the most used trajectories are represented in Figure 6 and described briefly below.

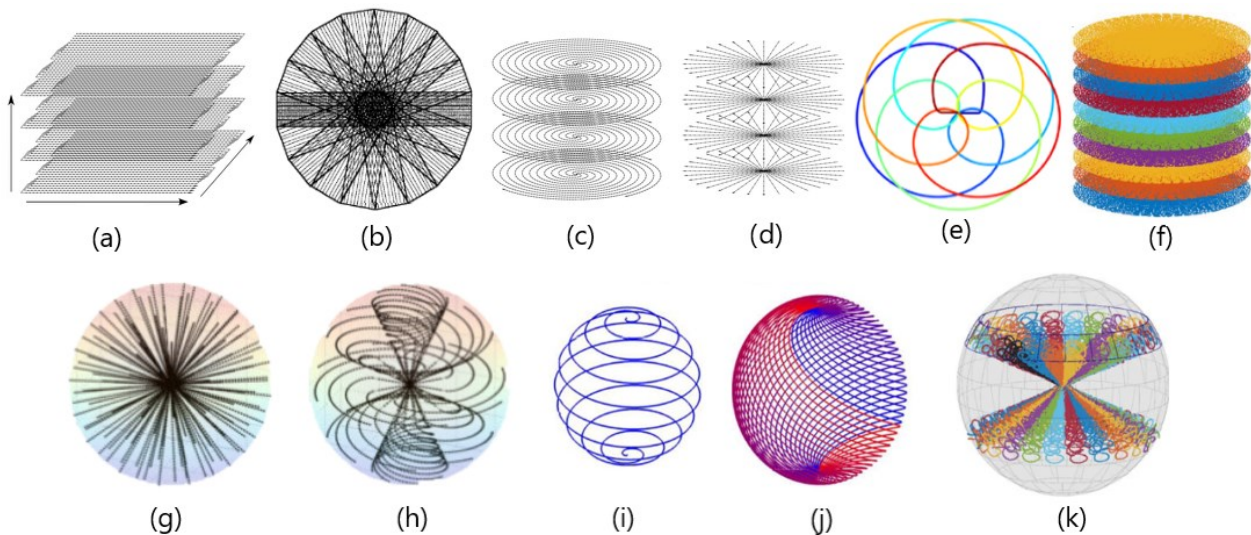


Figure 6: The top row shows 3D NC trajectories that can be made 3D by stacking along z . K-space trajectories in the form of (a) stack-of-EPI, (b) the PROPELLER, (c) stack-of-spirals, (d) stack-of-radial [35], (e) Rosette, and (f) the stack-of-Sparking trajectories [36]. The bottom row shows truly 3D NC trajectories in the form of (g) 3D radial spokes (a.k.a., kooshball), (h) 3D Cones, (i) an inner shot of Shells, (j) an outer Shells, and (k) the 3D Sparkling trajectories. The 3D Sparkling trajectory shots emanate from the center of k-space and travel out [37].

Radial Trajectories: Radial trajectories take the shape of radial spokes emanating from the center of k-space, or going through the centre of k-space, at various angles. The 3D radial trajectory could consist of a stack-of-stars (Figure 6d) or a 3D kooshball of spokes (Figure 6g) arranged along a 3D spherical surface. Radial trajectories regularly sample the centre of k-space, making it more robust to motion [38]. The sampling density is also typically higher in the centre of k-space, which contains most of the image energy, resulting in an increase in SNR.

For a fully sampled 3D radial acquisition, the number of spokes required to meet the Nyquist criteria is:

$$N_{radial}(r_k) = 4\pi r_k \Delta k_{nyquist}$$

(Equation 10)

Where $\Delta k_{nyquist} = \frac{1}{FOV}$ is the nyquist criteria in k-space related to the image domain FOV, and $r_k = \frac{1}{res}$ is the maximum k-space radius achieved based on the image domain resolution.

The angles of rotation and acquisition order of the spokes can impact the quality of the image. Phyllotaxis golden-angle radial sampling, shown in Figure 7b, is a rotation method where a Fibonacci lattice is traversed through a series of golden angle rotations leading to evenly spaced 3D k-space spokes [39]. The acquisition order of radial spokes can be distributed along the Fibonacci lattice to maximize the k-space volume acquired, ideal for dynamic MRI where fast coverage distributed along k-space can create low-resolution images at various time points [40, 41].

Golden means is an alternative radial rotation method that creates rotations along the azimuthal and polar angles based on Fibonacci sequence eigenvalues, as shown in Figure 7a. This method does not guarantee even spacing between spokes, thus the total number of shots required is not predetermined. However, improvements to motion artifacts and temporal stability are observed due to the acquisition order of the spokes [42].

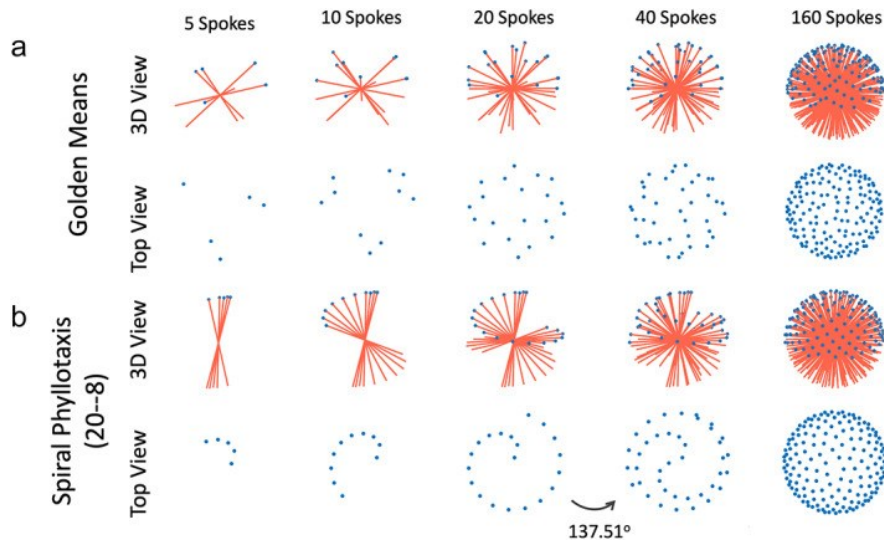


Figure 7: Arrangement of 3D spokes along a k -space sphere based on the a) golden means and b) spiral phyllotaxis rotation methods [38]. The same total number of spokes (160) provides a different sampling distribution in k -space, with the phyllotaxis method being more uniformly distributed along the Fibonacci lattice.

Propeller Trajectory: A NC trajectory formed from Cartesian rectangles rotated along a radial pattern on a 2D plane is the Periodically Rotated Overlapping Parallel Lines with Enhanced Reconstruction (PROPELLER) trajectory (Figure 6b) [36, 43-45]. This hybrid trajectory combines the properties of radial trajectories, with more k -space coverage per shot. It benefits from robustness to motion artifacts, along with the potential for retrospective motion correction.

Spiral Trajectories: Spiral trajectories involve the continuous, spiral-like sampling of k -space, with the trajectory path extending outward from the center of k -space, or vice versa, in a circular motion with increasing/decreasing radius (Figure 6c) [46-51]. The spiral can be density modulated to acquire data at various sampling densities as a function of radius [52], usually compressed towards the center to increase SNR. 3D imaging can be performed using a stack-of-spirals trajectory (Figure 6c) or by rotating the 2D spiral about the z -axis, resulting in a radial pattern at each z -plane [49].

Rosette Trajectory: The Rosette trajectory involves a continuous, radially outward and inward motion of k -space sampling, forming a spiral flower-like pattern (Figure 6e) [53, 54]. Since they travel out and back into the center of k -space, they sample the center at various times, making them compatible with multi-echo applications.

3D Shells Trajectory: This 3D trajectory features concentric shells acquired along a 3D spiral path on a k-space sphere (Figure 6 i and j) [55-58]. The Shells are acquired from the center sphere to the outermost k-space sphere, either in one or multiple interleaved shots. The Shells trajectory at an inner radius close to the k-space center can be sampled using a single readout (Figure 6i), while at a large k-space radius requires multiple shots (Figure 6j) [57].

3D Cones Trajectory: 3D Cones adopt a conical, fan-like acquisition pattern, extending from k-space's center, capturing a broad range of angles and radial lines [59-69]. The surface of a Cones is traversed along a spiral emanating from the center as depicted in Figure 6h. Often multiple spirals on a single cone are needed to satisfy the Nyquist sampling distance. K-space sampling can be spread out so Cones acquisition endpoints are distributed along a phyllotax distribution of points on the k-space sphere [59]. This allows for more k-space coverage per shot and further robustness to motion.

3D Yarnball or Spiral Trajectory: A continuous smooth trajectory which spirals from the center of k-space to the periphery inspired by the winding of a ball of yarn was proposed by Stobbe et al in 2020 [1]. The spiral-out trajectory is created by solving a set of ordinary differential equations which describe the motion around a loop increasing in radius from the center to the edge. They parameterize the motion by separating the points along the loop in the polar direction into spokes and the number of points along the azimuthal direction into discs. Figure 8 shows examples of the Yarnball trajectory for two different readout durations. Using this trajectory, the k-space sampling density is non-uniform, reaching up to 10-times oversampling along the k-space's z-axis. The Yarnball trajectory was implemented at 3T to acquire fully sampled T1-weighted brain images of 0.72mm isotropic resolution in 98 seconds, with no parallel-imaging or undersampling artifacts, as shown in Figure 10.

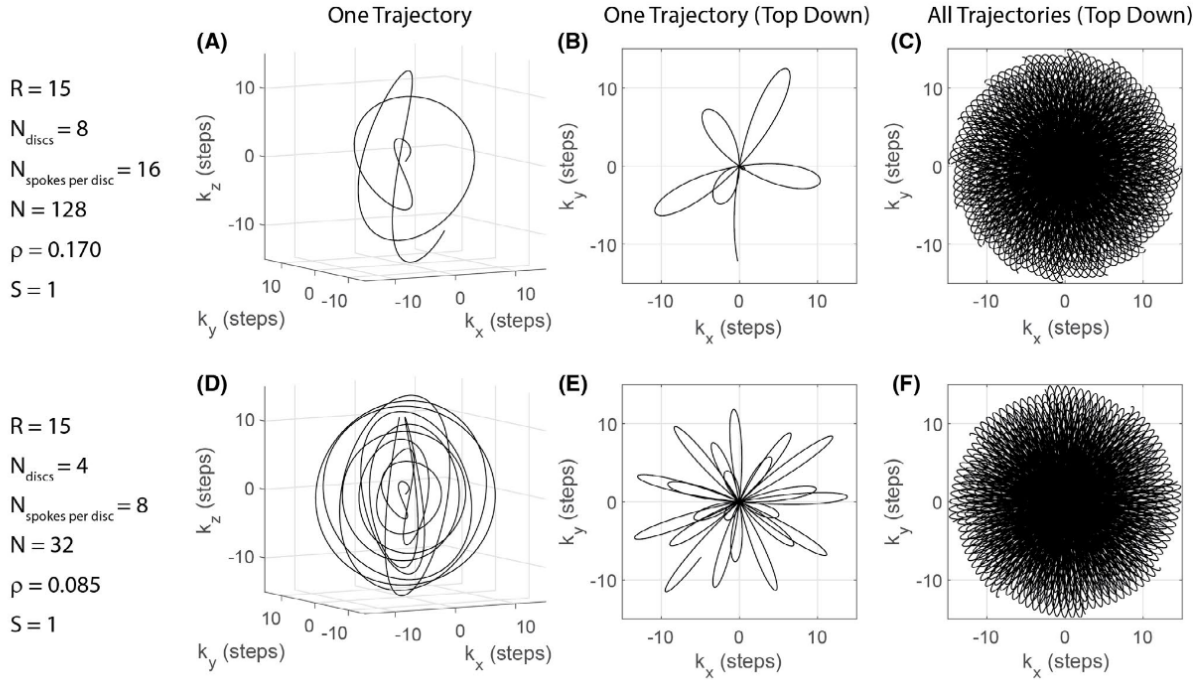


Figure 8: Two designs of the Yarnball trajectory, both with the same 3D matrix size of R . The top row shows a trajectory with a greater number of shots (128) and a shorter single trajectory arch length. The bottom row contains less shots (32) but a longer trajectory [1].

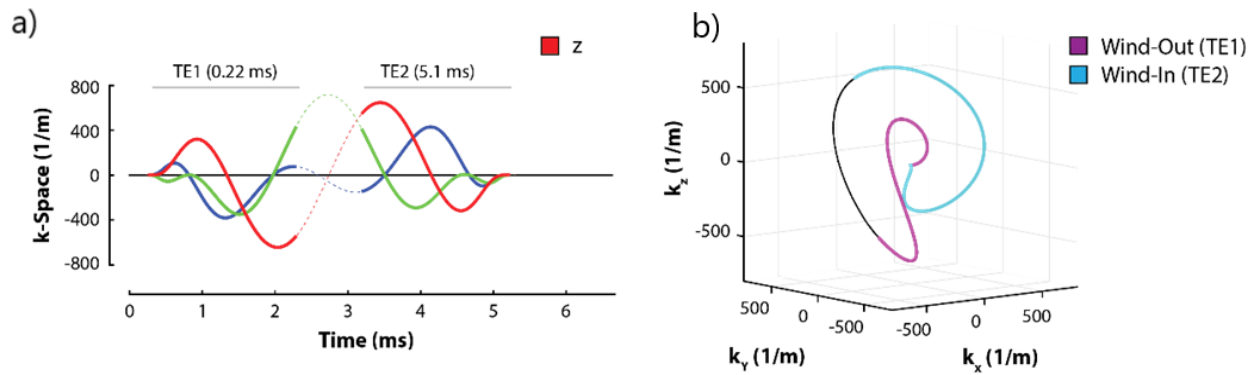


Figure 9: The dual-echo wind-out-in Yarnball trajectory gradient waveforms (a) and k -space locations (b)[70].

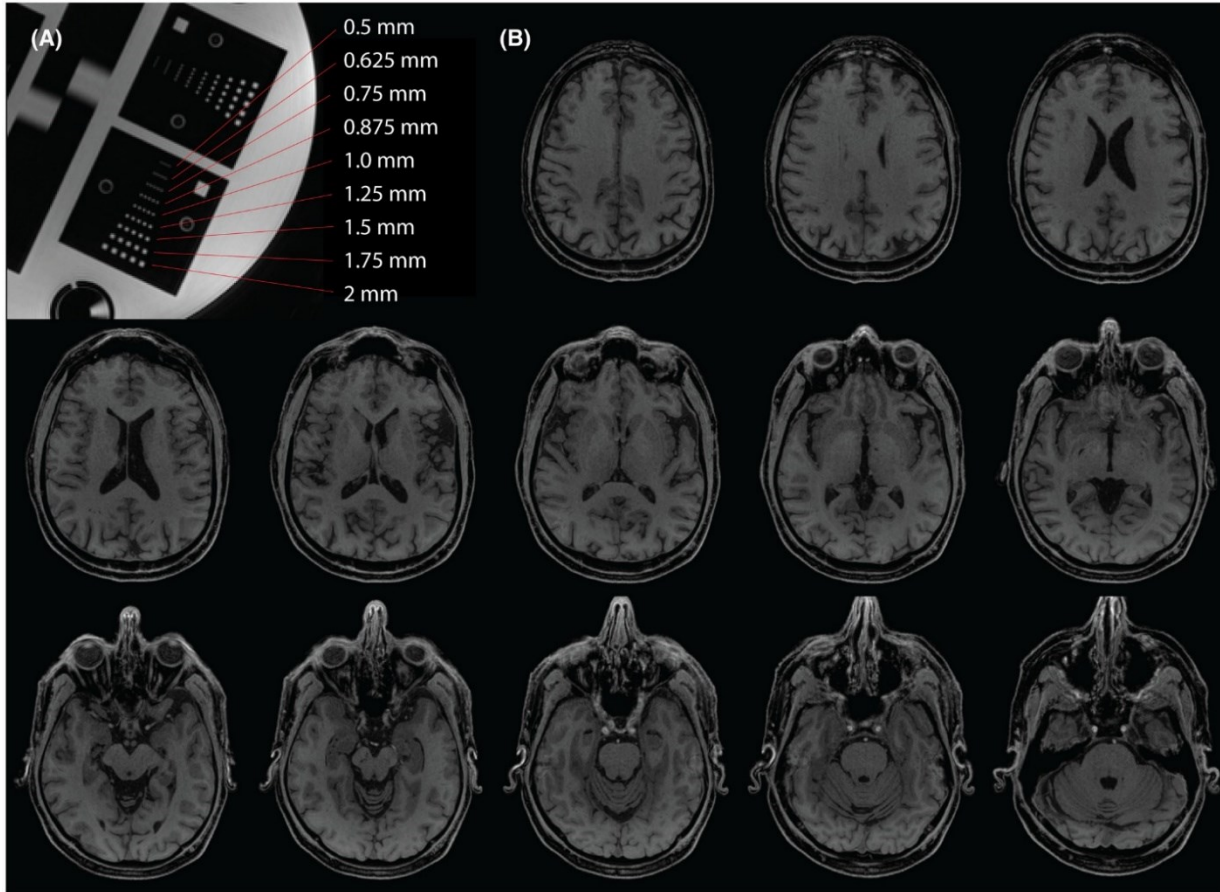


Figure 10: 0.72 mm isotropic T1-weighted images of a phantom (A) and a healthy volunteer (B) acquired in only 98 seconds using a 3D Yarnball trajectory of 10ms on a 3T Siemens Prisma scanner with no parallel imaging [1].

A dual echo Yarnball trajectory has also been implemented by extrapolating the single-echo Yarnball design to spiral back in from the periphery to the center of k-space, producing two images characterized by different echo times (Figure 9b) [70, 71]. The gradient waveforms in Figure 9a show smooth gradients and a transition section between the first and second echo.

A trajectory that is similar in shape to the Yarnball is the 3D Seiffert spiral which samples 3D k-space using a center-out Jacobian elliptical-based trajectory [11]. The trajectory is created by modulating the radius of a Seiffert spiral on the surface of a sphere from the center to the maximum k-space position. The trajectory design parameters and the positions of the interleaves with respect to each other are selected to ensure a uniform spread of points in the 3D volume, quantified using the discrepancy measure of a set of points [72, 73]. Minimizing the discrepancy of set of trajectory points leads to a more uniform sampling of k-space. Figure 11

shows a single interleave of the 3D Seiffert spiral with a 3.0ms readout duration and two different radial densities. The shots are created by rotating a single trajectory so the endpoints along the k-space sphere align with the Fibonacci lattice as shown in Figure 7b. This contrasts with the Yarnball trajectory where a set of differential equations is solved to meet the Nyquist condition between all interleave points. For the Seiffert spiral, each interleave is rotated differently about its axis until the discrepancy is minimized and trajectories overlap the least. Since the Nyquist condition is not inherently met between interleaves in the Seiffert spiral as it is in the Yarnball, a Nyquist test in the form of a nearest neighbor distance search is applied to a sample of k-space points and the number of shots is adjusted accordingly.

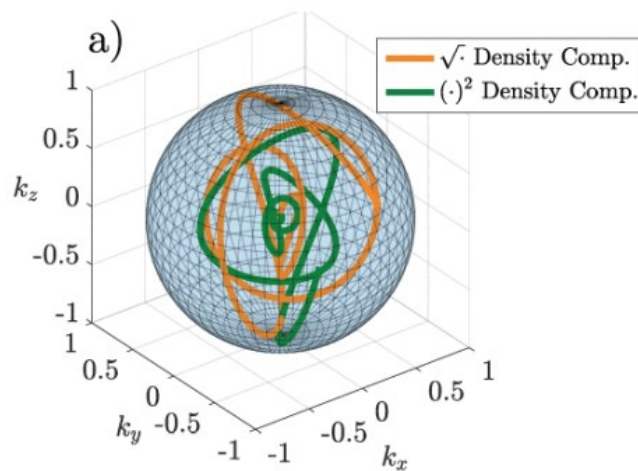


Figure 11: Single shot of the 3D Seiffert spiral trajectory for two different radial density compensation functions. Both Trajectories have a 3.0ms read-out duration, with a maximum gradient magnitude of 30mT/m and a slew-rate of 180 T/m/s [11].

SPARKLING Trajectory: SPARKLING is a trajectory that deviates from the traditional geometric approaches described above. It is instead created by minimizing a cost function while adhering to hardware constraints. The trajectory's speed and velocity constraints stem from the system's maximum gradient amplitude and slew rate. The cost function combines terms related to a target sampling density and terms that prevent gaps and clumps in k-space. SPARKLING can be employed in 2D (Figure 6f) and 3D (Figure 6k) acquisitions, allowing the modulation of the sampled radii along the z-axis to prioritize high SNR in the central region and faster acquisition in the periphery. Ex-vivo and in-vivo scans have demonstrated its potential for producing high-quality images in short acquisition times [74].

Efficient k-Space Sampling

Several of the non-Cartesian trajectories described above efficiently sample k-space due to their smooth gradient waveforms with no sharp turns, leading to shortened scan times [48, 75]. Due to their rapid acquisition, these trajectories are particularly well suited for applications where capturing temporal changes and high-resolution data are essential. The stack-of-spirals trajectory was shown to be up to 4 times faster than Cartesian readout when acquiring T2-weighted images of the brain despite requiring more shots [50]. Since spirals traverse more k-space as they move from the center to the periphery, they are up to 12 times faster than radial sampling for T2-weighted brain imaging [50].

This gain in k-space sampling efficiency is enhanced for true 3D trajectories in comparison to Cartesian sampling. A fully sampled 3D Shells acquisition with partial Fourier reconstruction was able to produce 1.5 times faster scan time compared to the Cartesian MP-RAGE sequence with the compromise of lower SNR [55]. The 3D SPARKLING trajectory showed comparable image quality to Cartesian with 2.5 times faster acquisition for a 0.6mm image acquired at 7T [74]. Unlike line-by-line Cartesian and radial readouts, 3D non-Cartesian trajectories such as Cones and Shells have longer readout times, enabling more data acquisition within a single TR and decreases in scan time [69].

The yarn trajectory introduced by Irarrazabal et al. produces comparable scan times and 9% fewer shots than the 3D Cones trajectory, only surpassed in scan time by Shells, stack-of-spirals, and other density compensated optimized variants of Cones and Spirals [69]. The Yarnball by Stobbe et al. [1] and the Seiffert spiral [11] trajectories both showed improved sampling efficiency in comparison to Cones. The Yarnball trajectory was used to acquire T1-weighted images of the brain 1.4 and 1.8 times faster than Cones for 2ms and 10ms readout durations, respectively, without any image artifacts [1]. Seiffert spiral knee images at 0.85mm resolution were also compared to Cones. The Seiffert spiral trajectory resulted in a 1.7 times shorter scan time than the cones. When compared to a 2D spiral rotated by the tiny golden-angle acquisition scheme in the polar and azimuthal axis, the Seiffert spiral showed a more efficient spread of points leading to a 2 times shorter scan time [76].

Undersampling K-Space

Long acquisition times are often mitigated by undersampling k-space. Unlike the skipping of lines common in Cartesian undersampling [77], 3D NC trajectories can undersample k-space in all 3 dimensions and spread out aliasing artifacts [78]. Spirals, Cones, Yarnball, and Seiffert spiral trajectories all contain diffuse circular artifacts in all image directions, seen in Figure 14, reducing their impact on diagnostic image quality [1, 11, 78]. Artifact incoherence also enhances the effectiveness of compressed sensing image reconstruction techniques, enabling the use of higher acceleration factors [79-81]. For example, Seiffert spiral images of the knee were reconstructed for an undersampling factor of $R = 8$ using compressed sensing and contain diffuse noise-like artifacts seen in Figure 14b, while the Cones trajectory shows blurring and ghosting artifacts [11]. Compressed sensing performs better on the Seiffert spiral images due to the incoherence of aliasing, whereas it is not able to remove the coherent aliasing artifacts from the 3D Cones acquisition (Figure 12).

NC trajectories have also demonstrated compatibility with parallel imaging techniques for the reconstruction of undersampled k-space [78]. NC trajectories have demonstrated lower g-factor values, which relates the aliasing with the differences in coil sensitivities and dictates the decrease in SNR after the application of parallel-imaging algorithms. The lower g-factor penalty of NC than Cartesian sampling is due to common properties of many NC trajectories [82]. This includes the division of undersampling between k-space directions enabling the coil sensitivities to be used more effectively, and the oversampling of the centre of k-space leading to completely captured centers even with large acceleration factors, common in the PROPELLER, Cones, Seiffert spiral and Yarnball [82].

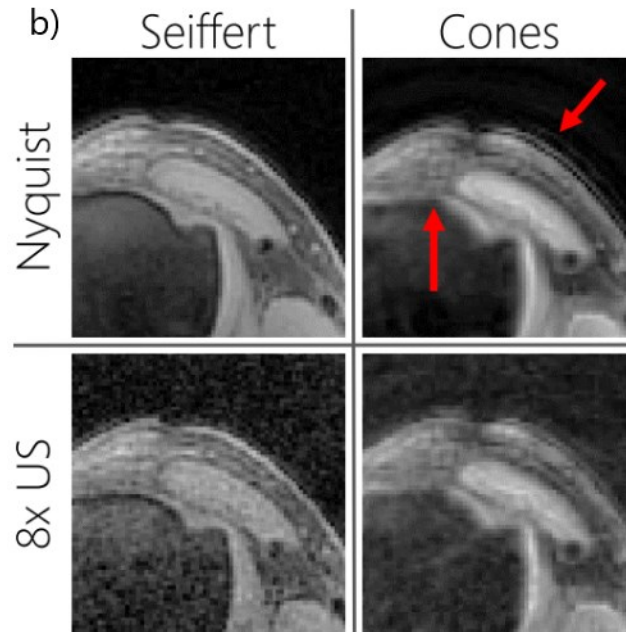


Figure 12: Close up of the axial Nyquist and 8-fold undersampled Seiffert and 3D Cones images of the knee[11].

Motion Robustness

Since the low spatial frequency information of the imaged object is stored at the center of k-space, sampling it during each shot results in signal averaging throughout the scan and decreases sensitivity to motion. For this reason, any trajectory that samples the center at different time points contain motion mitigation capabilities. Spirals have demonstrated robustness to motion artifacts compared to Cartesian trajectories [46], and density compensated spirals showed even further improvements [52]. Similarly, radial trajectories are notorious for their motion robustness. Stack-of-stars have been used at 1.5 and 3T for T1-weighted imaging, showing lower sensitivity to motion, with artifacts that have a lesser impact on diagnosis [83].

The unique design of the PROPELLER trajectory includes 2D blades that sample the central area of k-space at multiples time points, allowing comparisons between blades to remove rotational and translational motion [36, 43]. This trajectory is thus self-navigated.

3D trajectories such as Shells and Cones contain multi-layered sampling schemes which extend outward from the center, facilitating motion correction [56], [59, 62]. The Cones trajectory

shows similar motion correction properties to the 3D radial sampling trajectory, with up to 2 times shorter scan durations and higher SNR [69]. Yarnball and Seiffert spiral trajectories also enable motion correction by virtue of design, although this has not yet been demonstrated.

TE Flexibility and Improved SNR

Since the center of k-space is sampled at the beginning of the spiral, radial, Shells, Cones, Yarnball, and Seiffert spiral trajectories, they are able to achieve a short TE. This allows for T2- or T2*-weighted images with very little signal decay, resulting in a higher SNR [50]. Stack-of-spirals has been used to acquire 3D T2-weighted images of the brain at 0.86mm and showed better visualization of short-T2 tissues such as the nose cartilage, the eye optic nerve, and the brain meninges and parenchyma [50]. Similarly, cones acquisitions allowed for rapid signal decay to be captured in human brain sodium imaging [61] and demonstrated higher SNR than radial trajectories [69].

Shells offer control over angular and radial coverage levels resulting in TE flexibility [55, 57]. The brain's tissue contrast can be improved by adjusting the acquisition order of the Shell interleaves to synchronize the center of k-space sampling with the peak of the contrast, resulting in improved contrast-to-noise ratio compared to the Cartesian trajectories [57]. The Yarnball trajectory design is also flexible and can be adapted for multi-echo data acquisition. Dual echo T2*-weighted images of the knee were acquired using a Yarnball with TEs of 0.22ms and 5.1ms to visualize the ligaments and menisci [70]. An even shorter TE of 0.07ms along with a second echo at 2.79ms was acquired to capture water density of the lung [71].

2.6 Image Quality and Artifacts

Image artifacts are any errors or distortions in the image due to numerous causes relating to the k-space sampling pattern, magnetic field distortions, patient motion or implants, and many other phenomena. Artifacts can degrade image quality or be confused with pathology.

Aliasing artifacts occur when the sampling rate of the signal is not fast enough to capture the true frequencies in the emitted waveforms. The Nyquist criterion in MRI is that the k-space samples must be $1/\text{FOV}$ or less apart.

In addition, MRI images can be prone to various other forms of image artifacts originating from distinct sources. Magnetic gradient field distortions occur during imaging due to eddy currents arising from rapidly switching magnetic field gradients, concomitant magnetic fields, and gradient non-linearity. The distortions cause deviations between expected and actual k-space locations, and manifest as distortions and blurring in the images. Understanding and addressing these artifacts are critical for improving the diagnostic utility of MRI and ensuring the accuracy and precision of clinical and research applications.

Image artifacts in Cartesian acquisitions predominantly occur along the phase encoding axis due to the sampling rate being much lower than in the frequency encode direction. The artifacts caused by k-space undersampling, gradient imperfections, and B_0 field inhomogeneities are easily recognizable in line-by-line Cartesian imaging and EPI, appearing as image duplications shown in Figure 13a-b, and blurring in Figure 13d. These same sources of artifacts manifest themselves differently in non-Cartesian acquisitions, depending on the sampling trajectory in k-space.

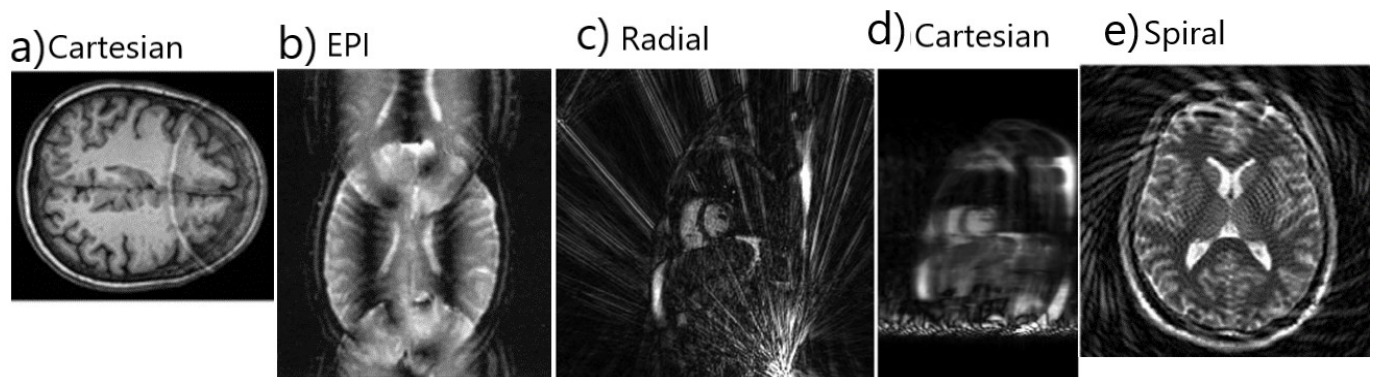


Figure 13: Cartesian and non-Cartesian imaging artifacts. A) Presence of a moderate wrap-around artifact due to undersampling of Cartesian k-space data [77]. B) Ghosting artifacts in EPI [84]. C) Streaking artifacts caused by radial sampling compared, d) Cartesian sampling which contains signal spreading in the phase encode direction [38]. E) 2 times undersampled aliasing artifact of spiral trajectory [79].

Radial sampling suffers from streaking artifacts (Figure 13c) which typically arise from off-resonance [38, 85, 86]. 3D spokes acquisitions with golden-angle radial sampling are more sensitive to eddy currents due to the need for fast and large gradient switching in golden-angle rotations [38]. Shells trajectories exhibit shading artifacts at the image peripheries due to gradient imperfections and eddy currents causing the actual k-space locations to deviate from

their expected values [55, 57]. Due to its hybrid nature, the propeller trajectory contains a combination of EPI and radial artifacts leading to some ghosting and radial streaks [44].

Spiral, Rosette, Yarnball, and Seiffert spiral acquisitions require longer read-out times making them more sensitive to image blurring due to magnetic field imperfections and T2* signal decay. These effects are more pronounced at 7T, leading spirals to have a decrease in resolution of 13-30% at 7T, compared to 6-12% at 1.5T [50].

The Yarnball point-spread function (PSF) is narrower, corresponding to a higher true resolution, compared to the cones trajectory (Figure 14a)[1]. A 4 times undersampled Seiffert spiral trajectory has a single peak in its PSF whereas the equivalent cones PSF contains additional ripples emanating outward (Figure 14b), indicating that the Seiffert spiral sampling artifacts are less coherent and more diffused than in cones [11] (Figure 14b).

Image simulations in Figure 15 compare Yarnball and cones image artifacts for various undersampling rates; from fully sampled to 75% sampled. Yarnball images in Figure 15A- D show circular blade-like artifacts distributed around the periphery of the FOV. Cones images contain artifacts for fully-sampled k-space (Figure 15E) that persist up to 1.87 oversampling rate (Figure 15F-H).

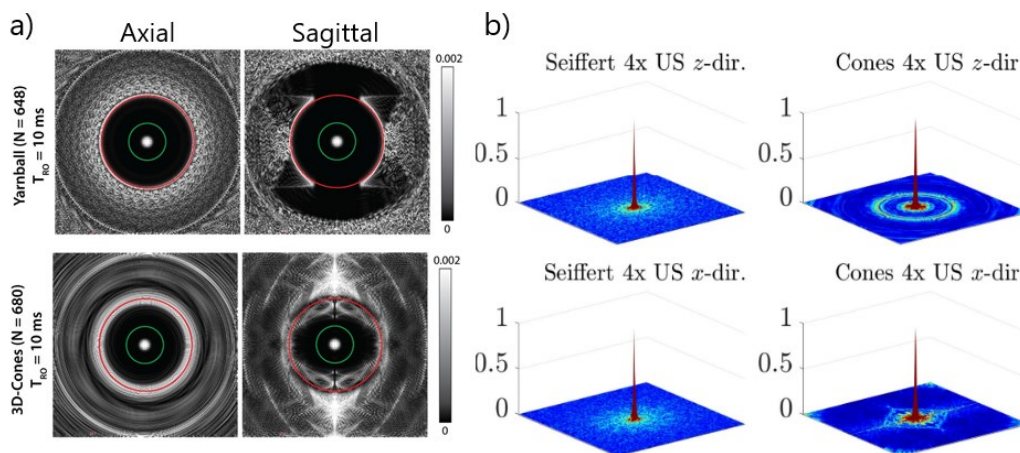


Figure 14: PSF of a) Yarnball (top row) and 3D cones (bottom row). The FOV is indicated by the red circles. The right column is the relative intensity of pixels outside the green area [1]. b) Simulated PSF for 4X undersampled Seiffert (left column), and 3D cones (right column) along the z and x directions [11].

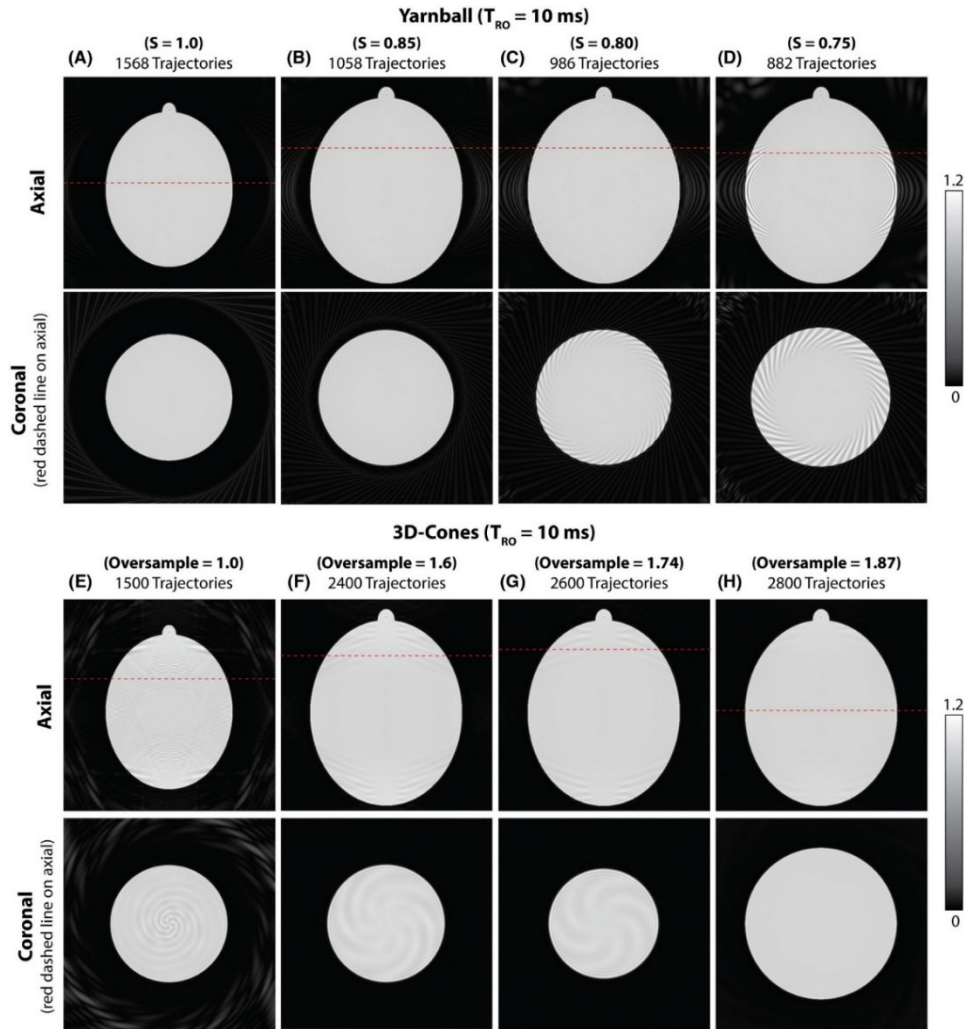


Figure 15: Simulated images comparing the Yarnball and cones trajectory to depict the appearance of artifacts [1].

2.7 T_2^* Mapping with Non-Cartesian Trajectories

NC trajectories are promising for multi-echo imaging due to their robustness to motion, shorter acquisition times, higher SNR, and non-coherent aliasing patterns in comparison to Cartesian acquisitions. For instance, Cones have been used to acquire multi-echo T_2^* -weighted data due to their short echo times allowing for earlier sampling of the FID and capturing short T_2^* tissues [66]. Susceptibility maps reconstructed from the Cones images are shown in Figure 16, showing values corresponding to the literature. The adaptability of cones allows for the readout time to be elongated to shorten total scan time, but this is at the cost of image blurring and reduced sensitivity to high resolution features of short T_2^* tissues [66, 69]. Cones can suffer from

streaking artifacts, which can be observed as elevated susceptibility in the QSM, highlighted by the red arrow in Figure 16a [66].

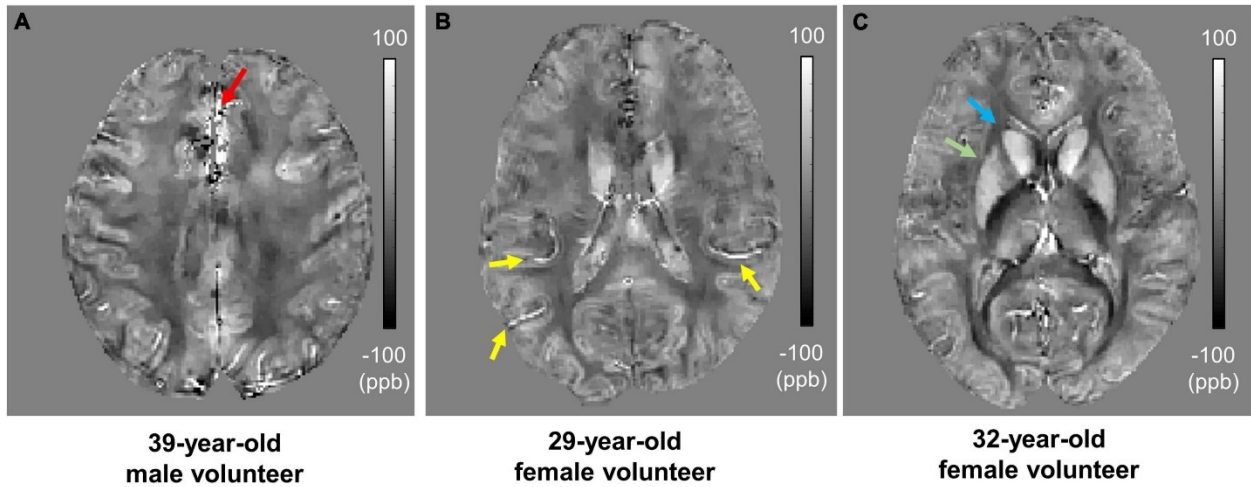


Figure 16: In vivo ultrashort echo time quantitative susceptibility mapping (UTE-QSM) with Cones trajectory of three representative healthy volunteers. (A) 39-year-old male, (B) 29-year-old female, and (C) 32-year-old female. The estimated susceptibility maps show a clear contrast between different tissues including the white matter, gray matter, vessels (yellow arrows), caudate (blue arrow), and putamen (green arrow)[66].

2D Rosettes have been used for T2* mapping by partitioning each petal of the Rosette into a different echo time readout, for a total of 5 echo acquisitions [54]. To ensure complete sampling of k-space, the trajectory shots are created by rotating the multi-echo Rosette in the 2D k-space plane using golden angle rotations. Their resulting images showed less image motion artifacts during free-breathing and failed breathe hold compared to Cartesian imaging of the heart and liver (Figure 18).

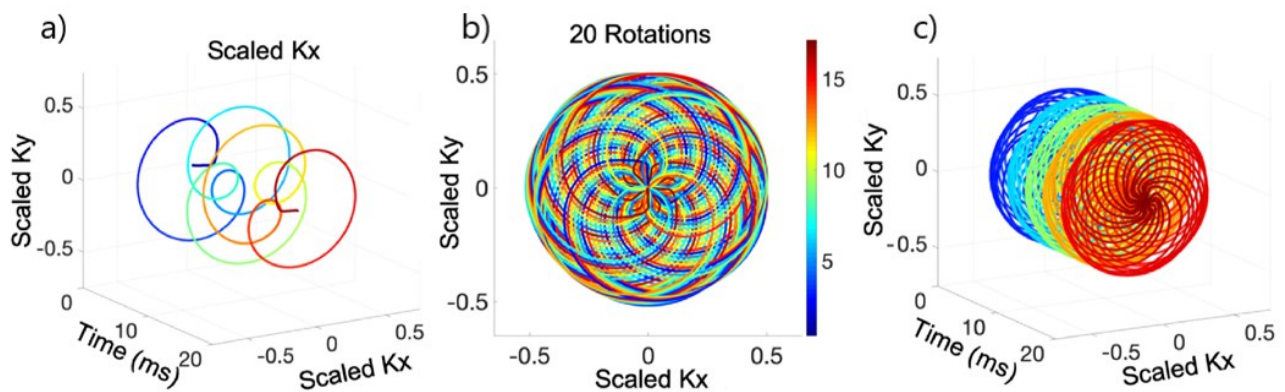


Figure 17: 2D Multi-Echo Rosette trajectory showing a) pedals collected during one TR contributing to different echoes, b) the trajectory rotated along the 2D plane to fill k-space, and c) the fully acquired k-space during multiple shots of the rosette trajectory for each echo time [54].

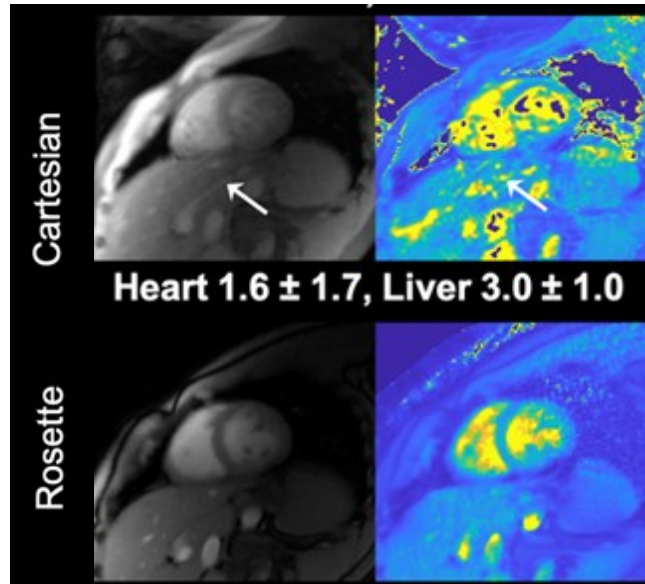


Figure 18: Single subject $T2^*$ weighted imaged along with the $T2^*$ map from it's respective multi-echo sequence during free-breathing and failed breath-hold conditions. White arrows show locations of motion artifacts more prevalent in Cartesian sampling than rosette [54].

Lastly, stack-of-spirals has been used for whole-brain 1mm resolution $T2^*$ mapping at 3T. The multi-echo spiral sequence was made by concatenating 5 center-out spiral trajectories with 10ms delays between consecutive echoes to allow for transition between spirals, i.e. returning to the centre of k-space [47]. Spirals were able to achieve 8 times faster scan times than Cartesian imaging, combined with an undersampling factor of 2 for a total of 16 times faster scan time than Cartesian imaging without compromise in SNR. Some blurring artifacts were present in the spiral scans due to off-resonance, gridding, and the circular acquisition of the trajectory. Figure 19 shows $R2^*$ ($1/T2^*$) maps created from the multi-echo stack-of-spirals data acquired at 1mm and 0.5mm [47], showing the potential of NC trajectories for high-resolution $T2^*$ mapping of the brain.

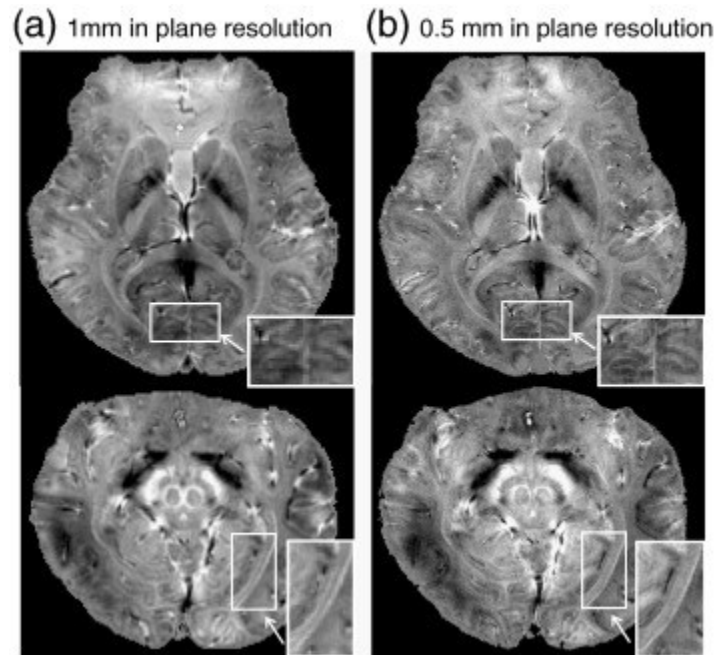


Figure 19: $R2^*$ ($1/T2^*$) maps of the brain acquired using a stack-of-spirals depicting possibility for 1mm and 0.5mm acquisition at 3T [47].

Not all trajectories lend themselves well to being multi-echo, as they require non-smooth transitions between echoes. This can lead to inefficiencies due to gradient limitations and peripheral nerve constraints. For instance, multi-echo radial trajectories require inefficient, sharp changes in trajectory direction to reacquire the same spoke and/or move to the next one [87]. Multi-echo cones acquisitions required returning from the periphery of k-space to the center to acquire each subsequent echo [65]. On the other hand, the Rosette and dual-echo Yarnball trajectory allows for smooth gradient transitions and constant acquisition between echoes [54, 70, 71]. The spiral can also be wound-out and back in for a smooth and continuous acquisition of k-space and multiple echoes [88].

2.8 Image Reconstruction of Non-Cartesian Trajectories

An inverse discrete Fourier transform (DFT) converts a sequence of equally spaced k-space samples to the image domain, however, is often too slow to be practical. The fast Fourier transform (FFT) factorizes the DFT matrix into a product of sparse factors, thus reducing the computation complexity from the order of n^2 to the order of $n \cdot \log(n)$, where n is the data size [89]. Unlike Cartesian grids, non-Cartesian trajectories sample k-space non-uniformly. As a

result, traditional FFT reconstruction methods may not apply directly, and alternative image reconstruction techniques are required [90].

One common approach called non-uniform fast Fourier transform (NUFFT) involves resampling acquired non-uniform k-space data onto a Cartesian grid, a process referred to as *gridding*, to make it compatible with traditional FFT [91]. When some spatial frequencies are overrepresented compared to others by a trajectory, a correction is required in the form of a weighting on each discrete frequency component called a *density compensation function (DCF)* [90]. This can be calculated using Vorronoi tessellation dividing the k-space into polygons or using iterative methods [90]. The effects of the DCF on image reconstruction to generate sufficient image quality has been shown on NC trajectories, particularly in radial [93], BLADE [93], and spiral trajectories [99]. Accurate calculation of the DCF requires accurate knowledge of the NC trajectory, often-requiring trajectory measuring or approximation prior to reconstruction due to hardware imperfections [92-94]. However, some NUFFT implementations use the forward model approach which iteratively minimize an error function and do not require the calculation of a DCF, such as BART's NUFFT[95]. Gridding, however, can introduce interpolation artifacts and may not be sufficient for all applications.

MRI is a slow imaging modality. K-space undersampling is often performed to shorten scan times, improve patient comfort, and limit motion artifacts. However, this may lead to decreased SNR and aliasing artifacts. The latter can be addressed through compressed sensing by exploiting the sparsity of the underlying image in certain transform domains, most commonly wavelet and total variation, to maintain image quality while achieving faster scan times [96]. Compressed sensing relies on non-linear reconstruction algorithms, often based on convex optimization techniques like l_1 minimization, to iteratively reconstruct the image from the undersampled data [96].

Undersampled images can also be restored through parallel imaging by taking advantage of spatial information from coil sensitivities. The SENSE reconstruction method is implemented in the image domain, where each aliased pixel is expressed as the addition of the coil sensitivities and gradient spatial encoding trajectory, the unaliased image is then iteratively solved using the

conjugate gradient method [78] [97]. This is a popular iterative method of solving linear equations due to its fast convergence [78]. GRAPPA is an alternative parallel imaging method applied in the k-space domain by posing the reconstruction as an interpolation problem. Unacquired k-space values are calculated via a linear combination of acquired neighboring k-space data from all coils [97]. SPIRIT is a combination of these two techniques that constrains the solution to have calibration and data consistency. Calibration consistency involves all synthesized Cartesian k-space points being a linear interpolation of nearby points. Additionally, data consistency involves transforming the synthesized Cartesian k-space back onto the acquired Non-Cartesian data and evaluating their agreement [78]. This was further improved upon by ESPIRIT, which estimates the coil sensitivity maps directly using eigenvalue decomposition [97]. ESPIRIT demonstrated the ability to extract high quality sensitivity maps and combines the high reconstruction quality and straightforward extension to non-Cartesian sampling of SENSE, with the noise robustness of GRAPPA [97].

3 Methods

Based on the properties of the previously discussed trajectories, in particular the Rosette, Yarnball and Sieffert spiral, I have designed a novel trajectory tailored to the fast acquisition of high-resolution, volumetric multi-echo T2*-weighted data for the purpose of T2* and susceptibility mapping of the brain. The peripheries of k-space are undersampled to reduce acquisition time accrued by extra gradient waveforms. Non-coherent aliasing artifacts improve the performance of undersampled image reconstruction. Oversampling the center of k-space is performed at different time points to ensure high SNR and provide motion robustness. A continuous trajectory in k-space with few sharp turns and smooth transitions between different echo readouts leads to hardware compliant gradient waveforms and optimizes acquisition efficiency. The novel 3D multi-echo Seiffert spiral (MESS) trajectory is compared to Cartesian imaging and implemented on a 7T scanner to demonstrate the feasibility of whole brain high-resolution T2* mapping.

3.1 3D Multi-echo Seiffert Spiral (MESS) Trajectory Design

3.1.1 3D Seiffert Spiral

The 3D spiral trajectory is designed as in Spiedel et al [11] using a Seiffert spiral, which dictates a trajectory along a spherical surface with a constant angular velocity and speed using the following equations:

$$\begin{aligned}\rho &= \operatorname{sn}(s, m) \\ \psi &= s\sqrt{m} \\ z &= \operatorname{cn}(s, m)\end{aligned}$$

(Equation 11)

where sn and cn are the Jacobi elliptic functions, the parameter m is a constant between 0 and 1, s is a parameterization of the arch length, and ρ , ψ , and z are the cylindrical coordinates of the spiral points. For a multi-echo k-space trajectory, the Seiffert spiral is partitioned into equal segments, each corresponding to a different echo. The arc length is approximated by the

desired total readout time and the speed is constrained by the maximum gradient amplitude of the MRI scanner.

3.1.2 Radius Modulation

For the single echo case, a spiral-out trajectory is used where the radius is modulated from the center to the periphery of k-space using the following function.

$$T_{3D} = r_{k_{mod}} T_{surf}$$

where $r_{k_{mod}} = \{r_k^\alpha | r_k \in [0, k_{max}]\}$

(Equation 12)

The spiral radius is modulated by an exponential function, where the exponent α will determine the radial sampling density. An α of 1 corresponds to the linear evolution of the spiral along the radius, while an α of 2 corresponds to a parabolic radius modulation which samples more points close to the center of k-space, and an α of 0.5, or 0.1 will sample more points at the periphery of k-space, as shown in Figure 20. All figures showing a single echo Seiffert spiral trajectory are for a 6ms readout, 240mm FOV, 0.8mm target resolution, and $\alpha = 1$ unless otherwise stated. All multi-echo Seiffert spiral (MESS) figures are for a 5 echo, 20ms (4ms/echo) readout, 240 FOV, 0.8mm target resolution, and $\alpha = 2$ unless otherwise stated.

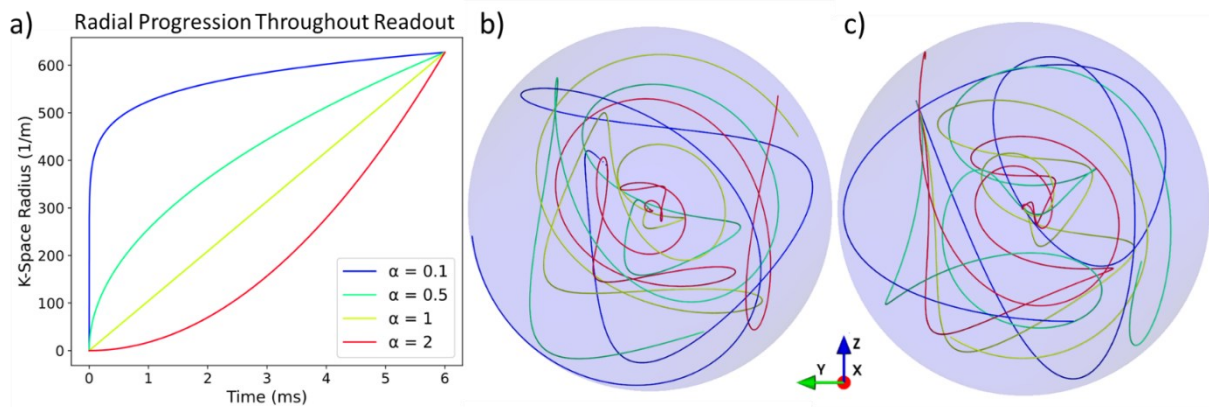


Figure 20: A single echo Seiffert spiral at 4 different α values of 0.1, 0.5, 1, and 2 corresponding to different radial sampling densities. The plot in a) shows the radial progression of the spiral throughout the readout time of 6ms for various α values. The trajectory's shape at the corresponding α values is shown for a b) spiral-out and c) spiral-in trajectory.

For the multi-echo case, the readout trajectory starts at the periphery of k-space, spirals into the center and back out to the periphery for each echo readout. To ensure continuous transitions, the subsequent echoes are a continuation of the same Seiffert spiral that winds in and out multiple times based on the number of echoes required. The echo time associated with each echo corresponds to the midpoint of the spiral-in-out readout trajectory when the centre of k-space is sampled.

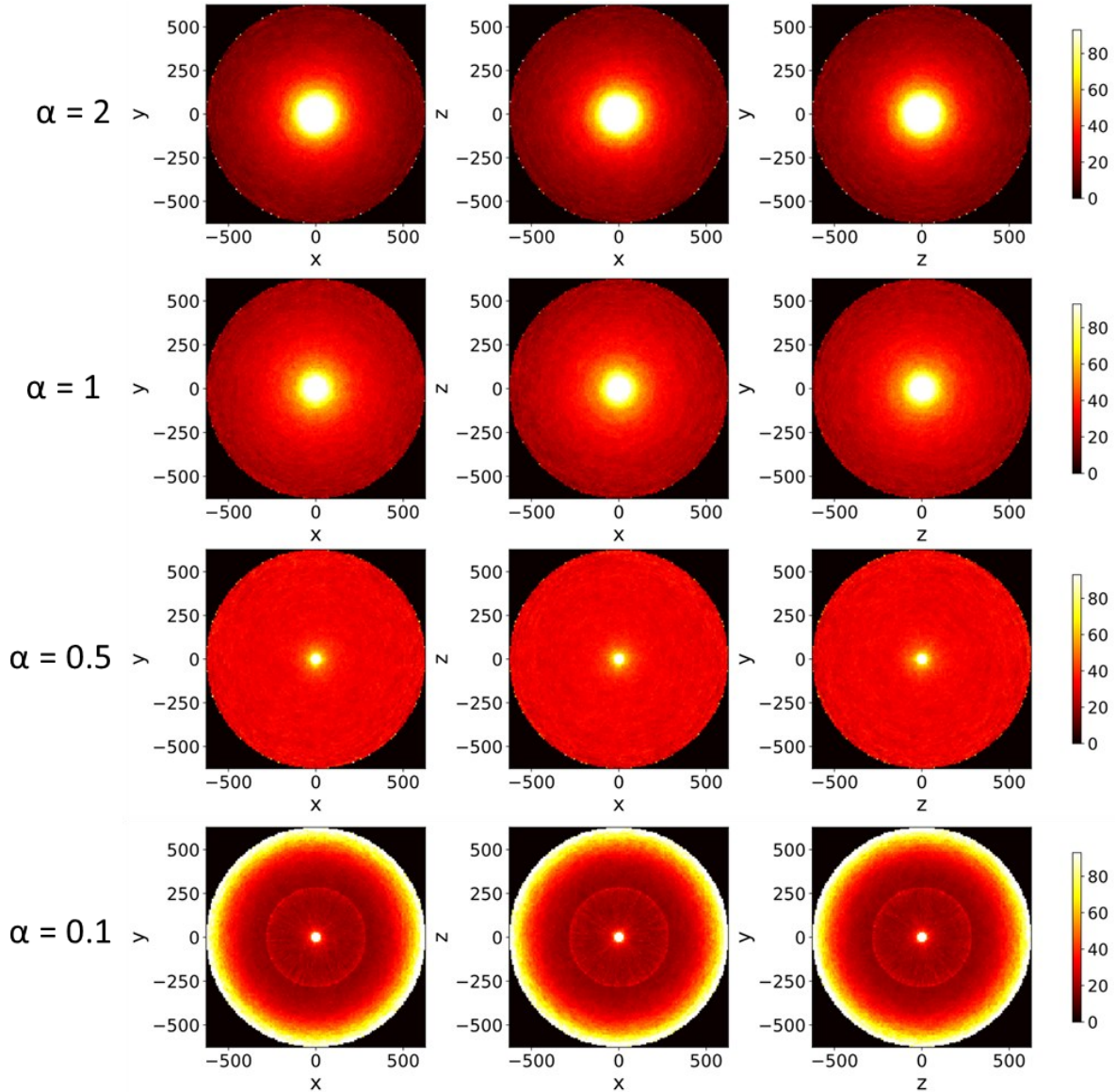


Figure 21: Density of points heatmap along various planes for a single-echo spiral-out trajectory at various α parameters of 2, 1, 0.5, and 0.1.

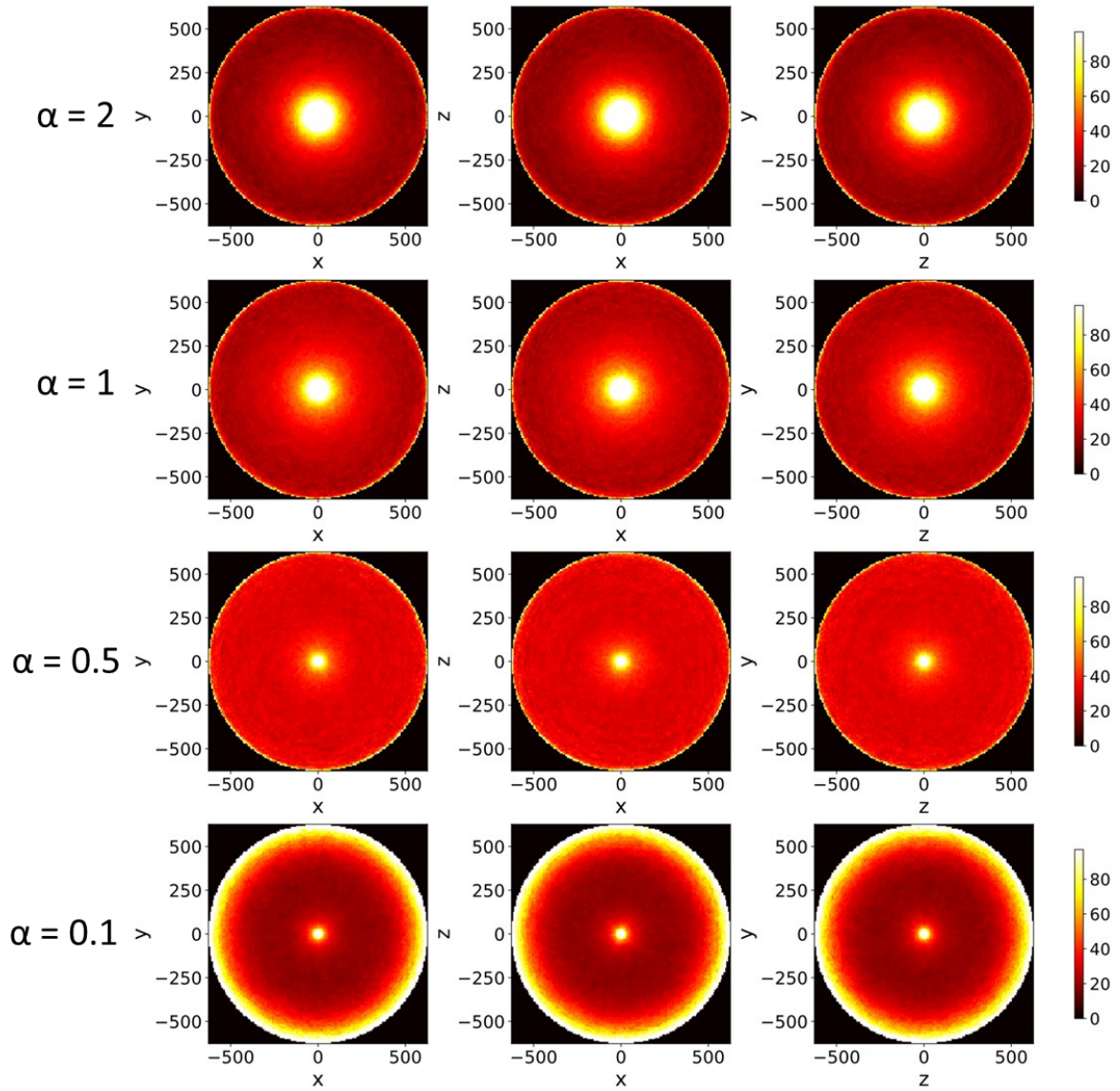


Figure 22: Density of points heatmap along various planes for the first echo of a MESS spiral-in-out trajectory at various α parameters of 2, 1, 0.5, and 0.1.

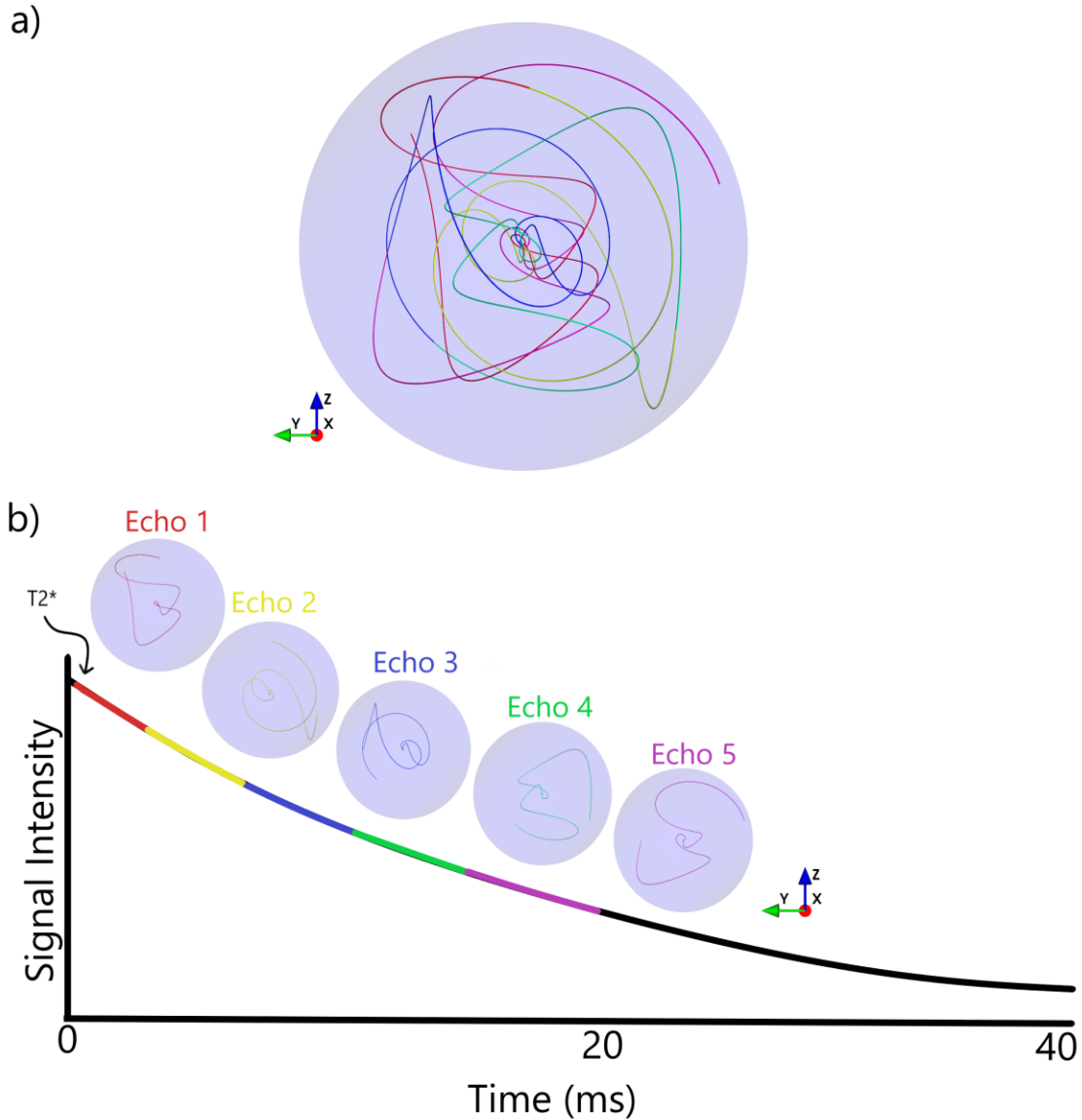


Figure 23: A MESS trajectory showing the wind-in-out pattern, along with b) the echoes separated to demonstrate their sampling time along the $T2^*$ decay curve.

3.1.3 Optimal Sampling Distribution

The m variable in (Equation 11) is set to a value between 0 and 1 that corresponds to the most uniform k-space sampling distribution, which is quantified using the discrepancy (Figure 24) [98] where a lower discrepancy value is associated with a more uniform sampling of points [73]. The discrepancy is measured using the python Scipy Quasi-Monte Carlo library [11, 98]. For a multi-echo trajectory, the discrepancy is calculated for each echo separately and then averaged. The m value corresponding to the lowest average discrepancy is selected to ensure the trajectory is

optimized for the echo ensemble (Figure 25).

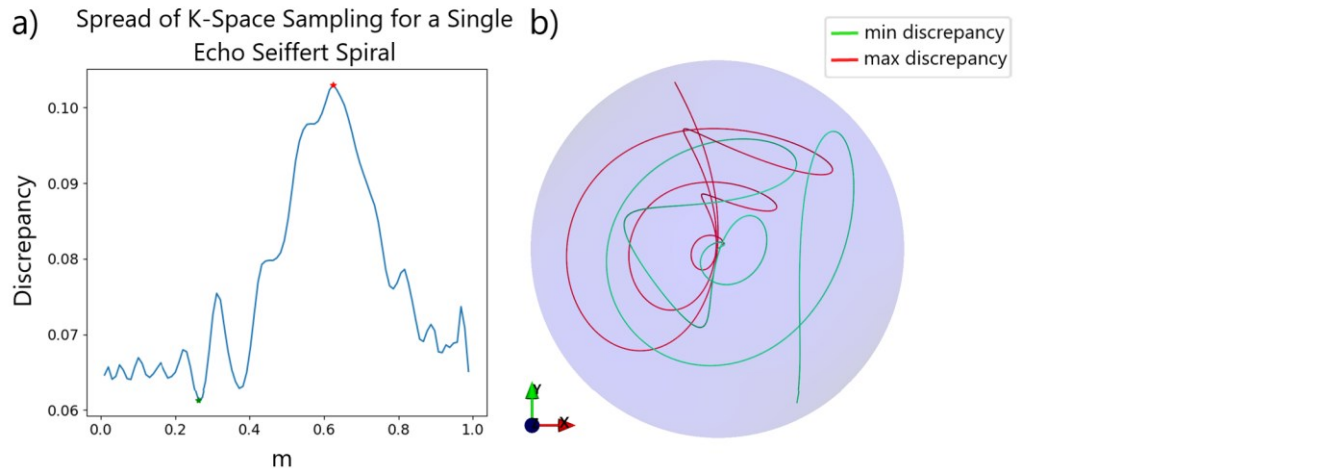


Figure 24: The effect of m parameter modulation on sample distributions in k -space for a single echo Seiffert spiral. The relationship between discrepancy and m are shown in a, while the trajectory with the highest and lowest discrepancies are shown in b.

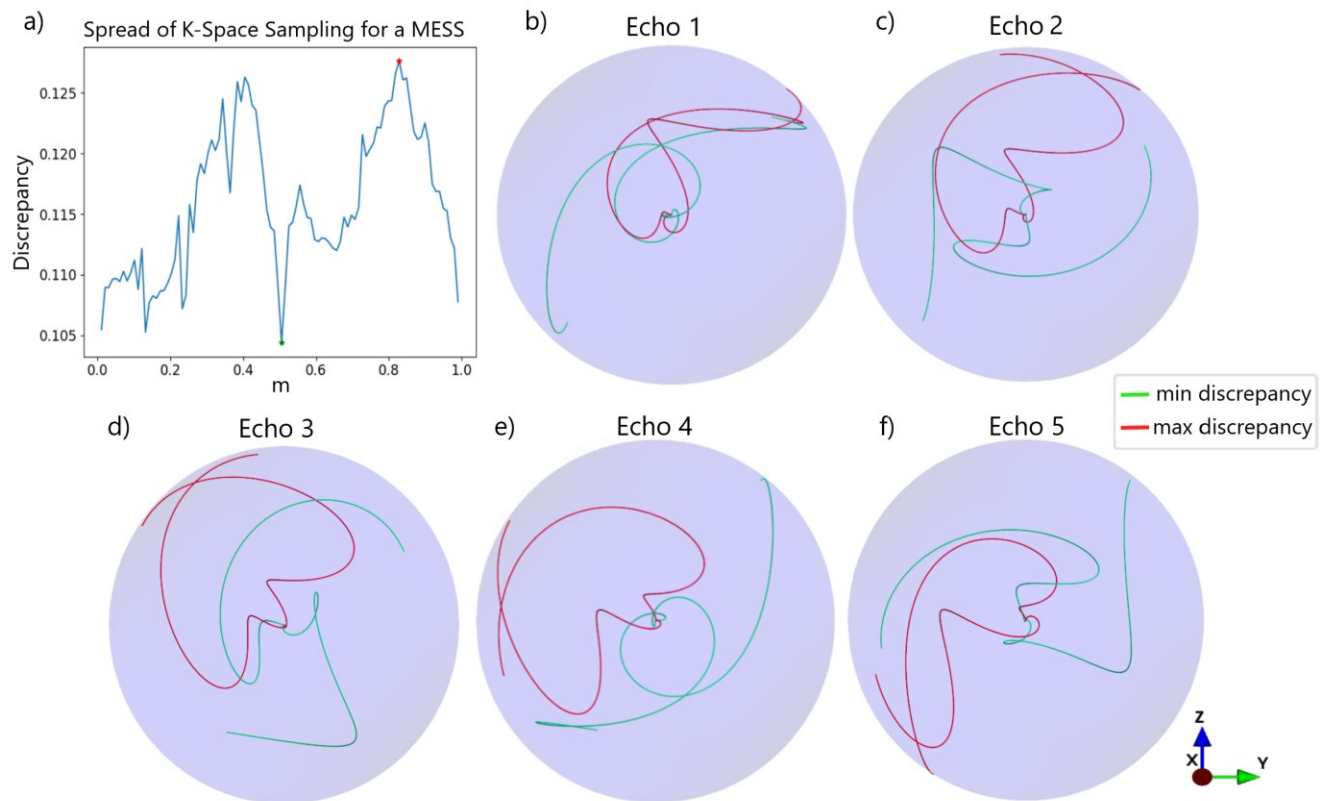


Figure 25: The effect of m parameter modulation on sample distributions in k -space for a MESS. The relationship between the average discrepancy between all echoes and m are shown in a, while the trajectory with the highest and lowest discrepancies for each echo are shown in b to f.

3.1.4 Total Trajectory Arc-Length

The radius modulation will determine the total arc-length S_{tot} travelled during the available readout time $t_{readout}$. The arc-length of the trajectory on the surface of a sphere is initially calculated using the kinematic equation:

$$S_{tot} = v_k t_{readout}$$

(Equation 13)

where the velocity v_k is that required to travel $\Delta K_{nyquist}$ in the sampling time interval determined by the MRI sampling rate. The arc-length $\Delta S_{initial}$ traveled between two points on the surface of a sphere is related to the radius r_k of the sphere by:

$$\Delta S_{initial} = \Delta\theta * r_{k_{initial}}$$

(Equation 14)

The ratio between the two arc-lengths at different radii is equal to the ratio of their radii. The initial radius is unitary ($r_{k_{initial}} = 1$) since the Seiffert spiral is initially constructed on the surface of a unit sphere.

$$S_{tot} = \sum_s \frac{r_{k_{final}}(s)}{r_{k_{initial}}} * \Delta S_{initial}(s) = \sum_s r_{k_{final}}(s) * \Delta S_{initial}(s)$$

(Equation 15)

The distances between neighboring points, $\Delta S_{initial}$, are calculated along the trajectory, then multiplied by their radius ratio, and summed along the trajectory to get the total arc length covered by the 3D trajectory.

3.1.5 Gradient Hardware Compliance

The gradient waveforms corresponding to the k-space trajectory must comply with gradient hardware constraints, including the maximum gradient amplitude and slew rate, relating to the velocity and acceleration of the trajectory, respectively. The gradient waveforms were calculated using the openly available software package by S. Vaziri and M. Lustig [99] for a max amplitude and slew rate of 30mT/m and 180T/m/s, respectively. Consequently, the read-out duration is often modified during the optimization of gradient waveforms. To make sure the

target readout duration is achieved, the total arc length is rescaled, and the gradient waveforms are recalculated iteratively until the gradient waveforms are within $\pm 1\mu\text{s}$ of the target readout time. Figure 26 shows optimized gradient waveforms, corresponding k-space positions, and slew rate for the spiral-out and spiral-in-out winding of a single echo, along with a MESS trajectory. Note that a prephase gradient is required for the spiral-in-out design of the Seiffert spiral since their readout commences at the k-space periphery, seen in Figure 26 b and c.

Oscillations of the gradient waveforms can cause mechanical vibrations, which are particularly strong at the mechanical resonance frequencies of the gradient system and can damage the gradients. We perform a frequency analysis of the gradient waveforms to make sure they are not operating at the *forbidden* mechanical resonance frequencies of the system. The forbidden frequencies of the Siemens Terra 7T MRI system are $550 \pm 50\text{Hz}$ and $1100 \pm 100\text{Hz}$. If any component (x, y, or z) of the gradients has peaks within 15Hz of these forbidden bands, the maximum gradient amplitude and slew rate are incrementally lowered to attenuate and shift the peaks away from the forbidden frequencies. The mechanical gradients of a single echo spiral-in, spiral-in-out and 5 echo MESS trajectory are shown in Figure 27, with gradient peaks away from the red forbidden frequency ranges.

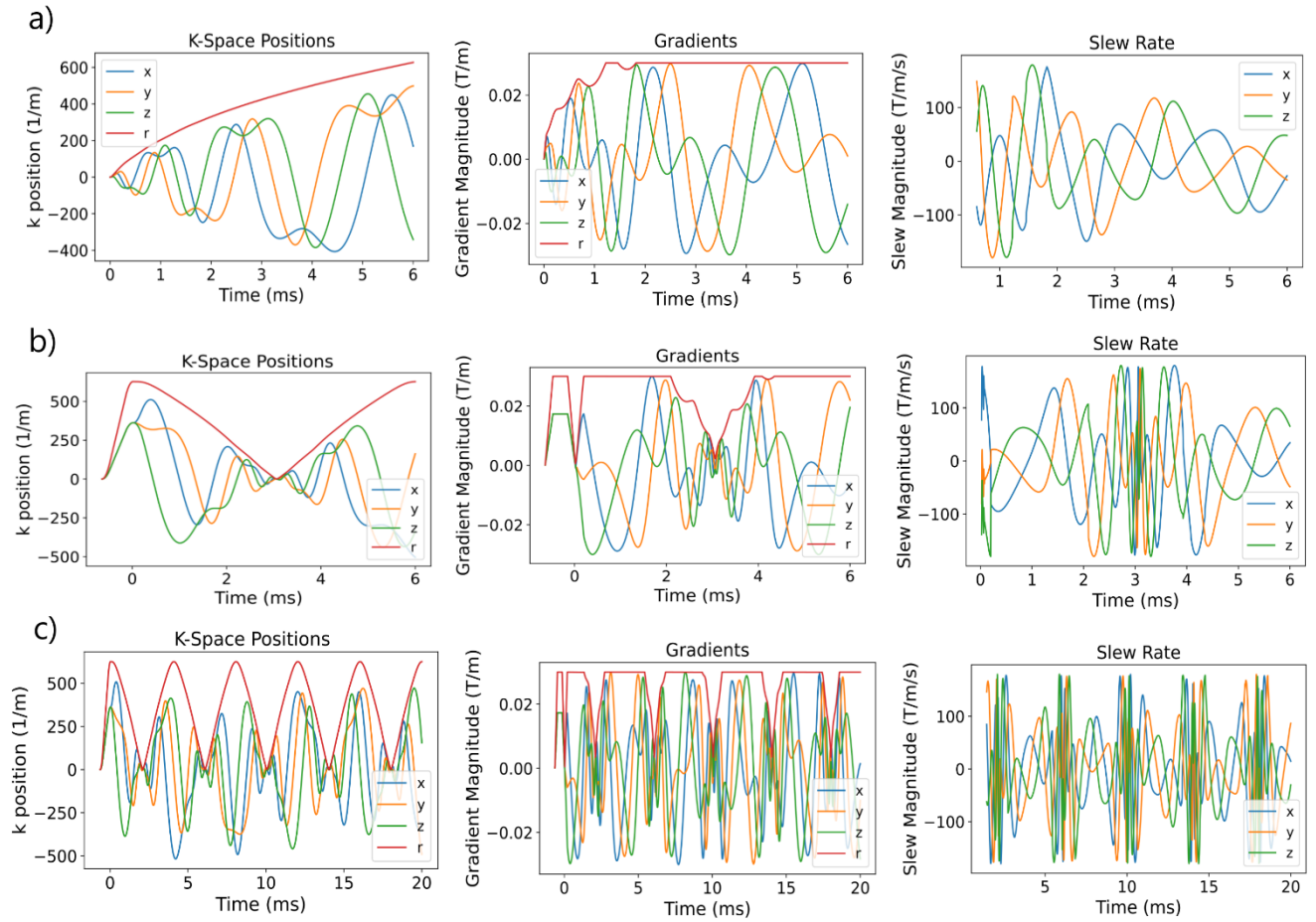


Figure 26: The k -space positions, gradient waveforms, and slew rates of the x , y , and z components of the a) single echo spiral-out trajectory, b) single echo spiral-in-out trajectory, and c) 5 echo MESS trajectory. The spiral-in-out and MESS trajectory include the pre-phasing gradient step that encodes the initial k -space position at the periphery of k -space. The rephrasing step is not included in the acquired MRI data.

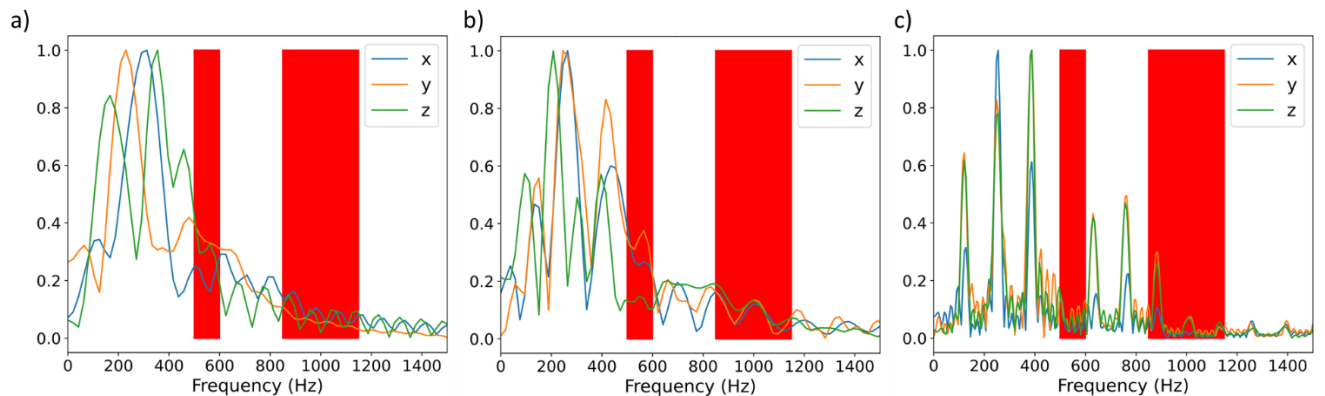


Figure 27: Mechanical Gradients of a) single echo spiral-out, b) single echo spiral-in-out, and c) multi echo Seiffert spiral. The red bars represent the forbidden frequencies ranges, and mechanical gradient peaks in this area should be avoided.

3.1.6 Trajectory Rotations along Fibonacci Lattice

The 3D spiral trajectory is rotated N_{shots} times to sample the whole k-space volume. The N_{shots} endpoints are defined using a Fibonacci lattice with points evenly spaced on the surface of a sphere. The corresponding θ and ϕ rotations are derived from the golden ratio (GR) and the number of rotations [100]:

$$\theta = 2\pi \frac{n}{GR}$$

$$\phi = \cos^{-1}\left(1 - 2 * \frac{n + 0.5}{N_{shots}}\right)$$

(Equation 16)

where n is the current integer rotation from 0 to N_{shots} .

For the single echo case, the rotations are performed along the vector v_o from the origin of k-space to the trajectory endpoint, while for the multi-echo case it is performed along the vector from the center to the endpoint of the first echo's trajectory.

The rotation matrices R for each aforementioned angle θ about an arbitrary axis of rotation v_{axis} are calculated using Rodrigues' formula:

$$R = I + \sin(\theta) v_{axis} + (1 - \cos(\theta))v_{axis}^2$$

(Equation 17)

Where the axis of rotation v_{axis} in this case is v_o . The ϕ azimuthal rotation is applied along a vector perpendicular to two vectors on the sphere. This vector is found by taking the cross product between v_o and a vector on the k-space z-axis.

$$v_{\phi} = v_o \times \langle 0, 0, K_{max} \rangle$$

(Equation 18)

The θ and ϕ rotation matrices are applied to all sample coordinates along the 3D trajectory to create the various shots. Two shots of the single echo and MESS are shown in Figure 28, with black arrows showing the endpoints, or v_o , forming the Fibonacci lattice.

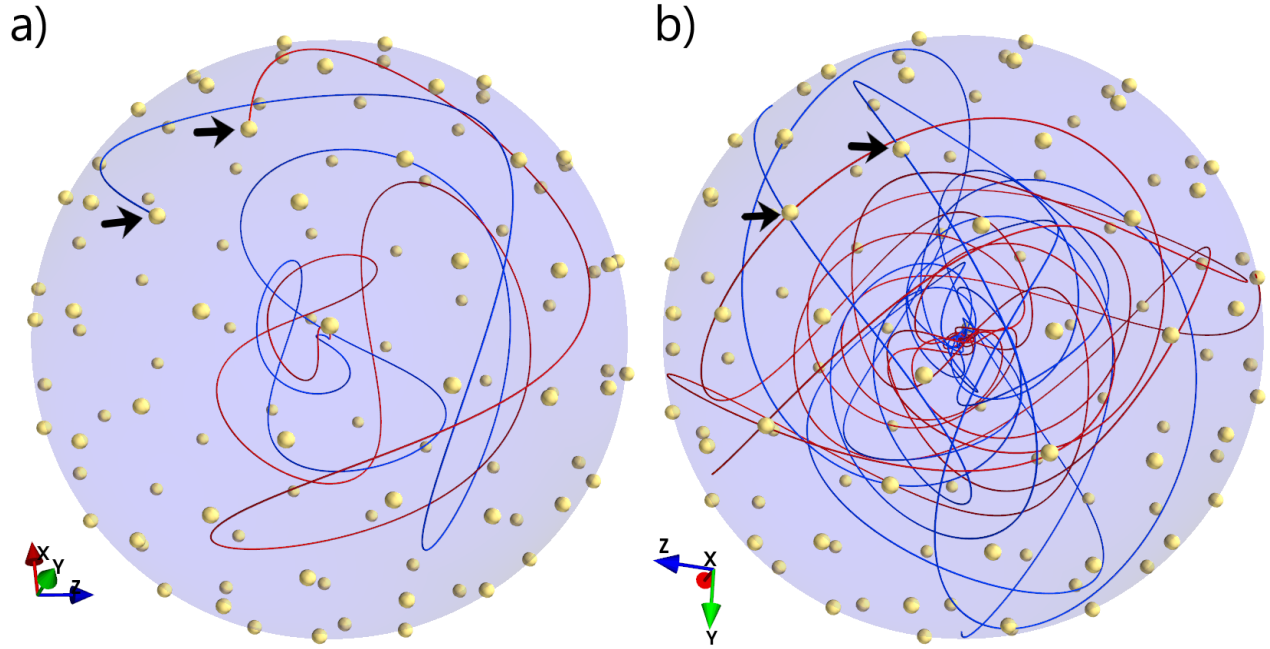


Figure 28: Two shots of the a) single-echo and b) 5 echo MESS trajectory rotation points along the Fibonacci lattice. The rotation point for the single-echo case is the endpoint of the shot, while for the MESS case it is the endpoint of the samples corresponding to the first echo. Only rotation points for 100 shots are displayed for simplicity to demonstrate the Fibonacci lattice on the k-space sphere.

3.1.7 Axis Rotations

Once the N_{shots} trajectories have been rotated to sample 3D k-space, they may converge at certain radii resulting in non-uniform sampling of the area inside the k-space sphere. As shown in Figure 29, without axis rotations, there are ripples of varying density along the radial direction.

To improve the uniformity of 3D k-space sampling, each shot is rotated about its own axis after the Fibonacci rotation by a random angle between 0 and 2π . For a large enough number of shots, this significantly improves sampling uniformity, as shown in Figure 29 and Figure 31. The random axis rotation outperforms two other methods of axis rotations considered: golden angle rotations and evenly spaced rotations determined by:

$$\Delta\theta = \frac{2\pi}{N_{shots}}.$$

(Equation 19)

The axis rotations also lead to consistently uniform k-space sampling across echoes, displayed in Figure 30.

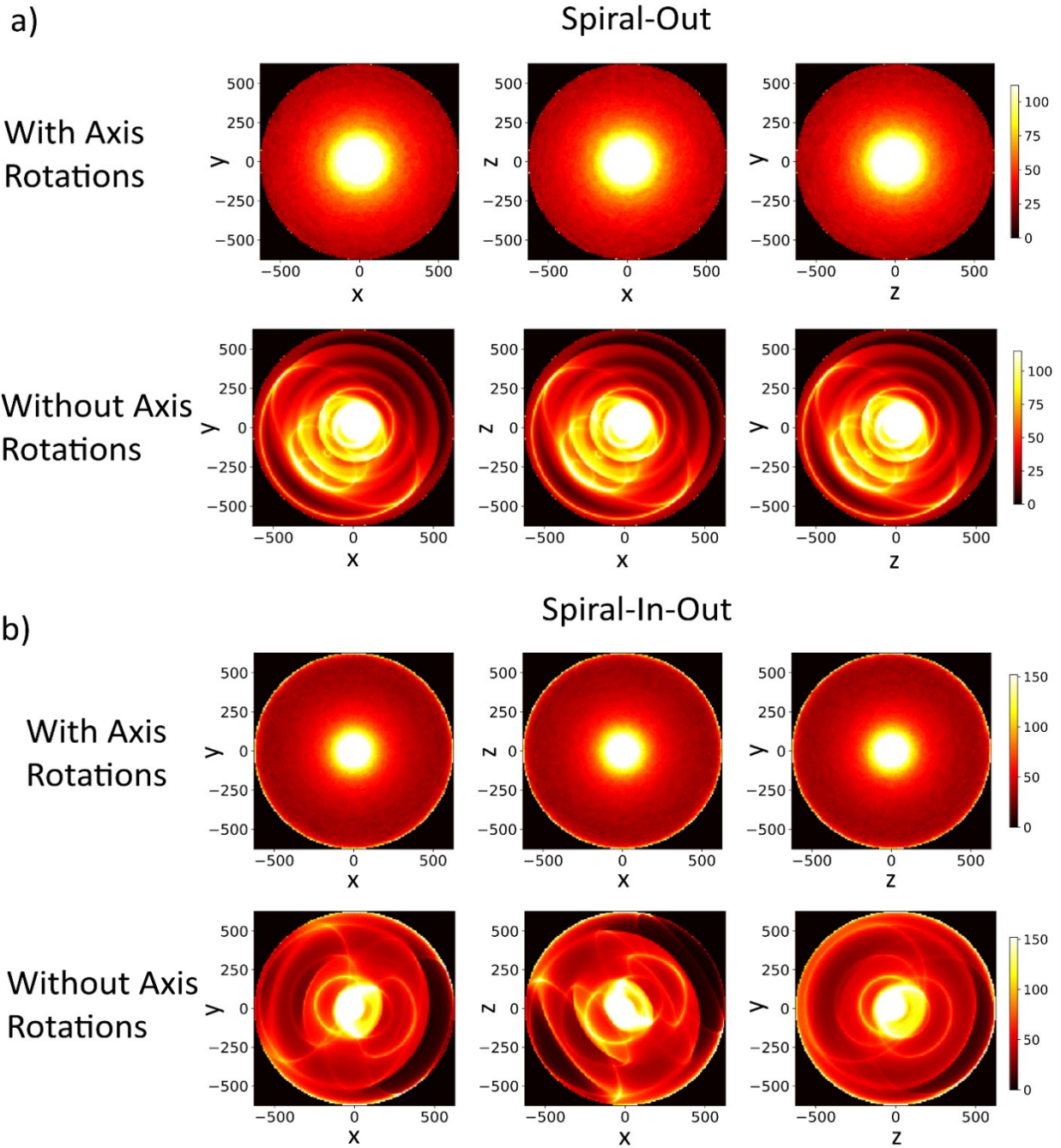


Figure 29: Sampling density plots representing number of points along each 2D column, normalized by the length of that column for a single echo trajectory with $\alpha = 1$. The top row is without axis rotations, and the bottom row is with random axis rotation, showing more uniformly spaced points. The spiral-in-out case also shows more densely sampled points at the periphery of the k-space sphere.

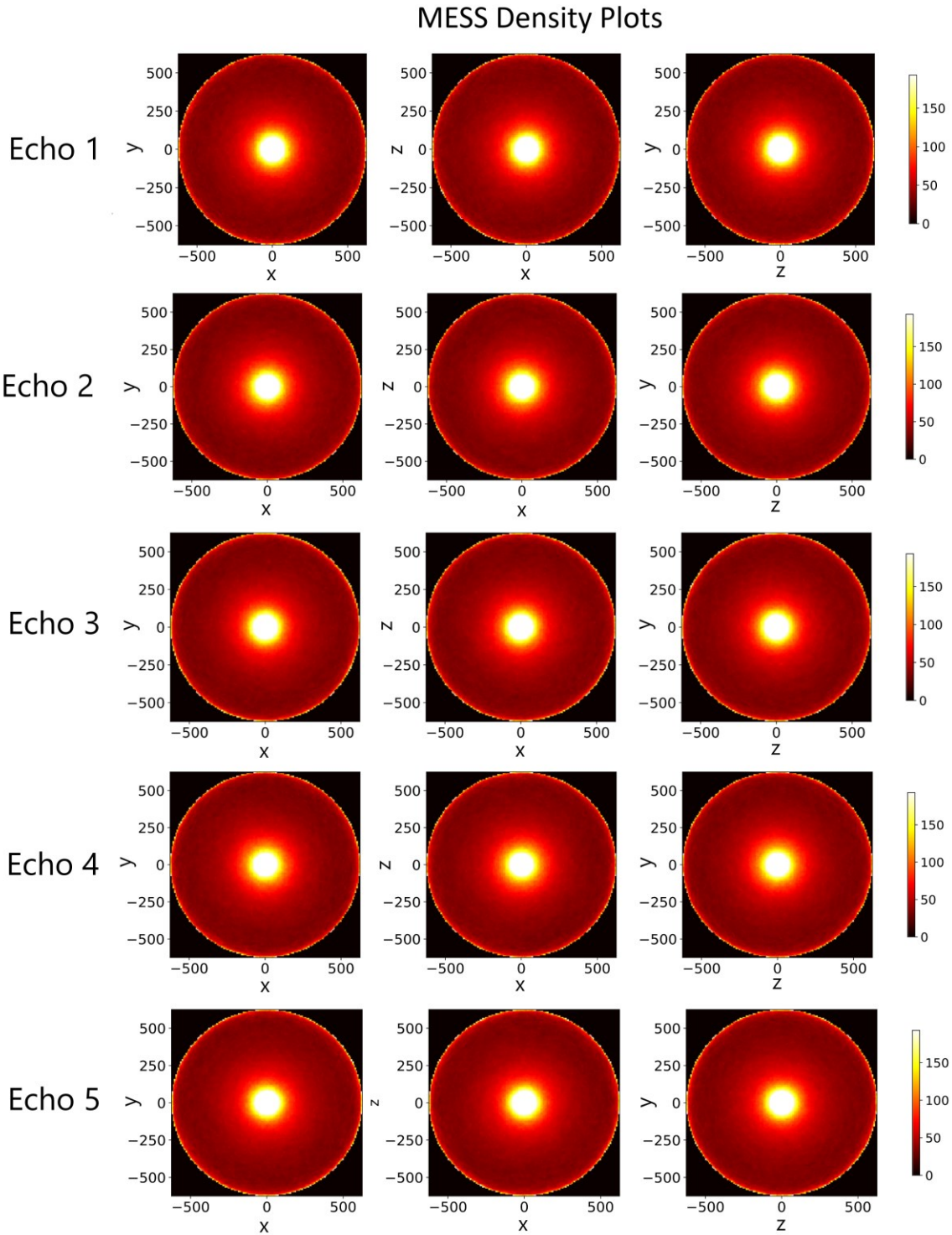


Figure 30: Sampling density plots representing number of points along each 2D column, normalized by the radius at that column for a single echo trajectory for the MESS case. This displays the consistent density profile along all echo samplings profiles.

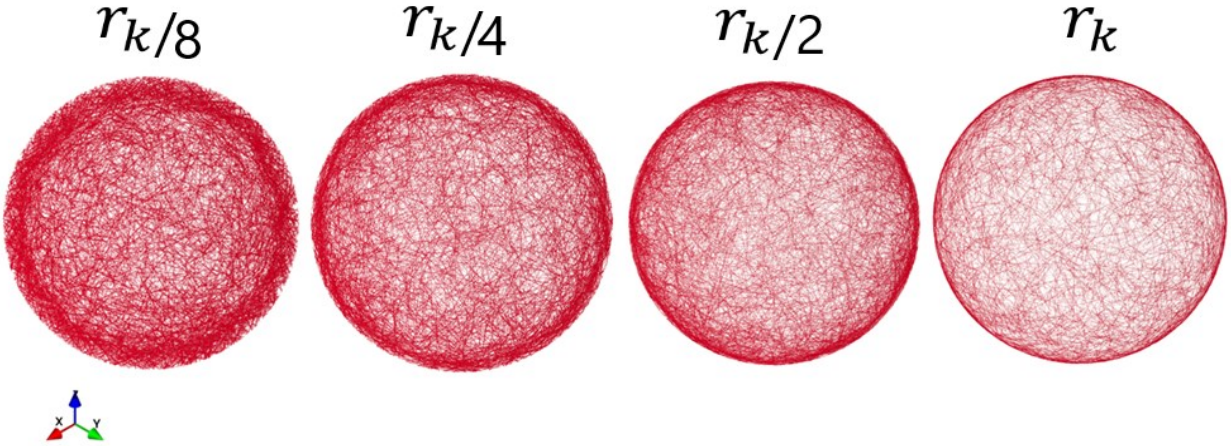


Figure 31: Density of points along different k -space radial shells with $\Delta K_{nyquist}$ thickness for the single echo spiral-out Seiffert spiral, displaying the uniform 3D distribution of points along each radial surface, and more dense sampling at smaller radii.

3.1.8 Nyquist Check

To ensure the Nyquist criteria $\Delta K_{nyquist} = \frac{1}{FOV}$ is met, a complete search of the k -space volume is performed. The sampling density is related to the number of Fibonacci rotations performed, thus an initial guess based on the 3D radial sampling case is calculated, then iteratively increased by evaluating the sampling within 3D Cartesian bins.

The number of radial shots required to sample a k -space sphere of radius r_k is calculated from the ratio of the area sampled by each point and the surface area of the sphere [101], given in (Equation 10).

The 3D Seiffert spiral trajectory acquires more k -space data points per repetition than a radial spoke due to its winding, thus fewer repetitions are needed to acquire all of k -space. To calculate the number of repetitions required, we first determine how many Nyquist spaced k -space points are acquired along a single trajectory within a spherical shell of $\Delta K_{nyquist}$ thickness. The Nyquist sampling criteria is checked at the radius with the lowest sampling density, which most often corresponds to the periphery of k -space. The number of shots is equal to the ratio of the number of points required to sample the sphere at radius r_k and the number points within the $\Delta K_{nyquist}$ rim centered at r_k for a single trajectory.

$$N_{shots}(r_k) = \frac{N_{radial}(r_k)}{N_{rim}(r_k)}$$

(Equation 20)

The k-space along the Seiffert spiral trajectory is often over-sampled. The points along the trajectory are thus reparametrized by the Nyquist distance to calculate $N_{rim}(r_k)$. For a multi-echo trajectory, there are two segments of the wind-in wind-out trajectory to be taken into account in this calculation. The initial guess for number of shots is the maximum across all radii r_k .

$$N_{guess} = \max\{N_{shots}(r_k) \mid 0 < r_k < k_{max}\}$$

(Equation 21)

To verify the Nyquist criterion is met, an iterative nearest neighbor check is implemented. This is performed by creating a 3D Cartesian grid at $\Delta k_{nyquist}$ distances between points and overlaying it with the 3D Seiffert spiral trajectory. The spiral's samples are grouped to a grid point within a Nyquist distance away. The grouping is performed using Scipy's KD-tree nearest neighbor algorithm. A spiral sample can belong to multiple grid points if it is within both of their Nyquist spheres. The passing criteria are 1) that no grid point be empty, and 2) that each grid point have a neighboring sample within the Nyquist distance away for all 6 immediately neighboring grid points. If these conditions are not met, the number of Fibonacci rotations is increased, and the grid check is repeated.

Eventually, a small portion of grid points will continue to fail and increasing the number of Fibonacci rotations will produce depreciating benefits. Thus, when the number of failing grid points is within 10% of the number of Fibonacci rotations, the gaps are filled by manually rotating a trajectory to pass through the gap. The missing grid point is determined to be the midpoint between two grid points whose closest trajectory samples are not within Nyquist distance of each other. The rotation is performed using the rotation vector v_m pointing to the trajectory sample with the nearest k-space radius to the location of the gap. The single rotation matrix R_{manual} takes v_m to the vector pointing from the origin to the gap location v_{gap} .

$$R_{manual}v_m = v_{gap}$$

(Equation 22)

The final total number of shots is equal to.

$$N_{shots} = N_{Fib} + N_{manual}$$

(Equation 23)

3.2 Image reconstruction

Two image reconstruction pipelines were used to reconstruct images from non-uniform k-space acquisitions. All PSFs were reconstructed using the MRI Berkeley Advanced Reconstruction Toolbox (BART) [95]. The BART *NUFFT* function allows for NC image reconstruction using the Conjugate Gradient algorithm with L2 error regularization. All digital phantom and real acquisitions were reconstructed using the Partial Dual Hybrid Gradient (PDHG) algorithm with L1-wavlet regularization from the Sigpy python package as outlined by Ong et al [102].

3.3 Imaging Experiments

To determine the impact of a specific sampling trajectory on image quality, a PSF can be used to assess resolution, and artifacts in the image domain's FOV. A PSF is the image created of a point source, akin to an impulse response function. A point source is characterized by spatial frequencies being equally present in all directions, therefore it will have a value of 1 everywhere in the k-space domain. The data along the readout trajectory can be modulated by the T2* signal decay to visualize the impact of T2* decay on the PSF, also known as T2* blurring. The k-space data and the trajectory coordinates are taken to the spatial domain using NUFFT, resulting in the PSF.

An ideal PSF should have a sharp spike at the center of the spatial domain, and zero for all other values inside the FOV sphere. In reality, a width is associated with the peak corresponding to the true resolution of the image, and smaller side lobes exist within the FOV representing artifacts. The broadening of the PSF's peak can be quantified using the full-width-half-max (FWHM) of the global maximum.

MRI acquisitions were performed using a T2*-weighted GRE sequence on the Siemens Terra 7T scanner using the 1/32-channel transmit/receive Nova head coil at the Montreal Neurological

Institute (a.k.a., The Neuro). The study was approved by McGill University’s institutional ethics committee.

3.3.1 Single-Echo Seiffert Spiral

Single echo Seiffert spiral images were assessed for image resolution and the presence of undersampling artifacts using simulated PSF and 3D digital phantom acquisitions.

Undersampling factors of $R = 1, 2,$ and 6 were tested for the appearance of artifacts and the impact on resolution using a constant (i.e., not $T2^*$ -modulated) single-echo trajectory of 0.8mm resolution, 240 mm FOV, and an α of 1 .

The same trajectory specifications were implemented to acquire *in vivo* healthy human brain images. Images were acquired with a fully and $R=2$ sampled Seiffert spiral trajectory. An equivalent protocol with a Cartesian line-by-line readout was acquired with the same acquisition parameters. All three acquisitions were performed i) using their minimum TE and TR to shorten scan time, and ii) with matching TE and TR values between all trajectories.

Table 1: Acquisition parameters for the single echo $T2^*$ -weighted human brain imaging protocols.

	Matching			Optimized		
	Seiffert Spiral		Cartesian	Seiffert Spiral		Cartesian
R	1	2	1	1	2	1
TR (ms)	12	12	12	10.15	10.15	6.2
TE (ms)	2.79	2.79	2.79	1.48	1.48	2.79
Readout Time (ms)	6	6	3.84	6	6	3.84
Resolution (mm)	0.8	0.8	0.8	0.8	0.8	0.8
FOV (mm)	240	240	240	240	240	240
α	1	1	n/a	1	1	n/a
Flip angle	10	10	10	10	10	10
Matrix Size	300 x 300 x 300	300 x 300 x 300	600 x 300 x 240	300 x 300 x 300	300 x 300 x 300	600 x 300 x 240
Num shots	55 904	25 285	72 000	55 904	25 285	72 000
Scan time	11min 11s	5min 4s	14min 26s	9min 28s	4min 17s	7min 28s

3.3.2 Spiral-Out vs Spiral-In-Out Trajectory Design

The MESS trajectory winds-in from the periphery of k-space to the centre and back to the periphery. The image reconstructed from all echoes is evaluated using PSF analysis, digital phantom simulations, and real phantom images with the acquisition parameters below.

Table 2: Scan parameters for comparisons between spiral-out and spiral-in-out trajectory shapes.

Shape	Spiral-Out	Spiral-In-Out
Num Echos	1	
R	1	
Resolution (mm)	1.5	
FOV (mm)	240	
Flip angle	10	
Matrix Size	160 x 160 x 160	
Readout Time (ms)	1	
TR (ms)	6	
TE (ms)	2	2.5
Num shots	54 786	56 644
Scan time	5min 29s	5min 40s

3.3.3 MESS Optimized for Quantitative T2* Mapping

Sampling the T2* decay curve for T2* mapping requires longer readout durations of 20ms to 40ms for 4 to 7 echoes at 7T [13]. A 5-echo MESS acquisition protocol is analyzed through PSF analyses, digital phantom simulations, and T2* blurring phantom simulations. A physical phantom was scanned at 7T using a 6-times undersampled protocol to shorten scan time.

Table 3: Scan parameters for MESS trajectory for quantitative imaging

Num Echos	5
R	6
Resolution (mm)	0.8

FOV (mm)	240
Flip angle	10
Matrix Size	300 x 300 x 300
α	2
Readout Time (ms)	20 (4 each)
TR (ms)	25
TE (ms)	4, 6, 8, 10, 12
Num shots	2 178
Scan time	56s

3.3.4 Effects of Variable Sampling Density

The sampling density of the trajectory as a function of the radius can affect the number of shots, image SNR, resolution, and T2* blurring. The impact of sampling density is assessed for a 3-echo MESS protocol using PSF analysis, and phantom simulations of α 's of 0.1, 0.5, 1, and 2. Real 7T phantom acquisitions were only performed at three different α 's of 0.5, 1, and 2. The trajectory parameters are summarized in the table below.

Table 4: Image acquisition parameters for a 3-echo MESS protocols for three different α values: 0.1, 0.5, 1, and 2.

α	0.1	0.5	1	2
Num Echos	3			
R	1			
Resolution (mm)	2			
TR (ms)	-	11		
TE (ms)	-	3, 5, 7		
Readout Time (ms)	-	6 (2 each)		
FOV (mm)	-	240		
Flip angle	-	10		
Matrix Size	120 x 120 x 120			
Num shots	23 629	12 827	13 828	15 444
Scan time	-	2min 22s	2min 33s	2min 50s

4 Results

4.1 Single Echo Seiffert Spiral

The PSF in Figure 32 below is for a single echo Seiffert spiral trajectory that is fully, half, and 6 times undersampled. T_2^* decay during the readout was not included. The zoomed-in cross sectional view in Figure 33 shows broadening from the nominal isotropic resolution of 0.8mm to ~ 1.28 mm for the fully sampled case, with no apparent resolution broadening in the half-sampled case. The PSFs for all sampling cases show a PSF broader than the expected 0.8mm resolution. This is to be expected for a 3D spiral trajectory design, as the Yarnball also experienced a 1.69 times broader PSF than the target resolution [1]. Single echo images were acquired for $\alpha = 1$, which contains very non-uniform k-space sampling as demonstrated in Figure 21.

Surprisingly, the $R = 2$ factor did not result in a significant decrease in resolution compared to $R=1$. However, as can be seen in Figure 32, there is more high frequency noise inside the FOV for the $R=2$ case than the fully sampled case, corresponding to undersampling artifacts. The $R=6$ undersampling of the trajectory resulted in a very slight broadening of the PSF peak by ~ 0.14 mm compared to the $R=1$ and $R=2$ case (Figure 33), along with significant undersampling artifacts in the form of noise in the PSF (Figure 32), unlike coherent circular artifacts present in undersampled cones and spirals (Figure 14). The incoherent undersampling artifacts are less detrimental to image interpretation, and more compatible with compressed sensing and parallel imaging techniques.

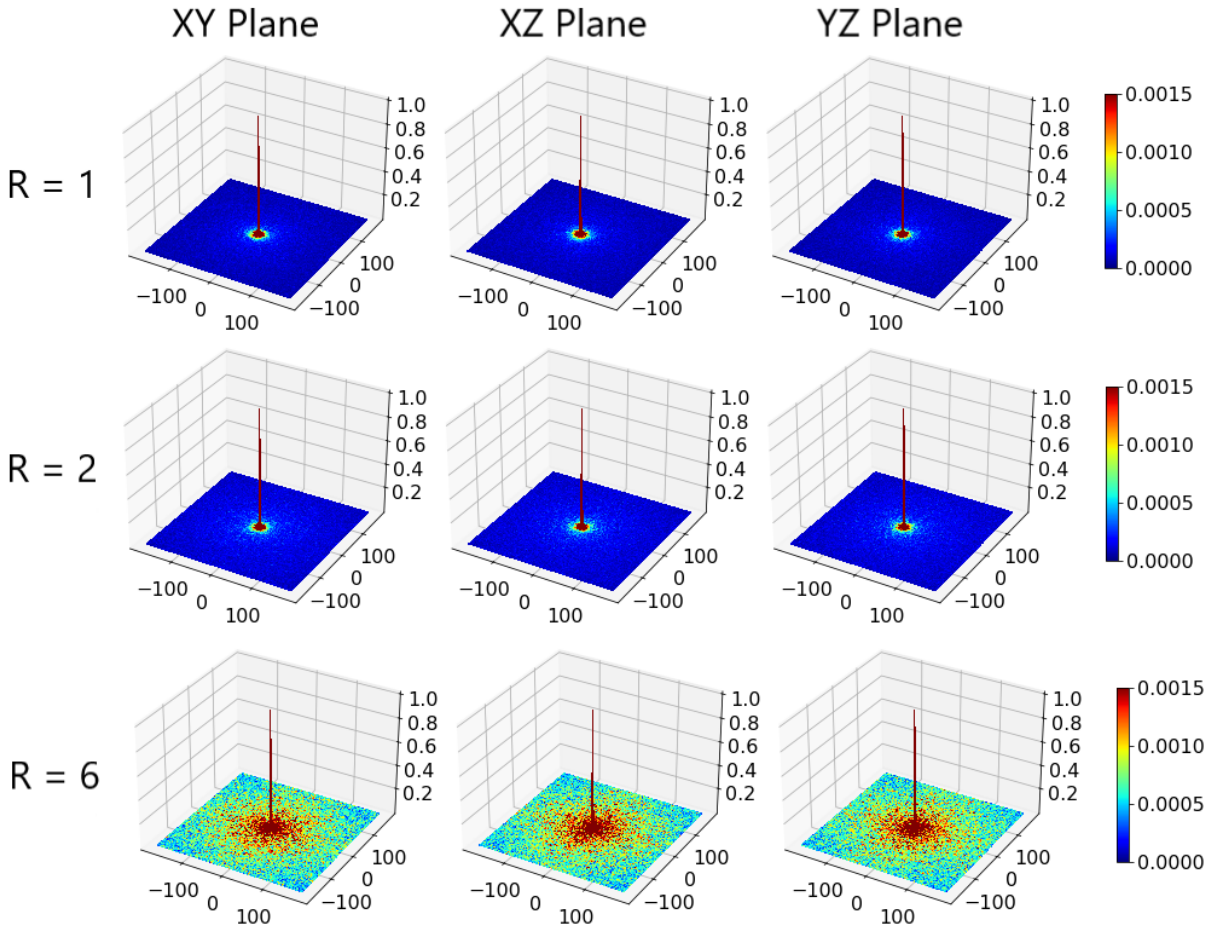


Figure 32: PSF for $R = 1$ (top), $R = 2$ (middle), $R = 6$ (bottom) acceleration factors of the same single echo Seiffert spiral trajectory with 240 FOV, 0.8mm resolution, and an α of 1.

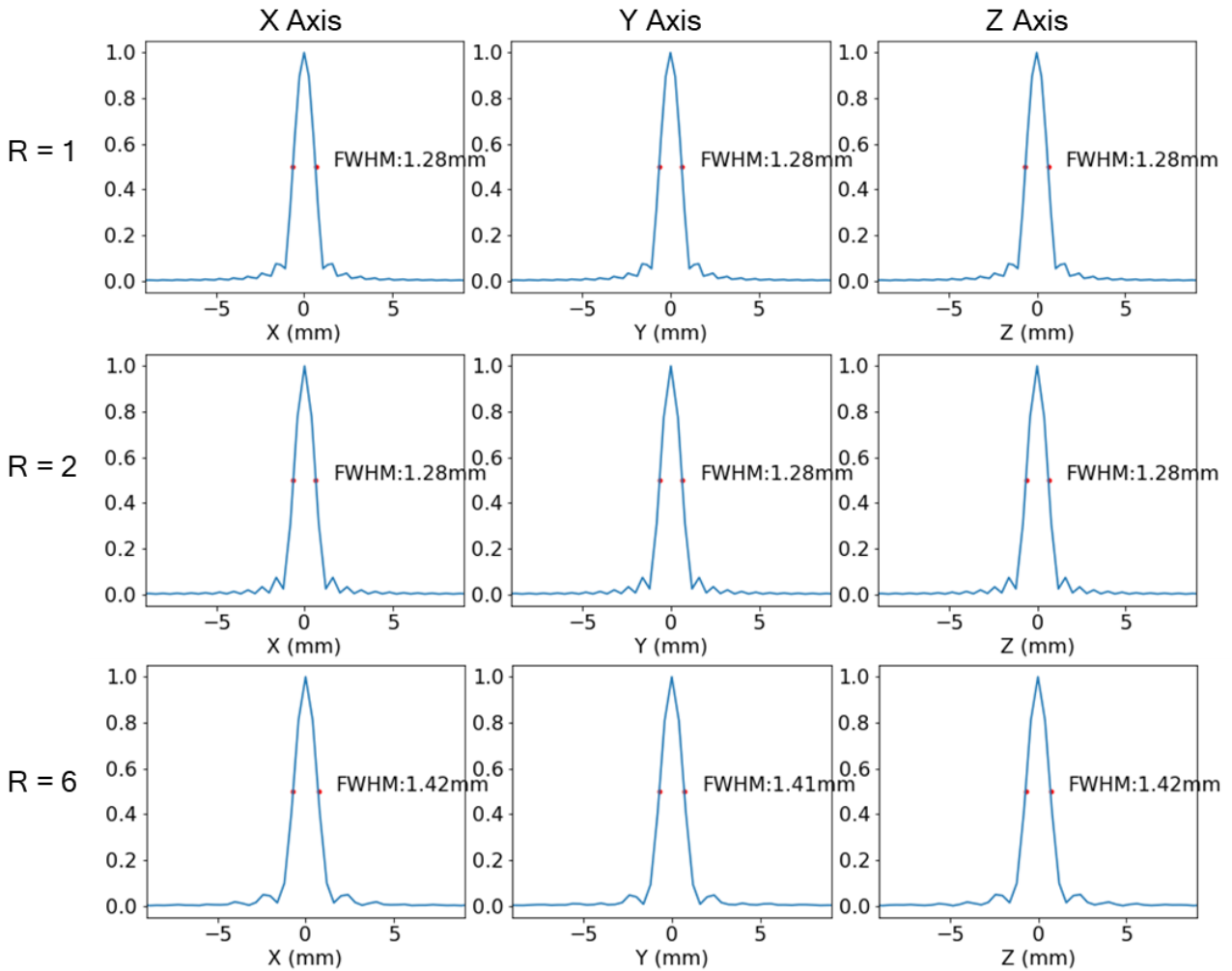


Figure 33: cross-section of PSF in x, y, and z directions for fully, half, and 6 times undersampled single echo Seiffert spiral with a nominal resolution of 0.8mm, along with the FWHM resolution displayed on the graphs. All image reconstruction was performed using the default NUFFT transform.

The reconstructed digital phantom images below demonstrate the impact of the k-space trajectory-related image reconstruction artifacts and resolution. Digital phantom images were created for each of the formerly mentioned trajectory specifications.

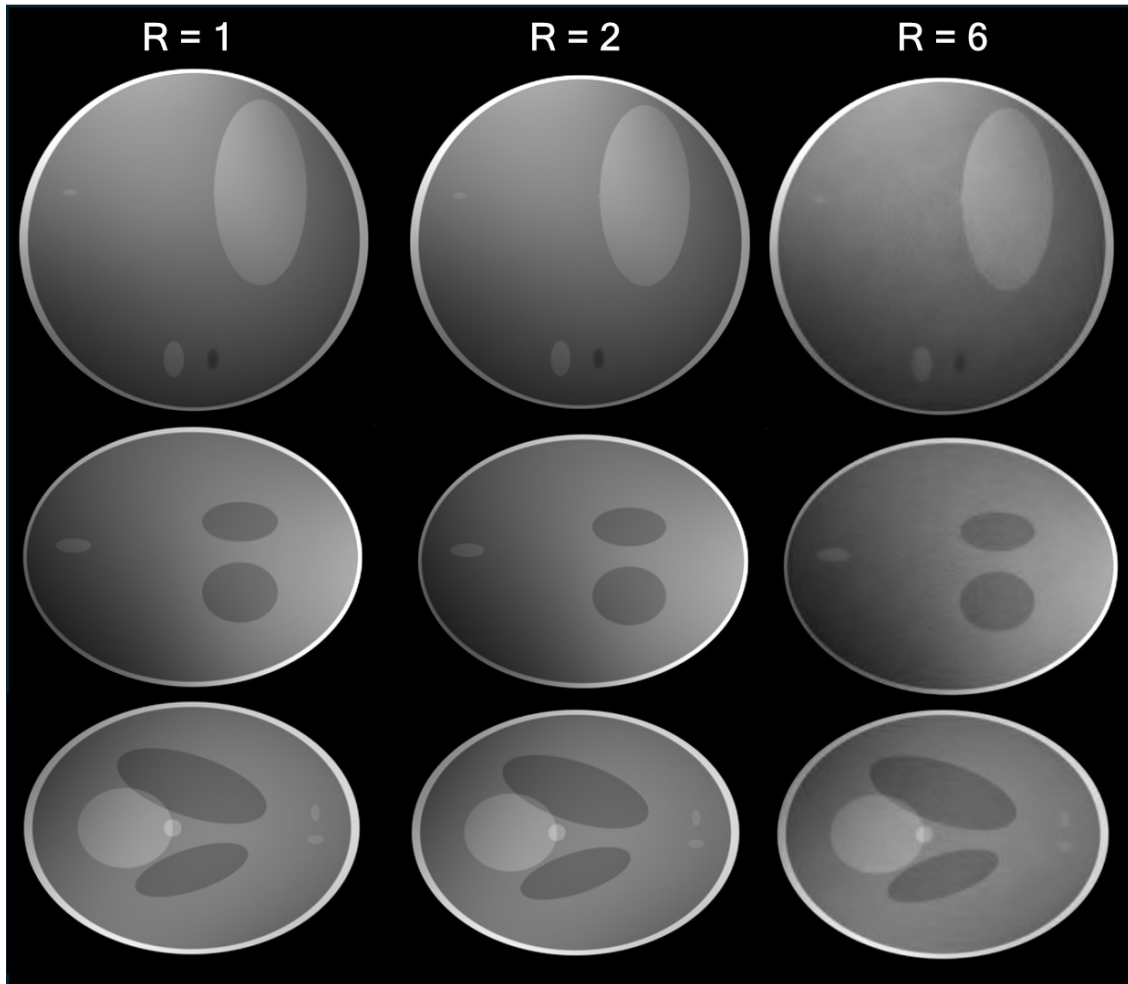


Figure 34: Digital phantom image for a single echo Sieffert spiral trajectory with $R = 1$ (left), $R = 2$ (middle), $R = 6$ (right) undersampling factors, and a constant 0.8mm resolution, 6ms readout, and an $\alpha = 1$.

The simulated phantom images in Figure 34 reconstructed using the PDHG parallel imaging algorithm with 8 coil sensitivity profiles show that the fully and half sampled trajectories better capture the phantom's structure, however the $R=6$ case has some noise-like artifacts throughout the image, which is consistent with the PSF in Figure 32. The artifacts are enhanced for higher acceleration factors, as expected since 8 coils were used to recover 6 times undersampled data.

Human brain images at $R=1$ and $R=2$ acquired using the protocols in Table 1 are shown in Figure 36.

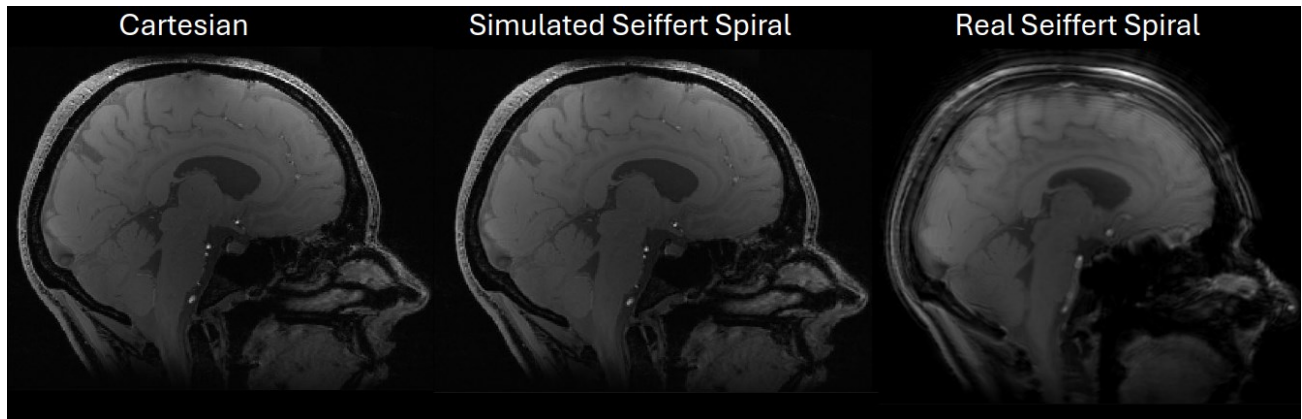


Figure 35: Comparison of a 0.8mm, 240mm FOV MRI image acquired along a single echo Cartesian (left), and Seiffert spiral (right) trajectory. The Cartesian image is also used as a phantom to simulate the Seiffert spiral sampling and reconstruction of the same trajectory parameters under ideal conditions (middle).

The human brain images showed that the Seiffert spiral is capable of producing high resolution 3D images albeit with some additional blurring and significant ringing near the skull compared to the Cartesian case in Figure 35 and Figure 36. The acquired Cartesian and Seiffert spiral images are compared with a simulated acquisition which samples the Cartesian image in Figure 35 along the same Seiffert spiral trajectory used for the real MRI data acquisition. Since the same trajectory was used to create the simulated and real images, comparisons between the two show the Seiffert spiral trajectory and reconstruction pipeline can generate images of equivalent quality to Cartesian sampling. The presence of additional artifacts in the real image in Figure 35 might be due to additional sources of MRI scan error such as T2* blurring, main magnetic field imperfections, gradient field deviations, for instance. Since the ringing is not present in the digital phantom simulation in Figure 34, the cause could be due to B_0 inhomogeneities, trajectory deviations, or improper NUFFT parameters leading to improper image reconstruction with the PDHG algorithm. The half sampled brain image in Figure 35 introduced slight blurring artifacts compared to the R=1 case, suggesting undersampling artifacts of the single echo Seiffert spiral manifest as increased blurriness in real imaging experiments. This is consistent with the increased blurring accompanying the 8 times undersampled Seiffert spiral data observed by Speidel et al (Figure 12) [11].

The fully sampled Seiffert spiral protocol was 1.3 times faster than Cartesian imaging, reducing the scan time from 14min 26s to 11min 11s for the matching TE and TR case. A simulated

Cartesian half-sampled acquisition in the phase direction with the same parameters as the fully sampled matching TE and TR sequence would require a 7min 14s scan time, which compared to the half-sampled Seiffert spiral requiring 5min 4s, resulting in a 1.4 times faster acquisition time for the R = 2 Seiffert spiral.

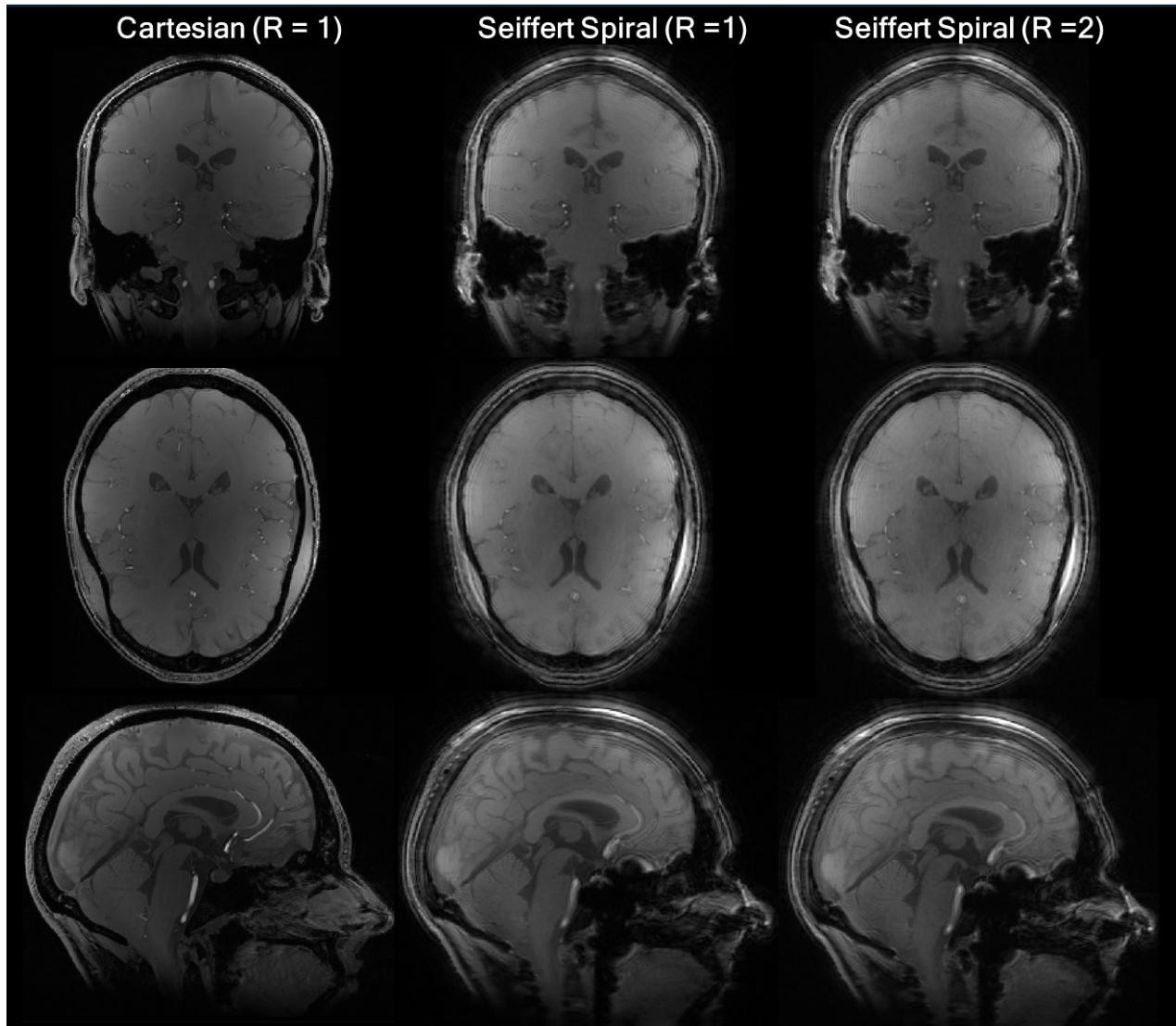


Figure 36: Human brain T2 weighted single echo Seiffert spiral images acquired at 240 FOV, 0.8mm resolution, 6ms readout, $\alpha = 1$, fully (left) and half sampled (middle). Reconstruction was performed using 32 coils with root sum of squares averaged. The reconstruction was also performed using PICS on the half-sampled image (right).*

4.2 Spiral-Out vs Spiral-In-Out Trajectory Design

The multi-echo case requires a different sampling trajectory design than the single-echo Seiffert spiral, acquiring points along a spiral-in-out pattern, instead of a spiral-out trajectory. This results in a different sampling density, as seen in Figure 21, where the spiral-in-out case has a higher sampling density near the periphery of k-space due to the slower winding to create smooth gradient waveforms.

The FWHM results in Table 5 show slight PSF peak broadening from the target resolution for both trajectory designs, with no additional peak broadening when winding in the spiral-in-out case, with slightly less FWHM broadening when T2* modulation is included. The FWHM analyses in Table 5 also show that T2* blurring is minimal for this short readout duration of 1ms.

Table 5: Table summarizing the PSF's FWHM of the spiral-out and spiral-in-out trajectory designs of nominal resolution 1.5mm and a short readout of 1ms.

Units: (mm)	Spiral-Out		Spiral-In-Out	
	Without T2* blurring	With T2* blurring	Without T2* blurring	With T2* blurring
x	2.37	2.38	2.37	2.37
y	2.37	2.38	2.37	2.37
z	2.37	2.38	2.36	2.36

Further comparisons are performed for a 6ms readout with all other specifications remaining the same. The change in readout duration from 1ms to 6ms showed a slight sharpening of the PSF peak by ~0.01mm (Table 5 and Table 6). This small change could be due to slightly improved peripheral coverage of the longer spiral trajectory, since a very short readout is akin to a radial sampling trajectory. The 6ms spiral-out case with T2* blurring showed 0.01mm broader FWHM resolution to the 1ms readout in Table 5, demonstrating that the longer readout spiral-out trajectory is more sensitive to T2* blurring. However, the spiral-in-out trajectory for both readout times did not exhibit significant T2* blurring compared to the no T2* modulation case.

The PSFs in Figure 37a show that T2* modulation has little effect on the spiral-out case with very few additional artifacts seen outside the main peak of the PSF. Conversely, Figure 37b shows the spiral-in-out case contains more speckled artifacts inside the FOV when T2* modulation was accounted for. This is expected due to points at the same radial distance being sampled at different time points of the T2* decay curve. The additional artifacts are more dramatic than for the spiral-out case, suggesting additional loss in image quality due to T2* blurring for the spiral-in-out design than the spiral-out case. However, the FWHM analysis in Table 6 shows more peak broadening for the spiral-out case than the spiral-in-out case for T2* modulation. This suggests that while introducing more image artifacts into the spiral-in-out case, T2* modulation degrades the resolution of the spiral-out by ~0.01mm FWHM broadening.

Table 6: Table summarizing the PSF's FWHM of the spiral-out and spiral-in-out trajectory designs of target resolution 1.5mm and a longer readout time of 6ms, comparing with and without T2 blurring for grey matter with a T2* value of 33.2ms.*

Units: (mm)	Spiral-Out		Spiral-In-Out	
	Without T2* blurring	With T2* blurring	Without T2* blurring	With T2* blurring
x	2.36	2.39	2.36	2.36
y	2.36	2.39	2.36	2.36
z	2.36	2.39	2.36	2.36

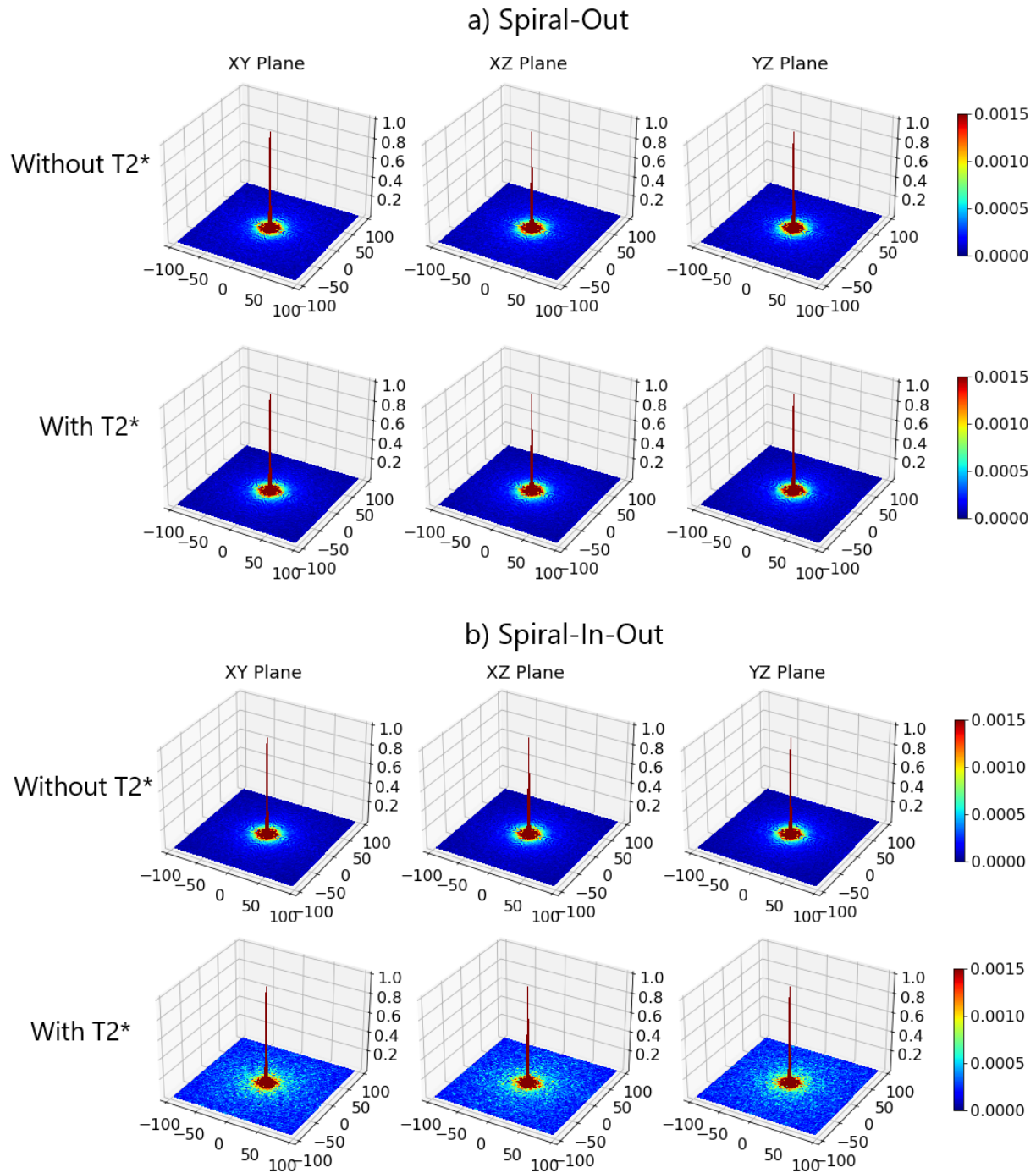


Figure 37: PSF for a single echo 1.5mm resolution 6ms readout with and without T_2^* blurring for a) the spiral-out and b) spiral-in-out trajectory design case. Comparisons show more artifacts due to T_2^* blurring for the spiral-in-out trajectory case.

Digital phantom images with the same trajectory parameters, including the same readout time of 1ms and α of 0.5, show how the trajectory design affects image quality without the effect of T_2^* blurring. The spiral-in-out phantom image in Figure 38 produces nearly identical image quality to the spiral-out sampling scheme despite differences in k-space sampling density. The only notable difference is the spiral-in-out trajectory's image displays slightly more ringing artifacts in some locations in the image shown by the red arrows in Figure 38. This suggests that the default PDHG's reconstruction parameters can be optimized further for the reconstruction of spiral-out and spiral-in-out Seiffert spiral designs.

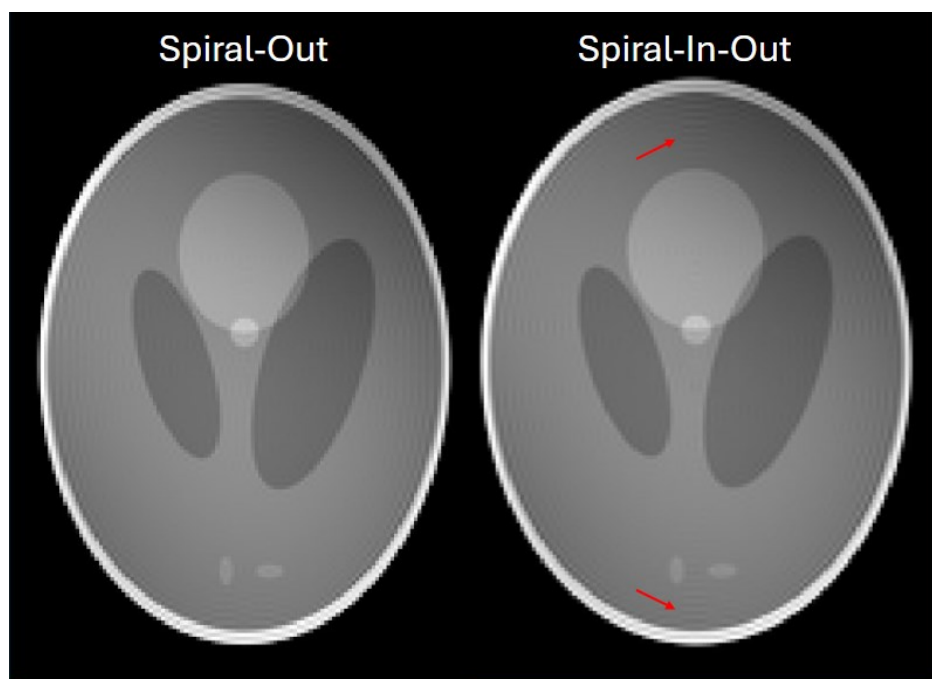


Figure 38: Digital phantom images of a single echo spiral-out (left) and spiral-in-out (right) trajectory designs with parameters described in Table 2, including a 240 FOV, 1.5mm resolution, 1ms readout, and an α of 0.5. Red arrows show locations of significant ringing artifacts.

The real phantom scans of the spiral-out and spiral-in-out trajectories acquired at 7T shows slightly different image quality from each other (Figure 39), different from the nearly identical digital phantom images presented above (Figure 38). The spiral-out trajectory image in Figure 39 has a higher SNR but also great signal non-uniformity and blurring. This could be due to the non-uniform k-space sampling density which requires density compensation during reconstruction. 100 iterations of the PDHG's reconstruction were performed to address this issue, but further optimization of the reconstruction parameters is necessary.

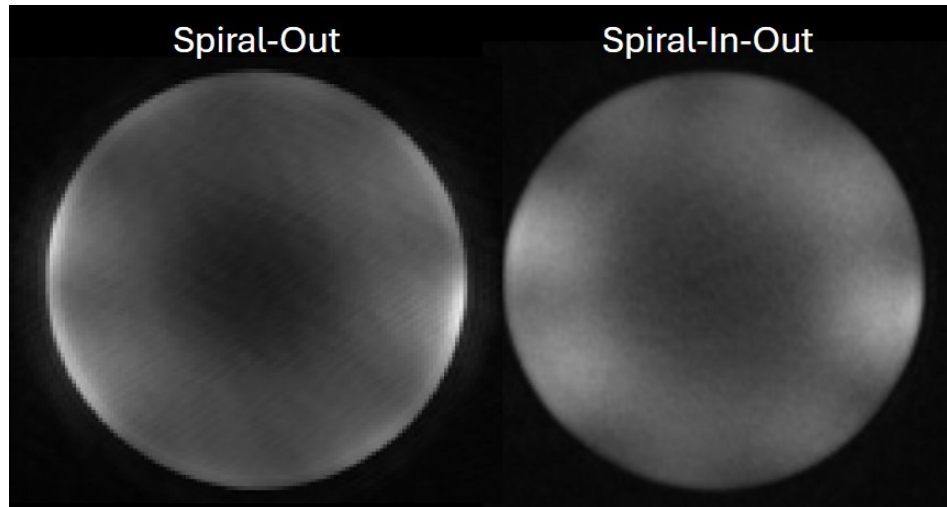


Figure 39: Single echo Seiffert spiral acquisition of a phantom with scan parameters described in Table 2, including 240 FOV, 1.5mm resolution, 1ms readout, α of 0.5, $R = 1$, in a spiral-out shape (left) and spiral-in-out shape (right).

4.3 MESS Optimized for T2* Mapping

A MESS acquisition of 5 echoes with a 20ms total readout time (4ms readout per echo) and 6 times undersampling was simulated to assess image quality between echoes in Figure 40. The PSF analysis with no T2*blurring in Table 7 demonstrated the FWHM of all the echoes are in agreement. This consistency between the echoes' PSF peaks shows the trajectory consistently meets sampling requirements for all echoes. The FWHM broadening from 0.8mm to 1.45mm is comparable to the single echo case with the same undersampling factor causing broadening to 1.42mm. This shows the $R = 6$ MESS shows an ~ 1.8 times broader PSF FWHM than the target resolution. Digital phantom images in Figure 40 show similar image quality for all echoes. This shows Nyquist checks applied to the first echo can be extrapolated to subsequent echoes with minimal artifacts.

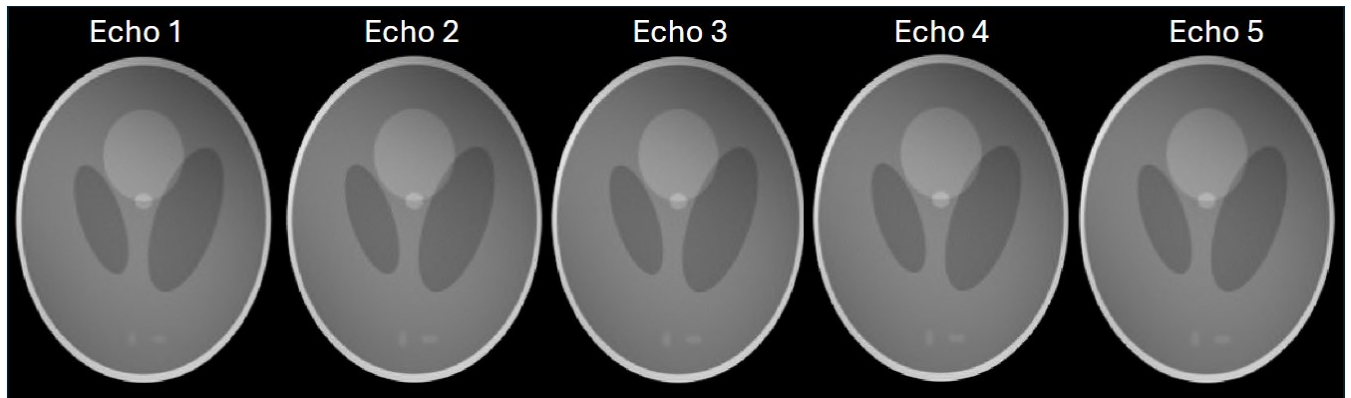


Figure 40: 6 times undersampled multi-echo digital phantom simulated sampling with the MESS trajectory as described in Table 3.

Table 7: FWHM with no T2* blurring for a 0.8mm resolution, 6 times undersampled, 20ms readout (5ms each echo), 5 echoes MESS trajectory as described the parameters in Table 3.

Units: (mm)	x	y	z
Echo 1	1.44	1.45	1.45
Echo 2	1.44	1.45	1.44
Echo 3	1.44	1.45	1.44
Echo 4	1.44	1.45	1.44
Echo 5	1.44	1.45	1.44

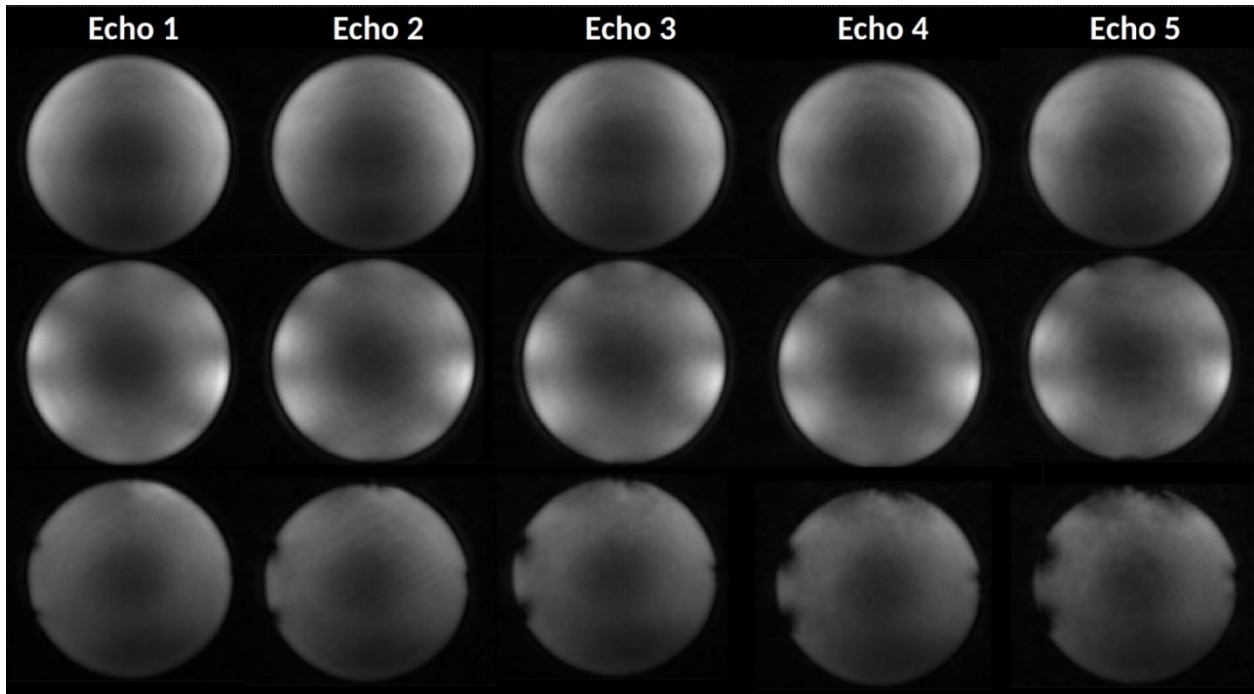


Figure 41: 5 echo 6 times undersampled MESS acquisition of a phantom at 0.8mm resolution, 240 FOV, 20ms readout (4ms per echo), and α of 2. All 5 echoes are shown along with 3 different views of the phantom.

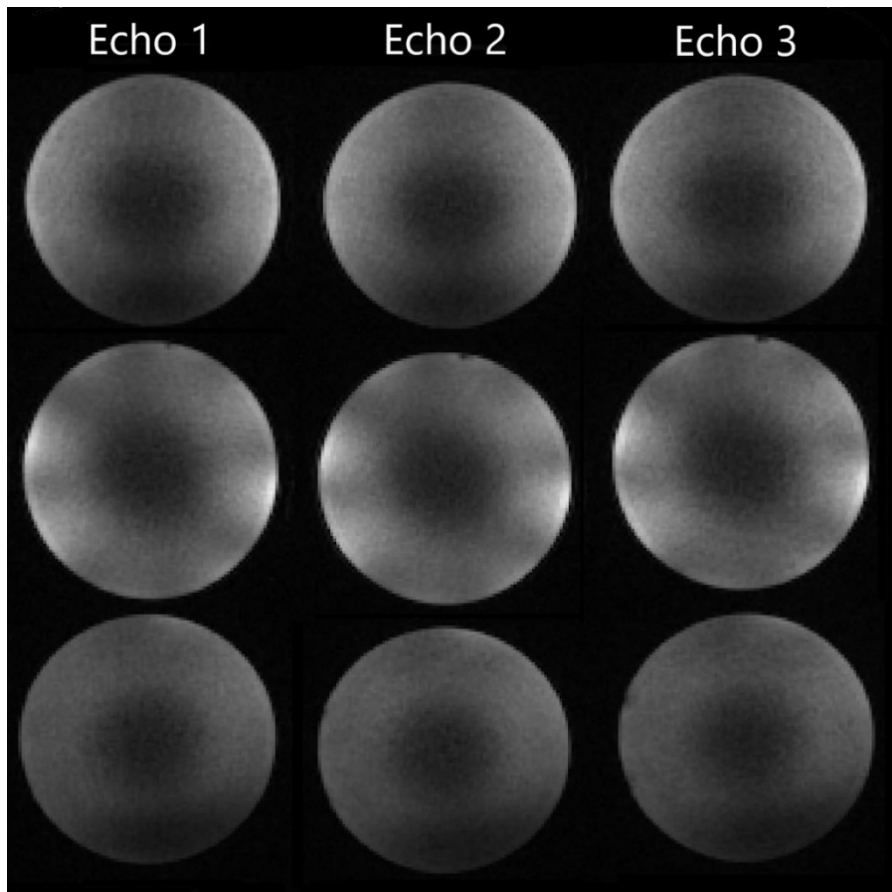


Figure 42: 3 echo MESS acquisition at 204 FOV, 2mm resolution, 6ms readout (2ms per echo), α of 1, $R = 1$. All 3 echoes are shown along with 3 different views of the echoes.

A 3 echo MESS for $\alpha = 1$ described in Table 4 shows consistency in image quality in real phantom images at different echo times in Figure 42. However, scan time reductions are greatest for longer readout durations, therefore the 5 echo MESS acquisition with a 20ms readout duration (4ms per echo) was designed to show trajectory design flexibility and respect of peripheral nerve stimulation limitations at a longer readout time.

Moderate signal drop off is shown in Figure 42 for the 3 echo case, especially in the bottom and middle row view of the phantom due to $B1^+$ field inhomogeneity. More severe signal drop off is shown in Figure 41, particularly at later echoes due to longer readout times of 20ms compared to the 6ms for the 3 echo case in Figure 42. Multi-echo images in Figure 42 at shorter readout time (2ms vs 4ms) show less blurring due to $T2^*$ and off-resonance effects compared to the longer readout in Figure 41.

The longer readout times are associated with more scan time efficiency compared to Cartesian sampling. A 4.2 times speed up is observed from a 56 seconds scan time with $R = 6$, 5 echo 20ms MESS readout versus 3min 58s for the Cartesian equivalent with matching TE and TR. A similar scan time was observed for a 2min 22s acquisition of a fully sampled 3 echo 6ms readout versus the 2min 23s Cartesian equivalent with matching TE and TR.

4.4 Effects of non-uniform radial sampling density

One key difference between the 3D Seiffert spiral trajectory and one which samples along a Cartesian grid, is that the Cartesian samples are evenly spaced enabling image reconstruction using the fast Fourier transform. The sampling density of the 3D Seiffert spiral varies as a function of the radius, requiring additional density compensation in the NUFFT reconstruction. The α parameter controls the sampling density near the center of k-space. As shown in Figure 21 and Figure 22, a higher α of 1 and 2 results in a higher sampling density near the center of k-space, while a lower α of 0.5 is more uniform. Oversampling the center of k-space will improve the SNR of the image, but overrepresentation of low frequencies can cause image artifacts. Additionally, undersampling the periphery of k-space can impact image resolution. Decreasing

the α to an even lower value of 0.1 leads to more time being spent at the higher radial values, which can be seen in Figure 20ea, and since each shot starts at the center of k-space, the central volume is still oversampled. This leads to the center and periphery dense sampling profile in Figure 21 and Figure 22 for an α of 0.1, which is less uniform in k-space than the $\alpha = 0.5$ case.

Estimating the density compensation function in NUFFT is an expected obstacle in non-Cartesian sampling. If the variable density is not considered, the image may contain artifacts. The PSF analysis for α 's of 0.1, 0.5, 1, and 2 reveals a slight decrease in FWHM for increasing α values as seen in Table 8, with a $\sim 0.01\text{mm}$ broadening from a α of 0.1 to 2. The FWHM was not affected by the jump from and α of 0.1 to 0.5 but did show $\sim 0.01\text{mm}$ increase in the later echoes with the α increase from 0.1 to 1. The lower α values contain slightly higher resolution PSFs due to more sampling on the periphery of k-space, however this change should not be significant since the Nyquist test accounts for that by increasing the number of shots until the Nyquist distance criterion is met.

Table 8: Table summarizing the FWHM in x, y, and z for various α s of 0.5, 1, and 2 with a 3 echo MESS trajectory at 240 FOV, 2mm resolution, $R = 1$.

Units: (mm)	$\alpha = 0.1$			$\alpha = 0.5$			$\alpha = 1$			$\alpha = 2$		
	x	y	z	x	y	z	x	y	z	x	y	z
Echo 1	3.14	3.14	3.14	3.14	3.14	3.14	3.14	3.14	3.14	3.15	3.15	3.15
Echo 2	3.13	3.13	3.13	3.13	3.13	3.13	3.14	3.14	3.14	3.14	3.14	3.14
Echo 3	3.13	3.13	3.13	3.13	3.13	3.13	3.14	3.14	3.14	3.14	3.14	3.14

The PSFs in Figure 43 show slightly more speckled noise-like artifacts for $\alpha = 0.1$ than for $\alpha = 0.5$, which outperforms all other α values for the presence of artifacts in the FOV. This could be due to the more uniform sampling density throughout the k-space volume. The NUFFT operator used to reconstruct the PSFs could introduce artifacts into the image domain data due to overrepresentation of low or high frequency signals, depending on the trajectory design.

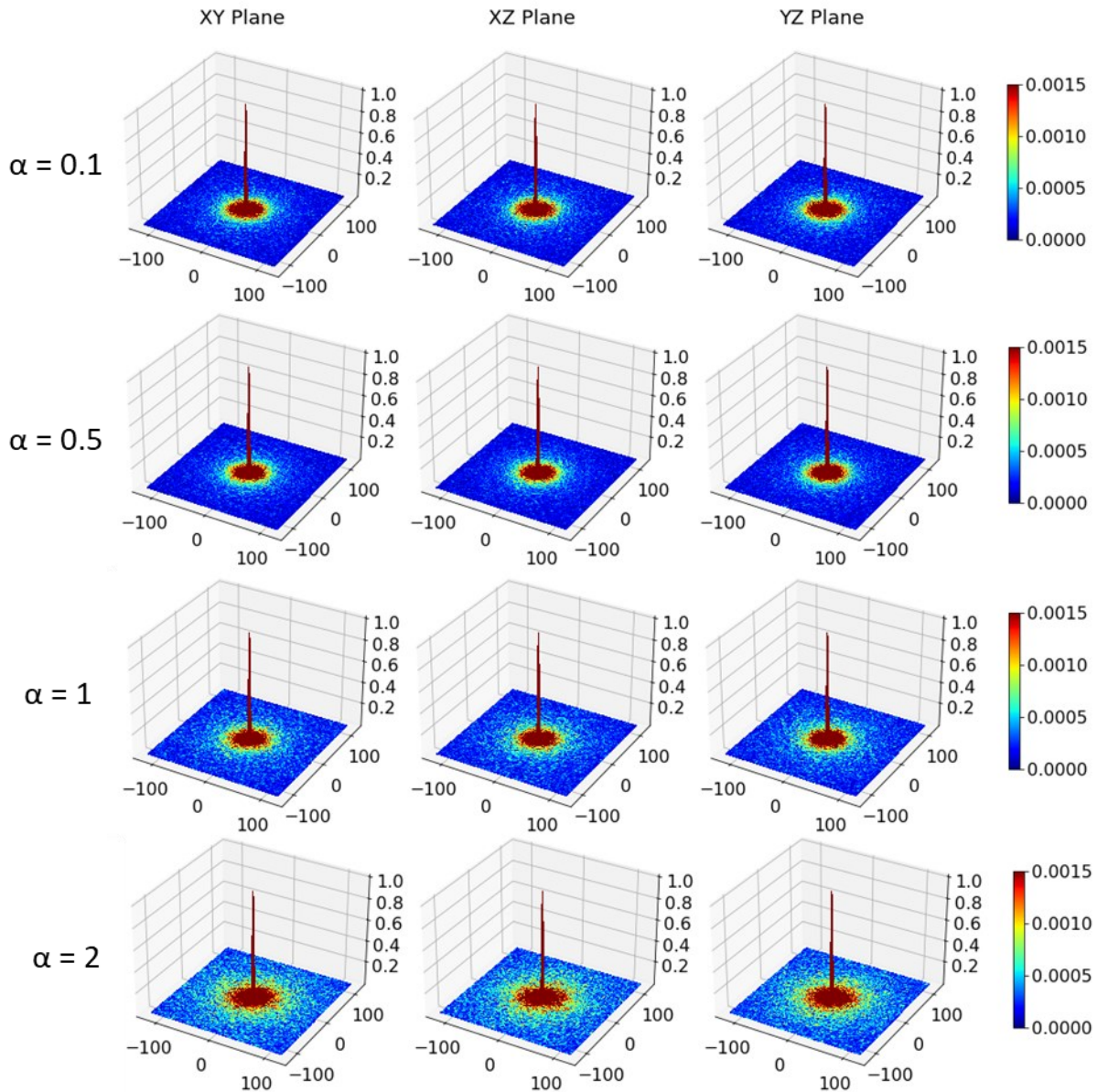


Figure 43: A 3 echo MESS trajectory at various α radius modulation values showing its impact on the first echo's PSF.

The digital phantom images in Figure 44 corresponding to the different α values do not show significant differences in image quality, with comparable image signal, contrast, and blurring. No α value shows improved image resolution, indicating the trajectory's k-space extent is sufficient to produce the desired 2mm resolution images. Ringing artifacts are prominent for all α values, which could be due to suboptimal image reconstruction parameters leading to

insufficient regularization. Equal image quality suggests that the PDHG NUFFT image reconstruction works equally for various non-uniform sampling densities.

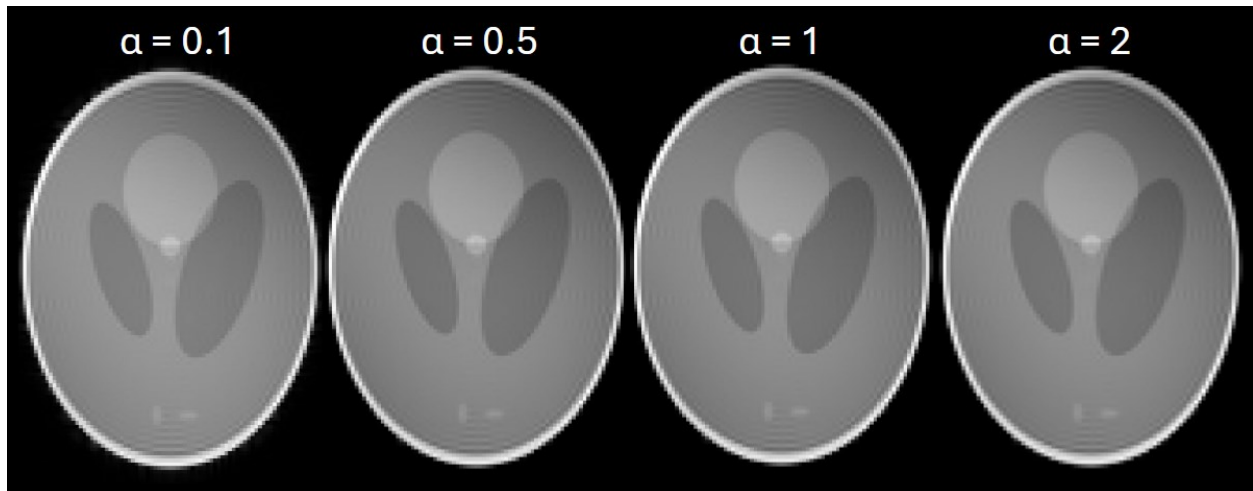


Figure 44: Simulated digital phantom images at of the first echo of a 3 echo MESS trajectory with 6ms readout (2ms per echo), 2mm resolution, 240 FOV, $R = 1$, and three different α values of 0.5 (left), 1 (middle), and 2 (right).

Image quality between all α values is consistent in the real phantom images in Figure 45, which agrees with our simulation and PSF analysis results. The increase in α leads to sparser sampling of the k-space periphery and the addition of shots to meet the Nyquist criterion, leading to increased scan time, as seen in Table 9. Similarly, a low α of 0.1 required more shots due to the middle k-space radius region being sparsely sampled. This suggests that there is an optimal α to minimize scan time.

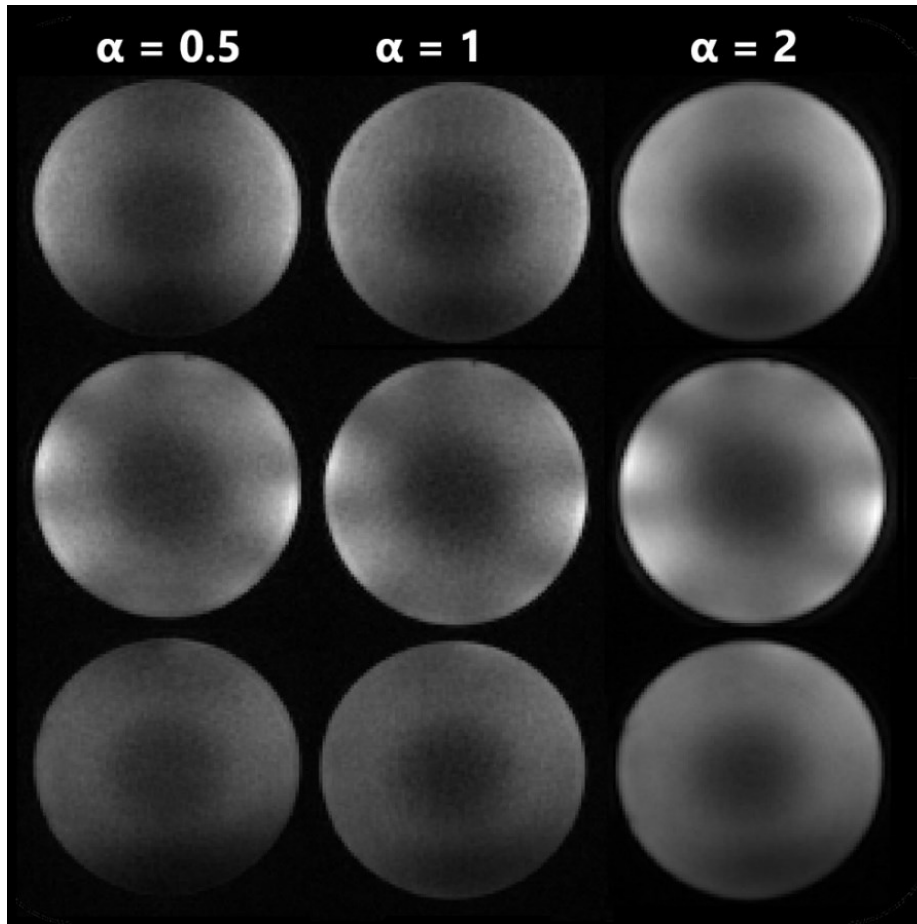


Figure 45: First echo of a 3 echo MESS acquisition at 204 FOV, 2mm resolution, 6ms readout (2ms per echo), $R = 1$ at different α values of 0.5 (left), 1 (middle) and 2 (right). Differences between image quality due to a different α parameter are compared.

Table 9: Table summarizing scan parameters for various α values for a 3 echo MESS acquisition at 204 FOV, 2mm resolution, 6ms readout (2ms per echo), $R = 1$, and the Cartesian equivalent.

	$\alpha = 0.1$	$\alpha = 0.5$	$\alpha = 1$	$\alpha = 2$
Number of shots	23 629	12 827	13 828	15 444

5 Discussion

A fast, motion-robust gradient echo MRI acquisition trajectory with incoherent undersampling artifacts was designed for the efficient acquisition of quantitative $T2^*$ data of the brain. An existing Seiffert spiral trajectory was adapted to multi-echo imaging by altering the radial winding and implemented at 7T for high-resolution imaging. The novelty of this design is the flexible multi-echo NC acquisition scheme with smooth waveforms and continuous readouts

along all echoes. This allows for variability in readout time and echo times, and reduced scan times compared to line-by-line Cartesian multi-echo sampling.

The design of the Seiffert spiral demonstrated compatibility with single and multi-echo acquisition schemes. The artifacts present in the undersampled case of $R = 2$ showed mild blurring in a human brain acquisition (Figure 36) while the $R = 6$ case showed image quality degradation in the form of noise-like artifacts on digital phantom simulations (Figure 34). This is superior to the Cartesian undersampled case, which renders wrap around artifacts which impact image quality and interpretation more severely than the incoherent aliasing artifacts in the undersampled Seiffert spiral trajectory. The single echo and MESS trajectory also showed decreased scan times for the fully sampled and undersampled cases at matching TE and TR's, demonstrating they are a flexible and more efficient alternative to Cartesian sampling for matching scan parameters.

Seiffert Spiral Image Quality

Single echo digital phantom images in Figure 34 show good image quality for the fully sampled, and $R = 2$ high resolution Seiffert spiral, with noise-like undersampling artifacts that don't greatly hinder image quality for the $R = 6$ case. This extends to the real brain acquisition in Figure 36, where even the fully sampled Seiffert spiral brain image is blurry in comparison to the Cartesian acquisition, along with ringing artifacts. The MESS trajectory's artifacts also appear as noise-like speckles in the image as can be seen from the $R = 6$, 5 echo MESS digital phantom images in Figure 40, while the $R = 1$, 3 echo MESS images in Figure 44 showed sharp images with some ringing along contrast borders for all α values. This ringing is likely due to not enough impact of the L1-wavelet regularization parameter in the PDHG algorithm, leading to good delineation of tissue borders but significant ringing artifacts. Optimizations to the weighing of the regularization term could lead to ringing artifact improvement.

The human brain images show that even the fully sampled acquisition of the single echo Seiffert spiral did not produce the expected image quality due to ringing artifacts. This contrasts with the digital phantom simulations and real phantom experiments, which showed that the trajectory sampling and image reconstruction pipeline is sufficient to produce high-resolution

images. This disagreement between ideal and real imaging conditions signify the Seiffert spiral could be impacted by main magnetic field imperfections leading to off-resonance, as well as gradient trajectory deviations, and eddy current affects.

Spiral-In-Out Trajectory Winding Compared to the Spiral-Out

The change of trajectory shape from spiral-out to spiral-in-out necessary for the multi-echo case did not result in a change in image quality for the digital phantom images and real phantom images (Figure 39). T2* blurring affects the acquired images in different ways depending on the sampling trajectory used. For the spiral-out trajectory, k-space points at the same radial distance from the centre are all sampled at the same time after the RF pulse resulting in the same T2* signal decay (Table 5). In contrast, for the spiral-in-out trajectory, points at the same radial distance from the centre of k-space can be sampled at two different time points along the T2* decay curve corresponding to the spiral-out and spiral-in segments of the trajectory (Table 6).

PSF analyses at longer readout times of 6ms reveal some image quality degradation in the form of noise in the PSF due to different T2* decay times along the k-space radius for the spiral-in-out trajectory, with no additional PSF artifacts for the spiral-out case (Figure 37). Whereas the FWHM analyses showed more enhanced peak broadening for the spiral-out case due to T2* blurring, suggesting increased image blurring (Table 6, Figure 39).

MESS Implementation

The multi-echo trajectory demonstrated the flexibility of MESS in designing a trajectory for various readout durations, number of echoes, and other image specifications. A 3 echo MESS with a 6ms (2ms per echo) readout showed improved image quality in comparison to a longer 5 echo, 20ms MESS (4ms per echo) design (Figure 42 vs Figure 41). Longer readout times per echo are associated with more signal drop-off, more T2* blurring, and decreased scan times. The assumption that performing a Nyquist check on only the first echo only was deemed sufficient due to comparable resolutions and image quality between the different echo time images from digital (Figure 40) and real (Figure 41 and Figure 42) phantom scans.

Non-Uniform Radial Sampling Density

Different radial k-space densities modulated by α did not have a significant impact on image quality in the simulated phantom data (Figure 44) and real phantom images (Figure 45). This signifies the PDHG with L1-wavelet regularization reconstruction pipeline is sufficient in reconstructing various designs of non-uniform k-space trajectories (Figure 44). Furthermore, an α of 0.5 showed the fastest scan time requiring ~ 1.8 and ~ 1.2 times less shots than an α of 0.1 and 2 respectively to meet the Nyquist criteria throughout k-space (Figure 45 and Table 9). However, since all shots sample the center of k-space, all Seiffert spiral trajectories benefit from an increase in SNR.

There is a tendency for excessive ringing when the L1-wavelet regularization coefficient is insufficiently large, observed in the digital phantom simulations in Figure 45 and Figure 44. This can be improved by manually adjusting the regularization coefficient, but the optimal value can vary across various trajectory designs.

5.1 Comparison to Previous Work

Previous Seiffert spiral implementations have produced high-resolution image quality, demonstrating 0.85mm isotropic images of the knee [11] and 0.72mm isotropic resolution images of the brain [1]. Phantom images showed comparable imaging results to Cartesian imaging, and knee images showed accurate representation of structure, with less blurring and improved sharpness in comparison to Cones acquisitions [11]. This is consistent with the phantom simulations that showed good image quality with the appropriate target resolution in Figure 34. The single echo Seiffert spiral acquired brain images in Figure 35 did not show artifact free image quality as demonstrated in the previous work, instead showed considerable ringing and some blurring leading to worsened image quality than the Cartesian equivalent. The Seiffert spiral image reconstruction however included a density compensation factor calculation through 3D Vorrnoi tessellation and trajectory corrections using the gradient impulse response function before gridding [11]. These have not been implemented yet into the reconstruction pipeline of this project and are thus part of future work.

Additionally, the PSF's peak FWHM calculated for the Seiffert spiral is larger than the target resolution, which is consistent with previous 3D spiral trajectory analysis. The FWHM of the fully sampled single echo Seiffert spiral is 1.28mm, ~1.6 times greater than the target 0.8mm resolution. This is similar to the 1.69 times greater FWHM noted by Rob Stobbe for both the Yarnball and 3D Cones trajectory [1]. This is likely due to the inability to find an adequate solution to the iterative image reconstruction algorithm when no structure is present, which is not required when reconstructing a uniformly sampled Cartesian image. The speckled noise-like undersampling artifacts in the PSF for the undersampled single echo Seiffert spiral in Figure 32 is akin to those reported by Speidel in Figure 14. Similarly, undersampling artifacts appeared as blurring in both the R=2 Seiffert spiral real human brain imaging (Figure 36) and the R=8 undersampled Seiffert spiral acquisition reported by Speidel (Figure 12) [11].

Similar to the results of this thesis, Speidel's implementation also demonstrated scan time improvements compared to the Cartesian case [11]. The previous implementation of the Seiffert spiral found a R = 10 implementation achieved 2.4 times faster scan times [11]. Although this undersampling factor was not testing for the Seiffert spiral, the single echo implementation found a 1.3- and 1.4-times faster acquisition than the Cartesian equivalent for matching TE and TR, for undersampling factors of 1 and 2 respectively.

While the Yarnball trajectory has been utilized for dual echo acquisitions [70, 71], the MESS implementation represents an advancement as the first multi-echo implementation of a Seiffert spiral, offering flexibility with any number of echoes, seamless transitions between echoes, and a spiral-in-out pattern. Additionally, it offers the benefit of more uniformly distributed sampling in k-space compared to the Yarnball method, which oversamples the z-axis by a factor of 10, resulting in unnecessary samples [1].

5.2 Limitations and Future Work

The fully sampled Cartesian case demonstrated the highest image quality with sharp differentiation of features in the human brain image in Figure 36. There are several potential improvements that can be addressed in future work, including improvements to the trajectory design and image reconstruction pipeline to achieve high-resolution images across all echoes.

Trajectory Design Improvements

Trajectory design improvements could be made to improve k-space uniformity and potentially achieve the same image quality for less shots by ensuring the shots of the trajectory are spread out from each other. This was previously implemented by Speidel et al by calculating the discrepancy across all shots and optimizing axis rotations to minimize discrepancy [11]. However, this is a computationally intensive process that precludes the imaging trajectory from being designed online. Alternatively, the trajectory's shape can be modified by modelling the samples through a minimization of Coulomb force system. The modification of trajectory shape would have to preserve spacing between points, thus sampling rate, and the total trajectory arch length, thus readout time [103].

NUFFT Density Compensation

NC trajectories introduce non-uniform sampling densities which require adapted image reconstruction algorithms. These image reconstruction errors have been improved in the past through the calculation of a DCF [104], which can be implemented through various open-source toolboxes [105]. The NUFFT parameters can also be optimized and other available iterative methods for image reconstruction can be evaluated, such as the (fast) iterative soft-thresholding algorithm, alternating direction method of multipliers, and iteratively regularized gauss-newton method to optimize reconstructed image quality [95].

Undersampled image reconstruction

One of the advantages of the Seiffert spiral trajectory is the non-coherent aliasing artifacts that make it ideal for parallel imaging and compressed sensing reconstruction of undersampled data. This was demonstrated using digital phantom simulations using the PDHG algorithm which uses SENSE to reconstruct missing data. However, this has not yet been demonstrated for real MESS data at a significant undersampling factor of 6 or greater. Further work is thus required to acquire real undersampled human brain data optimize undersampled image reconstruction [95].

Trajectory Deviation Corrections

Lastly, k-space trajectories commonly deviate from their expected paths due to gradient imperfections and spatio-temporal variations in B_0 [106]. These errors accumulate over time and thus impact longer readout trajectories more. This leads to incorrect frequencies assigned to the measured signal and ultimately image distortions and artifacts [92-94]. These sources of artifacts are not present in the digital phantom images but affect the real phantom and human brain data acquired at 7T (Figure 36). For instance, the impact of B_0 non-uniformities is seen in Figure 41 and Figure 42 in the form of signal dropout, especially at later echo times.

The true k-space trajectory can be measured using concurrent magnetic field monitoring with Skope field probes and used in the image reconstruction to improve image quality [94]. Similarly, the gradient's impulse response function can be measured for the specific MRI gradient system. This can then be used to alter the trajectory's path during the creation of gradient waveforms, or during the reconstruction to align the desired and true trajectory locations [107].

Additionally, ΔB_0 corrections can be implemented to mitigate main magnetic field non-uniformities leading to geometric distortions and signal dropouts, especially prominent in later echoes of Figure 41 and Figure 42. This can be fixed by acquiring a B_0 map before the MESS acquisition and correcting the main magnetic field profile in the image reconstruction [107].

Additional Quantitative Imaging Applications

The use of the MESS could be implemented for the acquisition of high-resolution $T2^*$ and QSM mapping. High-resolution maps of the human brain can be created to quantify iron and myelin in the brain as discussed thoroughly in the background section of this thesis. Apart from the commonly used non-exponential fit to determine the characteristic $T2^*$ time, multi-component $T2^*$ mapping could also be explored using a MESS acquisition for myelin water imaging [108, 109]. The spiral-out trajectory design is ideal to capture the short $T2^*$ myelin water.

The MESS trajectory could be applied to speed up other quantitative MRI techniques such as FLASH-based variable flip angle $T1$ mapping or MT saturation mapping [110]. The latter have

used multi-echo Cartesian readouts to improve SNR efficiency and simultaneously estimate $T2^*$ [111].

6 Conclusion

This thesis project aimed to address the challenges associated with imaging brain iron deposition using MRI techniques. By designing a novel 3D non-Cartesian trajectory known as the multi-echo Seiffert spiral (MESS), this study sought to improve imaging efficiency and quality while reducing scan times. The advantages of the MESS trajectory include strategic k-space under-sampling, compatibility with motion correction techniques, and improved conditioning for compressed sensing and parallel image reconstruction. The MESS trajectory, implemented on a 7 Tesla scanner, demonstrated promising results in simulations, phantom tests, and human subjects, outperforming conventional Cartesian sampling demonstrating 1.3- and 1.4-times faster scan time for the single echo case acquisition with undersampling factors of $R=1$ and 2 , respectively. The 5 echo MESS acquisition was 4.2-times faster than Cartesian for an $R=6$. The image quality of the human brain images for the single echo Seiffert spiral are currently of lower quality than the Cartesian images, likely due to a non-optimal reconstruction pipeline, which will be improved in future work. Overall, this fast 3D MESS imaging trajectory holds significant potential for generating high-resolution $T2^*$ maps and quantitative susceptibility maps (QSM) of the brain in short scan times, making it suitable for clinical applications in the diagnosis and monitoring of neurodegenerative disorders.

7 References

- [1] R. W. Stobbe and C. Beaulieu, "Three-dimensional Yarnball k-space acquisition for accelerated MRI," *Magn Reson Med*, vol. 85, no. 4, pp. 1840-1854, Apr 2021, doi: 10.1002/mrm.28536.
- [2] A. Ndayisaba, C. Kaindlstorfer, and G. K. Wenning, "Iron in Neurodegeneration - Cause or Consequence?," *Front Neurosci*, vol. 13, p. 180, 2019, doi: 10.3389/fnins.2019.00180.
- [3] P. Ravanfar *et al.*, "Systematic Review: Quantitative Susceptibility Mapping (QSM) of Brain Iron Profile in Neurodegenerative Diseases," *Front Neurosci*, vol. 15, p. 618435, 2021, doi: 10.3389/fnins.2021.618435.
- [4] Z. Zhao *et al.*, "The effect of beta-amyloid and tau protein aggregations on magnetic susceptibility of anterior hippocampal laminae in Alzheimer's diseases," *Neuroimage*, vol. 244, p. 118584, Dec 1 2021, doi: 10.1016/j.neuroimage.2021.118584.
- [5] Y. Wang *et al.*, "Clinical quantitative susceptibility mapping (QSM): Biometal imaging and its emerging roles in patient care," *J Magn Reson Imaging*, vol. 46, no. 4, pp. 951-971, Oct 2017, doi: 10.1002/jmri.25693.
- [6] S. Hametner *et al.*, "The influence of brain iron and myelin on magnetic susceptibility and effective transverse relaxation - A biochemical and histological validation study," *Neuroimage*, vol. 179, pp. 117-133, Oct 1 2018, doi: 10.1016/j.neuroimage.2018.06.007.
- [7] A. P. Fan *et al.*, "Quantitative oxygenation venography from MRI phase," *Magn Reson Med*, vol. 72, no. 1, pp. 149-59, Jul 2014, doi: 10.1002/mrm.24918.
- [8] J. Huck *et al.*, "High resolution atlas of the venous brain vasculature from 7 T quantitative susceptibility maps," *Brain Struct Funct*, vol. 224, no. 7, pp. 2467-2485, Sep 2019, doi: 10.1007/s00429-019-01919-4.
- [9] R. Burgetova *et al.*, "Age-related magnetic susceptibility changes in deep grey matter and cerebral cortex of normal young and middle-aged adults depicted by whole brain analysis," *Quant Imaging Med Surg*, vol. 11, no. 9, pp. 3906-3919, Sep 2021, doi: 10.21037/qims-21-87.

- [10] A. P. Fan *et al.*, "Elevated brain oxygen extraction fraction measured by MRI susceptibility relates to perfusion status in acute ischemic stroke," *J Cereb Blood Flow Metab*, vol. 40, no. 3, pp. 539-551, Mar 2020, doi: 10.1177/0271678X19827944.
- [11] T. Speidel, P. Metze, and V. Rasche, "Efficient 3D Low-Discrepancy k -Space Sampling Using Highly Adaptable Seiffert Spirals," *IEEE Trans Med Imaging*, vol. 38, no. 8, pp. 1833-1840, Aug 2019, doi: 10.1109/TMI.2018.2888695.
- [12] E. M. Haacke and E. M. Haacke, *Magnetic resonance imaging : physical principles and sequence design*. New York: Wiley (in English), 1999, pp. xxvii, 914 pages : illustrations.
- [13] J. Cohen-Adad, "What can we learn from T2* maps of the cortex?," (in eng), *Neuroimage*, vol. 93 Pt 2, pp. 189-200, Jun 2014, doi: 10.1016/j.neuroimage.2013.01.023.
- [14] J. Ridgway, "Cardiovascular magnetic resonance physics for clinicians: Part I," *Journal of cardiovascular magnetic resonance : official journal of the Society for Cardiovascular Magnetic Resonance*, vol. 12, p. 71, 11/30 2010, doi: 10.1186/1532-429X-12-71.
- [15] C. Langkammer *et al.*, "Quantitative MR imaging of brain iron: a postmortem validation study," (in eng), *Radiology*, vol. 257, no. 2, pp. 455-62, Nov 2010, doi: 10.1148/radiol.10100495.
- [16] Y. Liu *et al.*, "Correlation Between Cerebral Venous Oxygen Level and Cognitive Status in Patients With Alzheimer's Disease Using Quantitative Susceptibility Mapping," *Front Neurosci*, vol. 14, p. 570848, 2020, doi: 10.3389/fnins.2020.570848.
- [17] G. A. Fulop *et al.*, "Role of age-related alterations of the cerebral venous circulation in the pathogenesis of vascular cognitive impairment," *Am J Physiol Heart Circ Physiol*, vol. 316, no. 5, pp. H1124-H1140, May 1 2019, doi: 10.1152/ajpheart.00776.2018.
- [18] K. Ishii, H. Kitagaki, M. Kono, and E. Mori, "Decreased medial temporal oxygen metabolism in Alzheimer's disease shown by PET," *J Nucl Med*, vol. 37, no. 7, pp. 1159-65, Jul 1996. [Online]. Available: <https://www.ncbi.nlm.nih.gov/pubmed/8965188>.
- [19] E. J. McAllum *et al.*, "Regional iron distribution and soluble ferroprotein profiles in the healthy human brain," *Prog Neurobiol*, vol. 186, p. 101744, Mar 2020, doi: 10.1016/j.pneurobio.2019.101744.

- [20] P. Ramos, A. Santos, N. R. Pinto, R. Mendes, T. Magalhaes, and A. Almeida, "Iron levels in the human brain: a post-mortem study of anatomical region differences and age-related changes," *J Trace Elem Med Biol*, vol. 28, no. 1, pp. 13-7, Jan 2014, doi: 10.1016/j.jtemb.2013.08.001.
- [21] J. Acosta-Cabronero, M. J. Betts, A. Cardenas-Blanco, S. Yang, and P. J. Nestor, "In Vivo MRI Mapping of Brain Iron Deposition across the Adult Lifespan," *J Neurosci*, vol. 36, no. 2, pp. 364-74, Jan 13 2016, doi: 10.1523/JNEUROSCI.1907-15.2016.
- [22] S. Siemonsen, J. Finsterbusch, J. Matschke, A. Lorenzen, X. Q. Ding, and J. Fiehler, "Age-dependent normal values of T2* and T2' in brain parenchyma," *AJNR Am J Neuroradiol*, vol. 29, no. 5, pp. 950-5, May 2008, doi: 10.3174/ajnr.A0951.
- [23] L. I. Wallis *et al.*, "MRI assessment of basal ganglia iron deposition in Parkinson's disease," *J Magn Reson Imaging*, vol. 28, no. 5, pp. 1061-7, Nov 2008, doi: 10.1002/jmri.21563.
- [24] W. R. Martin, M. Wieler, and M. Gee, "Midbrain iron content in early Parkinson disease: a potential biomarker of disease status," (in eng), *Neurology*, vol. 70, no. 16 Pt 2, pp. 1411-7, Apr 15 2008, doi: 10.1212/01.wnl.0000286384.31050.b5.
- [25] S. Baudrexel *et al.*, "Quantitative mapping of T1 and T2* discloses nigral and brainstem pathology in early Parkinson's disease," *Neuroimage*, vol. 51, no. 2, pp. 512-20, Jun 2010, doi: 10.1016/j.neuroimage.2010.03.005.
- [26] B. Zhou, s. li, H. He, and X. Feng, "The evaluation of iron content in Alzheimer's disease by magnetic resonance imaging: Phase and R2* methods," *Advances in Alzheimer's Disease*, vol. 02, pp. 51-59, 01/01 2013, doi: 10.4236/aad.2013.22007.
- [27] B. R. Isaacs *et al.*, "3 versus 7 Tesla magnetic resonance imaging for parcellations of subcortical brain structures in clinical settings," *PLoS One*, vol. 15, no. 11, p. e0236208, 2020, doi: 10.1371/journal.pone.0236208.
- [28] E. Springer *et al.*, "Comparison of Routine Brain Imaging at 3 T and 7 T," *Invest Radiol*, vol. 51, no. 8, pp. 469-82, Aug 2016, doi: 10.1097/RLI.0000000000000256.

- [29] A. M. Peters *et al.*, "T2* measurements in human brain at 1.5, 3 and 7 T," *Magnetic Resonance Imaging*, vol. 25, no. 6, pp. 748-753, 2007/07/01/ 2007, doi: <https://doi.org/10.1016/j.mri.2007.02.014>.
- [30] E. C. Obusez *et al.*, "7T MR of intracranial pathology: Preliminary observations and comparisons to 3T and 1.5T," *Neuroimage*, vol. 168, pp. 459-476, Mar 2018, doi: 10.1016/j.neuroimage.2016.11.030.
- [31] M. M. Zeineh, Y. Chen, H. H. Kitzler, R. Hammond, H. Vogel, and B. K. Rutt, "Activated iron-containing microglia in the human hippocampus identified by magnetic resonance imaging in Alzheimer disease," *Neurobiol Aging*, vol. 36, no. 9, pp. 2483-500, Sep 2015, doi: 10.1016/j.neurobiolaging.2015.05.022.
- [32] R. M. Gracien *et al.*, "Multimodal quantitative MRI assessment of cortical damage in relapsing-remitting multiple sclerosis," *J Magn Reson Imaging*, vol. 44, no. 6, pp. 1600-1607, Dec 2016, doi: 10.1002/jmri.25297.
- [33] M. A. Bernstein, K. F. King, and X. J. Zhou, "CHAPTER 16 - ECHO TRAIN PULSE SEQUENCES," in *Handbook of MRI Pulse Sequences*, M. A. Bernstein, K. F. King, and X. J. Zhou Eds. Burlington: Academic Press, 2004, pp. 702-801.
- [34] J. J. Zwanenburg, M. J. Versluis, P. R. Luijten, and N. Petridou, "Fast high resolution whole brain T2* weighted imaging using echo planar imaging at 7T," *Neuroimage*, vol. 56, no. 4, pp. 1902-7, Jun 15 2011, doi: 10.1016/j.neuroimage.2011.03.046.
- [35] M. J. Fair, P. D. Gatehouse, E. V. DiBella, and D. N. Firmin, "A review of 3D first-pass, whole-heart, myocardial perfusion cardiovascular magnetic resonance," *J Cardiovasc Magn Reson*, vol. 17, no. 1, p. 68, Aug 1 2015, doi: 10.1186/s12968-015-0162-9.
- [36] J. G. Pipe, "Motion correction with PROPELLER MRI: application to head motion and free-breathing cardiac imaging," *Magn Reson Med*, vol. 42, no. 5, pp. 963-9, Nov 1999, doi: 10.1002/(sici)1522-2594(199911)42:5<963::aid-mrm17>3.0.co;2-l.
- [37] G. Madelin, "Sodium Magnetic Resonance Imaging: Biomedical Applications," 12/18 2012.
- [38] L. Feng *et al.*, "Golden-angle radial sparse parallel MRI: combination of compressed sensing, parallel imaging, and golden-angle radial sampling for fast and flexible dynamic

- volumetric MRI," *Magn Reson Med*, vol. 72, no. 3, pp. 707-17, Sep 2014, doi: 10.1002/mrm.24980.
- [39] D. Piccini, A. Littmann, S. Nielles-Vallespin, and M. O. Zenge, "Spiral phyllotaxis: the natural way to construct a 3D radial trajectory in MRI," *Magn Reson Med*, vol. 66, no. 4, pp. 1049-56, Oct 2011, doi: 10.1002/mrm.22898.
- [40] L. Feng *et al.*, "5D whole-heart sparse MRI," *Magn Reson Med*, vol. 79, no. 2, pp. 826-838, Feb 2018, doi: 10.1002/mrm.26745.
- [41] S. Coppo *et al.*, "Free-running 4D whole-heart self-navigated golden angle MRI: Initial results," *Magn Reson Med*, vol. 74, no. 5, pp. 1306-16, Nov 2015, doi: 10.1002/mrm.25523.
- [42] R. W. Chan, E. A. Ramsay, C. H. Cunningham, and D. B. Plewes, "Temporal stability of adaptive 3D radial MRI using multidimensional golden means," *Magn Reson Med*, vol. 61, no. 2, pp. 354-63, Feb 2009, doi: 10.1002/mrm.21837.
- [43] K. P. Forbes, J. G. Pipe, C. R. Bird, and J. E. Heiserman, "PROPELLER MRI: clinical testing of a novel technique for quantification and compensation of head motion," *J Magn Reson Imaging*, vol. 14, no. 3, pp. 215-22, Sep 2001, doi: 10.1002/jmri.1176.
- [44] K. Arfanakis, A. A. Tamhane, J. G. Pipe, and M. A. Anastasio, "k-space undersampling in PROPELLER imaging," *Magn Reson Med*, vol. 53, no. 3, pp. 675-83, Mar 2005, doi: 10.1002/mrm.20380.
- [45] Y. Chang, J. G. Pipe, J. P. Karis, W. N. Gibbs, N. R. Zwart, and M. Schar, "The effects of SENSE on PROPELLER imaging," *Magn Reson Med*, vol. 74, no. 6, pp. 1598-608, Dec 2015, doi: 10.1002/mrm.25557.
- [46] G. H. Glover and A. T. Lee, "Motion artifacts in fMRI: comparison of 2DFT with PR and spiral scan methods," (in eng), *Magn Reson Med*, vol. 33, no. 5, pp. 624-35, May 1995, doi: 10.1002/mrm.1910330507.
- [47] B. Wu, W. Li, A. V. Avram, S. M. Gho, and C. Liu, "Fast and tissue-optimized mapping of magnetic susceptibility and T2* with multi-echo and multi-shot spirals," *Neuroimage*, vol. 59, no. 1, pp. 297-305, Jan 2 2012, doi: 10.1016/j.neuroimage.2011.07.019.

- [48] J. H. Lee, B. A. Hargreaves, B. S. Hu, and D. G. Nishimura, "Fast 3D imaging using variable-density spiral trajectories with applications to limb perfusion," *Magn Reson Med*, vol. 50, no. 6, pp. 1276-85, Dec 2003, doi: 10.1002/mrm.10644.
- [49] X. Cao, H. Ye, C. Liao, Q. Li, H. He, and J. Zhong, "Fast 3D brain MR fingerprinting based on multi-axis spiral projection trajectory," *Magn Reson Med*, vol. 82, no. 1, pp. 289-301, Jul 2019, doi: 10.1002/mrm.27726.
- [50] Y. Qian and F. E. Boada, "Acquisition-weighted stack of spirals for fast high-resolution three-dimensional ultra-short echo time MR imaging," *Magn Reson Med*, vol. 60, no. 1, pp. 135-45, Jul 2008, doi: 10.1002/mrm.21620.
- [51] G. Dournes *et al.*, "3D ultrashort echo time MRI of the lung using stack-of-spirals and spherical k-space coverages: Evaluation in healthy volunteers and parenchymal diseases," *J Magn Reson Imaging*, vol. 48, no. 6, pp. 1489-1497, Dec 2018, doi: 10.1002/jmri.26212.
- [52] J. R. Liao, J. M. Pauly, T. J. Brosnan, and N. J. Pelc, "Reduction of motion artifacts in cine MRI using variable-density spiral trajectories," *Magn Reson Med*, vol. 37, no. 4, pp. 569-75, Apr 1997, doi: 10.1002/mrm.1910370416.
- [53] X. Shen *et al.*, "Ultra-short T(2) components imaging of the whole brain using 3D dual-echo UTE MRI with rosette k-space pattern," *Magn Reson Med*, vol. 89, no. 2, pp. 508-521, Feb 2023, doi: 10.1002/mrm.29451.
- [54] A. M. Bush *et al.*, "Rosette Trajectories Enable Ungated, Motion-Robust, Simultaneous Cardiac and Liver T(2) * Iron Assessment," *J Magn Reson Imaging*, vol. 52, no. 6, pp. 1688-1698, Dec 2020, doi: 10.1002/jmri.27196.
- [55] S. Tao, Y. Shu, J. D. Trzasko, J. Huston, and M. A. Bernstein, "Partial fourier shells trajectory for non-cartesian MRI," *Phys Med Biol*, vol. 64, no. 4, p. 04NT01, Feb 6 2019, doi: 10.1088/1361-6560/aafcc5.
- [56] Y. Shu, A. M. Elliott, S. J. Riederer, and M. A. Bernstein, "Motion correction properties of the shells k-space trajectory," *Magn Reson Imaging*, vol. 24, no. 6, pp. 739-49, Jul 2006, doi: 10.1016/j.mri.2005.10.038.

- [57] Y. Shu, S. Tao, J. D. Trzasko, J. Huston, 3rd, P. T. Weavers, and M. A. Bernstein, "Magnetization-prepared shells trajectory with automated gradient waveform design," *Magn Reson Med*, vol. 79, no. 4, pp. 2024-2035, Apr 2018, doi: 10.1002/mrm.26863.
- [58] Y. Shu, M. A. Bernstein, J. Huston, 3rd, and D. Rettmann, "Contrast-enhanced intracranial magnetic resonance angiography with a spherical shells trajectory and online gridding reconstruction," *J Magn Reson Imaging*, vol. 30, no. 5, pp. 1101-9, Nov 2009, doi: 10.1002/jmri.21938.
- [59] M. O. Malave *et al.*, "Whole-heart coronary MR angiography using a 3D cones phyllotaxis trajectory," *Magn Reson Med*, vol. 81, no. 2, pp. 1092-1103, Feb 2019, doi: 10.1002/mrm.27475.
- [60] Y. J. Ma *et al.*, "Volumetric imaging of myelin in vivo using 3D inversion recovery-prepared ultrashort echo time cones magnetic resonance imaging," *NMR Biomed*, vol. 33, no. 10, p. e4326, Oct 2020, doi: 10.1002/nbm.4326.
- [61] F. Riemer, B. S. Solanky, C. Stehning, M. Clemence, C. A. Wheeler-Kingshott, and X. Golay, "Sodium ((²³Na) ultra-short echo time imaging in the human brain using a 3D-Cones trajectory," *MAGMA*, vol. 27, no. 1, pp. 35-46, Feb 2014, doi: 10.1007/s10334-013-0395-2.
- [62] R. R. Ingle *et al.*, "Nonrigid autofocus motion correction for coronary MR angiography with a 3D cones trajectory," *Magn Reson Med*, vol. 72, no. 2, pp. 347-61, Aug 2014, doi: 10.1002/mrm.24924.
- [63] M. Wu *et al.*, "Magic angle effect on adiabatic T(1rho) imaging of the Achilles tendon using 3D ultrashort echo time cones trajectory," *NMR Biomed*, vol. 33, no. 8, p. e4322, Aug 2020, doi: 10.1002/nbm.4322.
- [64] S. P. Koundinyan *et al.*, "High-resolution, respiratory-resolved coronary MRA using a Phyllotaxis-reordered variable-density 3D cones trajectory," *Magn Reson Imaging*, vol. 98, pp. 140-148, May 2023, doi: 10.1016/j.mri.2023.01.008.
- [65] Y. Kee *et al.*, "Free-breathing R2 * mapping of hepatic iron overload in children using 3D multi-echo UTE cones MRI," *Magn Reson Med*, vol. 85, no. 5, pp. 2608-2621, May 2021, doi: 10.1002/mrm.28610.

- [66] H. Jang *et al.*, "Feasibility of ultrashort echo time quantitative susceptibility mapping with a 3D cones trajectory in the human brain," *Front Neurosci*, vol. 16, p. 1033801, 2022, doi: 10.3389/fnins.2022.1033801.
- [67] H. Rahbar and S. C. Partridge, "Editorial on "Diffusion-Weighted Double-Echo Steady-State with a 3D Cones Trajectory for Non-Contrast-Enhanced Breast MRI"," *J Magn Reson Imaging*, vol. 53, no. 5, pp. 1606-1607, May 2021, doi: 10.1002/jmri.27524.
- [68] C. J. Moran *et al.*, "Diffusion-weighted double-echo steady-state with a three-dimensional cones trajectory for non-contrast-enhanced breast MRI," *J Magn Reson Imaging*, vol. 53, no. 5, pp. 1594-1605, May 2021, doi: 10.1002/jmri.27492.
- [69] P. T. Gurney, B. A. Hargreaves, and D. G. Nishimura, "Design and analysis of a practical 3D cones trajectory," *Magn Reson Med*, vol. 55, no. 3, pp. 575-82, Mar 2006, doi: 10.1002/mrm.20796.
- [70] C. B. Robert W. Stobbe, "Wind Out-In Dual-Echo Yarn-Ball with Application to Knee Imaging," presented at the International Society for Magnetic Resonance in Medicine, Paris, France, 2018, 4148. [Online]. Available: <https://cds.ismrm.org/protected/18MProceedings/PDFfiles/4148.html>.
- [71] W. Q. Meadus, R. W. Stobbe, J. G. Grenier, C. Beaulieu, and R. B. Thompson, "Quantification of lung water density with UTE Yarnball MRI," *Magn Reson Med*, vol. 86, no. 3, pp. 1330-1344, Sep 2021, doi: 10.1002/mrm.28800.
- [72] Y. D. Zhou, K. T. Fang, and J. H. Ning, "Mixture discrepancy for quasi-random point sets," (in English), *Journal of Complexity*, vol. 29, no. 3-4, pp. 283-301, Jun-Aug 2013, doi: 10.1016/j.jco.2012.11.006.
- [73] K. T. Fang, R. Li, and A. Sudjianto, "Design and Modeling for Computer Experiments," (in English), *Ch Crc Comp Sci Data*, pp. 1-290, 2006. [Online]. Available: <Go to ISI>://WOS:000267235200009.
- [74] C. Lazarus *et al.*, "SPARKLING: variable-density k-space filling curves for accelerated T(2)(*)-weighted MRI," *Magn Reson Med*, vol. 81, no. 6, pp. 3643-3661, Jun 2019, doi: 10.1002/mrm.27678.

- [75] P. Irarrazabal and D. G. Nishimura, "Fast three dimensional magnetic resonance imaging," *Magn Reson Med*, vol. 33, no. 5, pp. 656-62, May 1995, doi: 10.1002/mrm.1910330510.
- [76] C. R. Wyatt and A. R. Guimaraes, "3D MR fingerprinting using Seiffert spirals," *Magn Reson Med*, vol. 88, no. 1, pp. 151-163, Jul 2022, doi: 10.1002/mrm.29197.
- [77] R. Hu, R. Yang, Y. Liu, and X. Li, "Simulation and Mitigation of the Wrap-Around Artifact in the MRI Image," *Front Comput Neurosci*, vol. 15, p. 746549, 2021, doi: 10.3389/fncom.2021.746549.
- [78] K. L. Wright, J. I. Hamilton, M. A. Griswold, V. Gulani, and N. Seiberlich, "Non-Cartesian parallel imaging reconstruction," *J Magn Reson Imaging*, vol. 40, no. 5, pp. 1022-40, Nov 2014, doi: 10.1002/jmri.24521.
- [79] J. Hamilton, D. Franson, and N. Seiberlich, "Recent advances in parallel imaging for MRI," *Prog Nucl Magn Reson Spectrosc*, vol. 101, pp. 71-95, Aug 2017, doi: 10.1016/j.pnmrs.2017.04.002.
- [80] C. Baker, "Comparison of MRI Under-Sampling Techniques for Compressed Sensing with Translation Invariant Wavelets Using FastTestCS: A Flexible Simulation Tool," *Journal of Signal and Information Processing*, vol. 07, pp. 252-271, 01/01 2016, doi: 10.4236/jsip.2016.74021.
- [81] M. Lustig, D. Donoho, and J. M. Pauly, "Sparse MRI: The application of compressed sensing for rapid MR imaging," *Magn Reson Med*, vol. 58, no. 6, pp. 1182-95, Dec 2007, doi: 10.1002/mrm.21391.
- [82] F. A. Breuer, S. A. Kannengiesser, M. Blaimer, N. Seiberlich, P. M. Jakob, and M. A. Griswold, "General formulation for quantitative G-factor calculation in GRAPPA reconstructions," *Magn Reson Med*, vol. 62, no. 3, pp. 739-46, Sep 2009, doi: 10.1002/mrm.22066.
- [83] K. T. Block *et al.*, "Towards Routine Clinical Use of Radial Stack-of-Stars 3D Gradient-Echo Sequences for Reducing Motion Sensitivity," *J Korean Soc Magn Reson Med*, vol. 18, no. 2, pp. 87-106, 6/ 2014. [Online]. Available: <https://doi.org/10.13104/jksmrm.2014.18.2.87>.

- [84] H. Fischer and R. Ladebeck, "Echo-Planar Imaging Image Artifacts," in *Echo-Planar Imaging: Theory, Technique and Application*, F. Schmitt, M. K. Stehling, and R. Turner Eds. Berlin, Heidelberg: Springer Berlin Heidelberg, 1998, pp. 179-200.
- [85] J. Du *et al.*, "Artifact reduction in undersampled projection reconstruction MRI of the peripheral vessels using selective excitation," *Magn Reson Med*, vol. 51, no. 5, pp. 1071-6, May 2004, doi: 10.1002/mrm.20036.
- [86] Y. Xue, J. Yu, H. S. Kang, S. Englander, M. A. Rosen, and H. K. Song, "Automatic coil selection for streak artifact reduction in radial MRI," *Magn Reson Med*, vol. 67, no. 2, pp. 470-6, Feb 2012, doi: 10.1002/mrm.23023.
- [87] G. R. Lee, M. A. Griswold, and J. A. Tkach, "Rapid 3D radial multi-echo functional magnetic resonance imaging," *Neuroimage*, vol. 52, no. 4, pp. 1428-43, Oct 1 2010, doi: 10.1016/j.neuroimage.2010.05.004.
- [88] C. S. Law and G. H. Glover, "Interleaved spiral-in/out with application to functional MRI (fMRI)," *Magn Reson Med*, vol. 62, no. 3, pp. 829-34, Sep 2009, doi: 10.1002/mrm.22056.
- [89] R. Oshana, S. MyiLibrary Elsevier, C. Technology, and MyiLibrary, *DSP software development techniques for embedded and real-time systems*, 1st edition ed. (Embedded technology series). Amsterdam ; Boston: Elsevier/Newnes (in English), 2006.
- [90] M. Bourgeois, F. T. A. W. Wajer, D. van Ormondt, and D. Graveron-Demilly, "Reconstruction of MRI Images from Non-Uniform Sampling and Its Application to Intrascan Motion Correction in Functional MRI," in *Modern Sampling Theory: Mathematics and Applications*, J. J. Benedetto and P. J. S. G. Ferreira Eds. Boston, MA: Birkhäuser Boston, 2001, pp. 343-363.
- [91] J. A. Fessler and B. P. Sutton, "Nonuniform fast Fourier transforms using min-max interpolation," (in English), *Ieee Transactions on Signal Processing*, vol. 51, no. 2, pp. 560-574, Feb 2003, doi: 10.1109/Tsp.2002.807005.
- [92] N. De Zanche, C. Barmet, J. A. Nordmeyer-Massner, and K. P. Pruessmann, "NMR probes for measuring magnetic fields and field dynamics in MR systems," *Magn Reson Med*, vol. 60, no. 1, pp. 176-86, Jul 2008, doi: 10.1002/mrm.21624.

- [93] J. H. Duyn, Y. Yang, J. A. Frank, and J. W. van der Veen, "Simple correction method for k-space trajectory deviations in MRI," *J Magn Reson*, vol. 132, no. 1, pp. 150-3, May 1998, doi: 10.1006/jmre.1998.1396.
- [94] S. J. Vannesjo *et al.*, "Retrospective correction of physiological field fluctuations in high-field brain MRI using concurrent field monitoring," *Magn Reson Med*, vol. 73, no. 5, pp. 1833-43, May 2015, doi: 10.1002/mrm.25303.
- [95] M. H. Moritz Blumenthal, Martin Juschitz, Holme Hans Christian Martin, Bernhard Rapp, Philip Schaten, Nick Scholand, Jonathan Tamir, Christian Tonnes, Martin Uecker. "Berkeley Advanced Reconstruction Toolbox." Zenodo. (accessed.
- [96] J. C. Ye, "Compressed sensing MRI: a review from signal processing perspective," *BMC Biomed Eng*, vol. 1, p. 8, 2019, doi: 10.1186/s42490-019-0006-z.
- [97] M. Uecker *et al.*, "ESPIRiT--an eigenvalue approach to autocalibrating parallel MRI: where SENSE meets GRAPPA," *Magn Reson Med*, vol. 71, no. 3, pp. 990-1001, Mar 2014, doi: 10.1002/mrm.24751.
- [98] Y.-D. Zhou, K.-T. Fang, and J.-H. Ning, "Mixture discrepancy for quasi-random point sets," *Journal of Complexity*, vol. 29, no. 3, pp. 283-301, 2013/06/01/ 2013, doi: <https://doi.org/10.1016/j.jco.2012.11.006>.
- [99] M. Lustig, S. J. Kim, and J. M. Pauly, "A fast method for designing time-optimal gradient waveforms for arbitrary k-space trajectories," (in eng), *IEEE Trans Med Imaging*, vol. 27, no. 6, pp. 866-73, Jun 2008, doi: 10.1109/tmi.2008.922699.
- [100] P. Erdős, "Spiraling the Earth with C. G. J. Jacobi," (in English), *American Journal of Physics*, vol. 68, no. 10, pp. 888-895, Oct 2000, doi: Doi 10.1119/1.1285882.
- [101] M. A. Bernstein, K. F. King, X. J. Zhou, and ProQuest, *Handbook of MRI pulse sequences*. Amsterdam ; Boston: Academic Press (in English), 2004.
- [102] F. Ong, M. Uecker, and M. Lustig, "Accelerating Non-Cartesian MRI Reconstruction Convergence Using k-Space Preconditioning," *IEEE Trans Med Imaging*, vol. 39, no. 5, pp. 1646-1654, May 2020, doi: 10.1109/TMI.2019.2954121.
- [103] C. a. S. Yu, Henrik and Crane, Keenan, "Repulsive Curves," *ACM Trans. Graph.*, vol. 40, no. 2, 2021.

- [104] J. G. Pipe and P. Menon, "Sampling density compensation in MRI: rationale and an iterative numerical solution," *Magn Reson Med*, vol. 41, no. 1, pp. 179-86, Jan 1999, doi: 10.1002/(sici)1522-2594(199901)41:1<179::aid-mrm25>3.0.co;2-v.
- [105] J. Fessler. " Image reconstruction toolbox."
<https://web.eecs.umich.edu/~fessler/code/index.html> (accessed.
- [106] G. H. Glover, "Spiral imaging in fMRI," *Neuroimage*, vol. 62, no. 2, pp. 706-12, Aug 15 2012, doi: 10.1016/j.neuroimage.2011.10.039.
- [107] M. Veldmann, P. Ehses, K. Chow, J. F. Nielsen, M. Zaitsev, and T. Stocker, "Open-source MR imaging and reconstruction workflow," *Magn Reson Med*, vol. 88, no. 6, pp. 2395-2407, Dec 2022, doi: 10.1002/mrm.29384.
- [108] E. Alonso-Ortiz, I. R. Levesque, and G. B. Pike, "MRI-based myelin water imaging: A technical review," *Magn Reson Med*, vol. 73, no. 1, pp. 70-81, Jan 2015, doi: 10.1002/mrm.25198.
- [109] E. Alonso-Ortiz, I. R. Levesque, and G. B. Pike, "Impact of magnetic susceptibility anisotropy at 3 T and 7 T on T2*-based myelin water fraction imaging," *Neuroimage*, vol. 182, pp. 370-378, Nov 15 2018, doi: 10.1016/j.neuroimage.2017.09.040.
- [110] G. Helms, H. Dathe, K. Kallenberg, and P. Dechent, "High-resolution maps of magnetization transfer with inherent correction for RF inhomogeneity and T1 relaxation obtained from 3D FLASH MRI," *Magn Reson Med*, vol. 60, no. 6, pp. 1396-407, Dec 2008, doi: 10.1002/mrm.21732.
- [111] N. Weiskopf *et al.*, "Quantitative multi-parameter mapping of R1, PD(*), MT, and R2(*) at 3T: a multi-center validation," *Front Neurosci*, vol. 7, p. 95, 2013, doi: 10.3389/fnins.2013.00095.